

# Exotic modes of excitation in atomic nuclei far from stability

**Nils Paar**

Institut für Kernphysik, Technische Universität Darmstadt, Schlossgartenstrasse 9,  
D-64289 Darmstadt, Germany

**Dario Vretenar**

Physics Department, Faculty of Science, University of Zagreb, Bijenička 32, 10000  
Zagreb, Croatia

**Elias Khan**

Institut de Physique Nucléaire, IN<sub>2</sub>P<sub>3</sub>-CNRS/Université Paris-Sud, 91406 Orsay,  
France

**Gianluca Colò**

Dipartimento di Fisica dell'Università degli Studi and INFN, Sezione di Milano, via  
Celoria 16, 20133 Milano, Italy

**Abstract.** We review recent studies of the evolution of collective excitations in atomic nuclei far from the valley of  $\beta$ -stability. Collective degrees of freedom govern essential aspects of nuclear structure, and for several decades the study of collective modes such as rotations and vibrations has played a vital role in our understanding of complex properties of nuclei. The multipole response of unstable nuclei and the possible occurrence of new exotic modes of excitation in weakly-bound nuclear systems, present a rapidly growing field of research, but only few experimental studies of these phenomena have been reported so far. Valuable data on the evolution of the low-energy dipole response in unstable neutron-rich nuclei have been gathered in recent experiments, but the available information is not sufficient to determine the nature of observed excitations. Even in stable nuclei various modes of giant collective oscillations had been predicted by theory years before they were observed, and for that reason it is very important to perform detailed theoretical studies of the evolution of collective modes of excitation in nuclei far from stability. We therefore discuss the modern theoretical tools that have been developed in recent years for the description of collective excitations in weakly-bound nuclei. The review focuses on the applications of these models to studies of the evolution of low-energy dipole modes from stable nuclei to systems near the particle emission threshold, to analyses of various isoscalar modes, those for which data are already available, as well as those that could be observed in future experiments, to a description of charge-exchange modes and their evolution in neutron-rich nuclei, and to studies of the role of exotic low-energy modes in astrophysical processes.

## Contents

<b>1</b>	<b>Introduction</b>	<b>3</b>
<b>2</b>	<b>Self-Consistent Theory of Small Amplitude Vibrations</b>	<b>5</b>
2.1	The Hartree-Fock-Bogoliubov Method with Effective Nuclear Forces . . .	6
2.2	The Relativistic Hartree-Bogoliubov model (RHB) . . . . .	12
2.3	Continuum QRPA . . . . .	15
2.4	Discrete QRPA . . . . .	18
2.5	Relativistic QRPA . . . . .	20
2.6	Multipole Transition Strength and Transition Densities . . . . .	22
<b>3</b>	<b>Beyond the Mean-Field Approximation</b>	<b>24</b>
3.1	Extensions of the (Q)RPA . . . . .	24
3.2	Illustrative calculations . . . . .	29
<b>4</b>	<b>Low-Energy Electric Dipole Strength</b>	<b>31</b>
4.1	Low-Energy Response of Light Nuclei . . . . .	31
4.2	Low-Energy Dipole Excitations in Oxygen Isotopes . . . . .	34
4.3	Pygmy Dipole Resonances in Heavier Neutron-Rich Nuclei . . . . .	39
4.4	Isotopic Dependence of Pygmy Dipole Resonances . . . . .	50
4.5	The Proton Electric Pygmy Dipole Resonance . . . . .	55
4.6	Di-neutron Correlations near the Drip-Line . . . . .	59
<b>5</b>	<b>Isoscalar Modes</b>	<b>61</b>
5.1	Isoscalar Dipole Compressional and Toroidal Modes . . . . .	61
5.2	Low-Lying Quadrupole States in Unstable Nuclei . . . . .	69
5.3	Giant Quadrupole Resonance and Higher Multipoles . . . . .	75
5.4	Pairing Vibrations in Drip-Line Nuclei . . . . .	77
<b>6</b>	<b>Charge-exchange Resonances</b>	<b>81</b>
6.1	Proton-Neutron QRPA . . . . .	81
6.2	Proton-Neutron Relativistic QRPA . . . . .	84
6.3	Gamow-Teller Resonances . . . . .	85
6.4	Effect of the Dirac Sea on the Gamow-Teller Sum Rule . . . . .	90
6.5	Spin-Isospin Resonances and the Neutron Skin of Nuclei . . . . .	92
<b>7</b>	<b>Exotic Nuclear Modes in Astrophysical Processes</b>	<b>95</b>
7.1	Low-Energy Dipole Strength and the r-process . . . . .	95
7.2	Nuclei as Ultra-High Energy Cosmic Rays . . . . .	102
7.3	Supergiant Resonances in the Inner Crust of Neutron Stars . . . . .	108
<b>8</b>	<b>Concluding Remarks and Outlook</b>	<b>111</b>

## 1. Introduction

Studies of nuclear vibrational modes over several past decades have provided valuable information on the structure of the nucleus and the forces of cohesion that are responsible for the nuclear binding. Collective degrees of freedom characterize many aspects of nuclear structure. The response of a nucleus to external forces often exhibits a degree of simplicity associated with collective modes: rotations and vibrations. Even the simplest excitations, giant vibrations or giant resonances characterized by a coherent oscillation of all the nucleons, probe not only global nuclear properties such as the size, the shape, the distributions of protons and neutrons, the compressibility of nuclear matter, but also the details of the in-medium modification of the nucleon-nucleon interaction, and the interplay between different degrees of freedom in dissipative processes that determine the damping mechanism. The excitation energies and decay properties of giant resonances have been measured mostly for nuclei along the valley of  $\beta$ -stability, and the extension of these studies to regions of unstable nuclei is still in its infancy.

The multipole response of nuclei far from the  $\beta$ -stability line and the possible occurrence of exotic modes of excitation presents a rapidly growing field of research. Characteristic ground-state properties (weak binding of the outermost nucleons, coupling between bound states and the particle continuum, nuclei with very diffuse neutron densities, formation of neutron skin and halo structures) will also have a pronounced effect on the multipole response of unstable nuclei. For instance, the dipole (E1) response of neutron-rich nuclei is characterized by the fragmentation of the strength distribution and its spreading into the low-energy region, and by the mixing of isoscalar and isovector components. While in light nuclei the onset of dipole strength in the low-energy region is caused by non-resonant independent single-particle excitations of the loosely bound neutrons, several theoretical analyses have predicted the existence of the pygmy dipole resonance (PDR) in medium-mass and heavy nuclei, i.e., the resonant oscillation of the weakly-bound neutron skin against the isospin saturated proton-neutron core. The interpretation of the dynamics of the observed low-energy E1 strength in nuclei with a pronounced neutron excess is currently very much under discussion.

Of course, not only pygmy states, but also other possible exotic modes are being studied: isoscalar dipole, toroidal, giant pairing vibrations, low-energy monopole and quadrupole, and spin-isospin excitations in unstable nuclei. The isoscalar giant dipole resonance (ISGDR) corresponds to a second order high-energy compression mode and therefore provides information on the nuclear matter compression modulus, but the existence of a low-energy component has recently been experimentally confirmed. Several theoretical studies have predicted that the low-energy isoscalar dipole vibration is not sensitive to the nuclear compressibility and that, in fact, it could correspond to the toroidal dipole resonance. The toroidal dipole mode is a transverse zero-sound wave and its experimental observation would invalidate the hydrodynamical picture of the nuclear medium, since there is no restoring force for such modes in an ideal fluid.

Pairing vibrations are induced in the nucleus by the addition or removal of a pair of neutrons, and can be associated with the fluctuation of the pairing field. High-energy collective pairing modes – Giant Pairing Vibrations (GPV), have been predicted and analyzed theoretically, but have never been observed in studies of reactions induced by beams of stable isotopes. Entirely new types of collective excitations might arise in nuclei near the particle emission threshold: di-neutron vibrations close to the neutron-drip line, and proton pygmy resonances in proton-rich nuclei. Several new theoretical approaches have recently been developed, which provide a fully microscopic description of low-energy collective excitations in weakly bound nuclei. This review presents an opportunity to compare the results and predictions of various models, and to discuss the development of modern theoretical tools based on the interacting shell-model, the time-dependent non-relativistic and relativistic self-consistent mean-field framework, and the extensions of the latter models beyond the mean-field approximation.

Theoretical predictions of exotic modes have also prompted the design of experiments with radioactive beams, and a number of studies of low-energy multipole response in unstable nuclei have been reported in recent years. Low-lying E1 strength has been observed in neutron-rich oxygen isotopes, exhausting about 10% of the classical dipole sum rule below 15 MeV excitation energy. In heavier systems data have recently been reported on the concentration of electric dipole strength below the neutron separation energy in  $N = 82$  semi-magic nuclei. The experimental information which is presently available, however, is not sufficient to determine the dominant structure of the observed states. The Sn isotopes present another very interesting example of the evolution of the low-lying dipole strength with neutron number. Very recently the dipole strength distribution above the one-neutron separation energy has been measured in the unstable  $^{130}\text{Sn}$  and the doubly-magic  $^{132}\text{Sn}$ . In addition to the giant dipole resonance (GDR), evidence has been reported for a PDR structure at excitation energy around 10 MeV both in  $^{130}\text{Sn}$  and  $^{132}\text{Sn}$ , exhausting a few percent of the E1 energy-weighted sum rule. Obviously this is a rapidly expanding field and many new experiments are being planned and designed at existing or future radioactive-beam facilities, which will allow the study of the evolution of collective modes in nuclei far from stability, and the discovery of new exotic modes of excitation.

Besides being intrinsically interesting as new structure phenomena, exotic modes of excitation might play an important role in nuclear astrophysics. For example, the occurrence of the PDR could have a pronounced effect on neutron capture rates in the r-process nucleosynthesis, and consequently on the calculated elemental abundance distribution. Even though its strength is small compared to the total dipole strength, the PDR significantly enhances the radiative neutron capture cross section on neutron-rich nuclei, as shown in recent large-scale QRPA calculations of the E1 strength for the whole nuclear chart. The latest theoretical and computational advances in nuclear structure modeling have had a strong impact on nuclear astrophysics. More and more often calculations of stellar nucleosynthesis, nuclear aspects of supernova collapse and explosion, and neutrino-induced reactions, are based on microscopic global predictions

for the nuclear ingredients, rather than on phenomenological approaches. The ability to model the Gamow-Teller response, for instance, is essential for reliable predictions of  $\beta$ -decay rates in neutron-rich nuclei along the  $r$ -process path. The calculation of GT strength, however, can also be used to constrain the spin-isospin channel of energy density functionals. When approaching the neutron (proton) drip lines, an increasing fraction of the GT<sub>-</sub> (GT<sub>+</sub>) strength is found within the  $\beta$ -decay window, and a consistent study of this phenomenon has yet to be carried out in the framework of microscopic self-consistent models.

The low-energy E1 strength could also play a role in the photodisintegration of Ultra-High Energy Cosmic Rays (UHECR). Under the assumption that UHECR are extra-Galactic nuclei accelerated to energies up to  $10^{21}$  eV, their interaction with the 2.7 K Cosmic Microwave Background (CMB) leads to photoabsorption reactions, followed by nucleon emission. Recent calculations have shown that the photodisintegration path proceeds through regions of unstable nuclei, and that the nucleon emission rate is very sensitive to the low-energy dipole strength.

The ultimate exotic modes far from stability could be collective excitations in nuclei far beyond the drip-line. Such systems can be expected to exist in the inner crust of neutron stars, where nuclear clusters are immersed in a dilute gas of neutrons and electrons. Model calculations have predicted the existence of super-giant resonances (SGR) at very low energies, typically around 3 MeV, and exhausting more than 70% of the EWSR. The SGR can have a pronounced effect on the specific heat of the crust, and could therefore affect the cooling time of the neutron star.

The most accurate description of nuclear vibrations is provided by the time-dependent mean-field theory, and thus we begin this review with an outline of the theoretical tools which are based on the self-consistent theory of small-amplitude vibrations (Sec. 2), and its extension beyond the mean-field approximation (Sec. 3). An extensive review of recent studies of the evolution of low-energy dipole vibrations, and the possible occurrence of pygmy modes in nuclei far from stability, is presented in Sec. 4. Various isoscalar modes, those already observed in experiments, as well as those that so far have only been predicted in theoretical studies, are reviewed in Sec. 5. A discussion of charge-exchange modes and their evolution in neutron-rich nuclei is included in Sec. 6. The possible role of exotic low-energy modes in astrophysical processes is described in Sec. 7 and, finally, Sec. 8 contains the concluding remarks and ends with an outlook for future studies.

## 2. Self-Consistent Theory of Small Amplitude Vibrations

Modern nuclear structure theory has evolved from macroscopic and microscopic studies of phenomena in stable nuclei towards regions of exotic, short-lived nuclei far from the valley of stability, and nuclear astrophysics applications. The principal challenge is to build a consistent microscopic theoretical framework that will provide a unified description of bulk properties, nuclear excitations and reactions.

The *ab-initio* approach, which starts from accurate two-nucleon and three-nucleon interactions, adjusted to nucleon-nucleon scattering data and spectroscopic data on few-nucleon systems, respectively, provides the basis for a quantitative description of ground-state properties, excited states and transitions in relatively light nuclei with  $A \leq 16$ . Improved shell-model techniques, which employ accurately adjusted effective interactions and sophisticated truncation schemes, are used in large-scale calculations of structure phenomena in medium-mass nuclei, including properties which are relevant for astrophysical applications. The structure of heavy nuclei with a large number of active nucleons, however, is best described in the framework of self-consistent mean-field models. A vast body of data, not only in medium-heavy and heavy stable nuclei, but also in regions of exotic nuclei far from the line of  $\beta$ -stability, has been successfully analyzed with mean-field models based on the Skyrme and Gogny non-relativistic interactions, and on relativistic meson-exchange effective Lagrangians. The self-consistent mean-field approach to nuclear structure represents an approximate implementation of Kohn-Sham density functional theory, which enables a microscopic description of the nuclear many-body problem in terms of a universal energy density functional. When compared with *ab-initio* and shell-model approaches, important advantages of the mean-field framework include the use of global effective nuclear interactions, the ability to describe arbitrarily heavy systems including superheavy nuclei, and the resulting intuitive picture of intrinsic nuclear shapes.

The unique structure properties which characterize highly unstable nuclei as, for instance, the weak binding of the outermost nucleons and the coupling between bound states and the particle continuum, the modification of the effective nuclear potential and the formation of nuclei with very diffuse neutron densities, the occurrence of neutron skin and halo structures, will also affect the multipole response of these systems, and new modes of excitation could arise in nuclei at the limits of stability. Therefore a quantitative description of properties of ground and excited states in weakly-bound nuclei, and especially studies of exotic modes far from stability, necessitate using the time-dependent self-consistent mean-field framework. In this section we present an outline of the theoretical tools that have been employed in most studies included in this article. We start with the non-relativistic Hartree-Fock-Bogoliubov theory, extend this approach to the relativistic mean-field framework, and derive the (continuum) non-relativistic and relativistic quasiparticle random phase approximations in the small-amplitude limit of the self-consistent time-dependent mean-field theory. For a more detailed introduction we refer the reader to several excellent monographs [1, 2, 3, 4, 5, 6], and recent review articles [7, 8].

### 2.1. The Hartree-Fock-Bogoliubov Method with Effective Nuclear Forces

In addition to the self-consistent mean-field single-nucleon potential, the inclusion of pairing correlations is essential for a quantitative description of structure phenomena in open-shell spherical and deformed nuclei. In weakly-bound systems far from stability,

in particular, the Fermi surface for one type of nucleons is found close to the particle continuum. The single-nucleon separation energies become comparable to the pairing gaps, and this results in the lowest particle-hole ( $ph$ ) and particle-particle ( $pp$ ) modes being embedded in the continuum. A unified and self-consistent treatment of both the mean-field and pairing correlations becomes necessary, and the coupling between bound and continuum states has to be taken into account explicitly.

The Hartree-Fock-Bogoliubov (HFB) theory [1, 2] provides a unified description of  $ph$ - and  $pp$ -correlations in nuclei and, when the self-consistent HFB equations are formulated in coordinate space, allows for a treatment of continuum effects in the presence of pairing. In the HFB framework two average potentials are taken into account: the self-consistent Hartree-Fock field  $\hat{\Gamma}$  which encloses all the  $ph$  correlations, and the pairing field  $\hat{\Delta}$  which sums up the effects of the  $pp$  interaction. The ground state of a given nucleus is described by a generalized Slater determinant  $|\Phi\rangle$  of single-quasiparticle self-consistent solutions of the HFB equations, and represents the vacuum with respect to independent quasiparticles. The quasiparticle operators are defined by the unitary Bogoliubov transformation of the single-nucleon creation and annihilation operators:

$$\alpha_k^+ = \sum_l U_{lk} c_l^+ + V_{lk} c_l, \quad (1)$$

where  $U_{lk}$ ,  $V_{lk}$  are single-quasiparticle wave functions that satisfy the HFB equation. The index  $l$  denotes an arbitrary basis, for instance the harmonic oscillator states. In the coordinate space representation  $l \equiv (\mathbf{r}, \sigma, \tau)$ , with the spin-index  $\sigma$  and the isospin index  $\tau$ . The HFB wave functions determine the hermitian single-particle density matrix

$$\hat{\rho}_{ll'} = \langle \Phi | c_{l'}^+ c_l | \Phi \rangle = (V^* V^T)_{ll'}, \quad (2)$$

and the antisymmetric pairing tensor

$$\hat{\kappa}_{ll'} = \langle \Phi | c_{l'} c_l | \Phi \rangle = (V^* U^T)_{ll'}. \quad (3)$$

These two densities can be combined into the generalized density matrix

$$\mathcal{R} = \begin{pmatrix} \rho & \kappa \\ -\kappa^* & 1 - \rho^* \end{pmatrix}. \quad (4)$$

For a nuclear Hamiltonian of the form

$$\hat{H} = \sum_l \varepsilon_l c_l^+ c_l + \frac{1}{4} \sum_{ll'mm'} \tilde{v}_{ll'mm'} c_l^+ c_m^+ c_m c_{l'}, \quad (5)$$

where  $\tilde{v}$  denotes a general nucleon-nucleon interaction, the expectation value  $\langle \Phi | \hat{H} | \Phi \rangle$  can be expressed as a function of the hermitian density matrix  $\hat{\rho}$ , and the antisymmetric pairing tensor  $\hat{\kappa}$ . The minimization of this energy functional with respect to  $\hat{\rho}$  and  $\hat{\kappa}$  leads to the Hartree-Fock-Bogoliubov equations

$$\begin{pmatrix} \hat{h} - \lambda & \hat{\Delta} \\ -\hat{\Delta}^* & -\hat{h}^* + \lambda \end{pmatrix} \begin{pmatrix} U_k \\ V_k \end{pmatrix} = E_k \begin{pmatrix} U_k \\ V_k \end{pmatrix}. \quad (6)$$

The single-nucleon Hamiltonian reads  $\hat{h} = \hat{\varepsilon} + \hat{\Gamma}$ , and the two self-consistent potentials  $\hat{\Gamma}$  and  $\hat{\Delta}$  are defined by

$$\hat{\Gamma}_{ll'} = \sum_{mm'} \tilde{v}_{lm'l'm} \hat{\rho}_{mm'} , \quad (7)$$

and

$$\hat{\Delta}_{ll'} = \sum_{m < m'} \tilde{v}_{ll'mm'} \hat{\kappa}_{mm'} . \quad (8)$$

The chemical potential  $\lambda$  is determined by the particle number subsidiary condition, in such a way that the expectation value of the particle number operator in the ground state equals the given number of nucleons. The column vectors denote the quasiparticle wave functions, and  $E_k$  are the corresponding quasiparticle energies.

In the framework of Kohn-Sham density functional theory (DFT) [9, 10, 11], of which the self-consistent HFB represents a particular implementation, the nuclear many-body problem is defined in terms of a universal energy density functional. Self-consistent mean-field models approximate the exact energy functional, which includes all higher-order correlations, with powers and gradients of ground-state nucleon densities. Although it models the effective interaction between nucleons, a general density functional is not necessarily related to any given microscopic nucleon-nucleon potential, i.e. it is rather the density functional that defines the effective nuclear interaction. This means that in the DFT formulation of the HFB framework one does not start with a Hamiltonian defined by a two-body interaction as in Eq. (5), but rather from the energy functional  $E[\mathcal{R}] = E[\hat{\rho}, \hat{\kappa}]$  that depends on the densities  $\hat{\rho}$  and  $\hat{\kappa}$ . The generalized Hamiltonian  $\mathcal{H}$  is then obtained as a functional derivative of the energy with respect to the generalized density:

$$\mathcal{H} = \frac{\delta E}{\delta \mathcal{R}} = \begin{pmatrix} \hat{h} & \hat{\Delta} \\ -\hat{\Delta}^* & -\hat{h}^* \end{pmatrix} , \quad (9)$$

where the single particle Hamiltonian  $\hat{h}$  results from the variation of the energy functional with respect to the hermitian density matrix  $\hat{\rho}$

$$\hat{h} = \frac{\delta E}{\delta \hat{\rho}} , \quad (10)$$

and the pairing field is obtained from the variation of the energy functional with respect to the pairing tensor

$$\hat{\Delta} = \frac{\delta E}{\delta \hat{\kappa}} . \quad (11)$$

In a compact form the stationary HFB equation is given in terms of the generalized density:

$$[\mathcal{H}, \mathcal{R}] = 0 . \quad (12)$$

In principle, a universal energy density functional can be built as an expansion in terms of local densities and currents, including all terms allowed by the underlying



symmetries, and without direct reference to any specific nucleon-nucleon interaction. By employing global effective nuclear interactions, with a small set of parameters adjusted to reproduce empirical properties of symmetric and asymmetric nuclear matter, and bulk properties of few stable spherical nuclei, the current generation of self-consistent mean-field models has achieved a high level of accuracy in the description of ground states and properties of excited states in arbitrarily heavy nuclei, including rare isotopes with a large neutron to proton asymmetry. In the non-relativistic framework, in particular, two classes of effective nucleon-nucleon interactions have become standard in self-consistent Hartree-Fock and Hartree-Fock-Bogoliubov calculations. The first is the finite-range Gogny force [12, 13]:

$$\begin{aligned} \hat{v}_{\text{Gogny}}(\mathbf{r}_{12}) = & \sum_{j=1}^2 e^{-(\mathbf{r}_{12}/\mu_j)^2} (W_j + B_j \hat{P}_\sigma - H_j \hat{P}_\tau - M_j \hat{P}_\sigma \hat{P}_\tau) \\ & + t_3 (1 + x_0 \hat{P}_\sigma) \delta(\mathbf{r}_{12}) \rho^\alpha \left( \frac{\mathbf{r}_1 + \mathbf{r}_2}{2} \right) \\ & + iW_{ls} (\hat{\sigma}_1 + \hat{\sigma}_2) \cdot \hat{\mathbf{k}}^\dagger \times \delta(\mathbf{r}_{12}) \hat{\mathbf{k}} \end{aligned} \quad (13)$$

where  $\hat{P}_\sigma = \frac{1}{2}(1 + \hat{\sigma}_1 \cdot \hat{\sigma}_2)$  is the spin-exchange operator,  $\hat{P}_\tau = \frac{1}{2}(1 + \hat{\tau}_1 \cdot \hat{\tau}_2)$  the isospin exchange operator,  $\mathbf{r}_{12} = \mathbf{r}_1 - \mathbf{r}_2$ , and  $\hat{\mathbf{k}} = -\frac{i}{2}(\nabla_1 - \nabla_2)$ . The interaction includes the sum of two Gaussians with space, spin and isospin exchange, the term which includes an explicit density dependence, and the spin-orbit term.  $W_j$ ,  $B_j$ ,  $H_j$ ,  $M_j$ ,  $\mu_j$ ,  $t_3$ ,  $x_0$ ,  $\alpha$  and  $W_{ls}$  are adjustable parameters of the interaction.

The second class of effective interactions is based on the zero-range, momentum-dependent Skyrme force:

$$\begin{aligned} \hat{v}_{\text{Sk}}(\mathbf{r}_{12}) = & t_0 (1 + x_0 \hat{P}_\sigma) \delta(\mathbf{r}_{12}) \\ & + \frac{1}{2} t_1 (1 + x_1 \hat{P}_\sigma) \left( \hat{\mathbf{k}}^{\dagger 2} \delta(\mathbf{r}_{12}) + \delta(\mathbf{r}_{12}) \hat{\mathbf{k}}^2 \right) \\ & + t_2 (1 + x_2 \hat{P}_\sigma) \hat{\mathbf{k}}^\dagger \cdot \delta(\mathbf{r}_{12}) \hat{\mathbf{k}} \\ & + \frac{1}{6} t_3 (1 + x_3 \hat{P}_\sigma) \delta(\mathbf{r}_{12}) \rho^\alpha \left( \frac{\mathbf{r}_1 + \mathbf{r}_2}{2} \right) \\ & + iW_0 (\hat{\sigma}_1 + \hat{\sigma}_2) \cdot \hat{\mathbf{k}}^\dagger \times \delta(\mathbf{r}_{12}) \hat{\mathbf{k}} . \end{aligned} \quad (14)$$

Standard Skyrme interactions include ten adjustable parameters which determine the central term, the velocity dependent terms, the density dependent term, and the spin-orbit term [7, 14, 15, 16]. The Skyrme energy density functional can be derived from the Hartree-Fock expectation value of the zero-range momentum dependent two-body force Eq. (14), or it can be parameterized directly without reference to an effective two-body force [7]. In the latter case the universal functional contains systematically all possible bilinear terms in the local densities and currents (plus derivative terms) which are invariant with respect to parity, time-reversal, rotational, translational and isospin transformations.

The pairing field in Eq. (8) is determined by the effective interaction in the pairing channel. In applications of the HFB model with the Gogny force, the same effective

interaction is used both in the  $ph$  and  $pp$  channels, with the exception of the density-dependent zero-range term which, with the choice of the parameter  $x_0 = 1$ , does not contribute to the pairing channel. There is no physical reason, however, to use identical terms of the energy density functional in the the mean-field and pairing channels. Skyrme-type forces, for instance, generally exhibit unrealistic pairing properties, and thus an additional effective pairing interaction has to be specified in Skyrme-HFB calculations of open-shell nuclei. A standard choice for the pairing interaction is a zero-range local force, often including an explicit density-dependence:

$$v_{\text{pair}}(\mathbf{r}_{12}) = \frac{V_0}{2} (1 - \hat{P}_\sigma) \left[ 1 - \eta \left( \frac{\rho(\mathbf{r}_1)}{\rho_c} \right)^\beta \right] \delta(\mathbf{r}_1 - \mathbf{r}_2). \quad (15)$$

Depending on the value of the parameters  $\eta$ ,  $\rho_c$  and  $\beta$ , pairing is more active in the volume of the nucleus, or on its surface. The strength  $V_0$  is adjusted to reproduce the odd-even staggering of binding energies in selected isotopic chains. Usually this results in slightly different values of the pairing strengths for protons and neutrons, thus breaking the isospin invariance of the pairing energy functional.

For nuclear systems with time-reversal invariance, the HFB method can be considerably simplified by employing the Bardeen-Cooper-Schrieffer (BCS) approximation. In the BCS approximation the pairing potential  $\hat{d}$ , defined by the relation:

$$\hat{\Delta} = \begin{pmatrix} 0 & \hat{d} \\ -\hat{d}^T & 0 \end{pmatrix}, \quad (16)$$

where  $\hat{\Delta}$  is the pairing field of Eq. (8), is diagonal in the basis of the eigenstates of the mean-field Hamiltonian  $\hat{h}$

$$d_{n\bar{m}} = \delta_{nm} d_{n\bar{n}}, \quad \hat{h}\varphi_n = \varepsilon_n \varphi_n, \quad (17)$$

and  $\bar{m}$  ( $\bar{n}$ ) denotes the time-conjugate partner of the single-particle state  $m$  ( $n$ ). The resulting two-component HFB wave functions read  $U_n = u_n \varphi_n$  and  $V_n = v_n \varphi_n$ , and the occupation amplitudes  $(u_n, v_n)$  are determined by the gap equation

$$(\varepsilon_n - \lambda)(u_n^2 - v_n^2) + 2d_{n\bar{n}} u_n v_n = 0, \quad (18)$$

and the normalization condition:

$$u_n^2 + v_n^2 = 1. \quad (19)$$

In the case of well-bound nuclei close to the stability line, pairing correlations are often treated in the BCS approximation, with the strength of the pairing force adjusted to the experimental odd-even mass differences. This approach, however, presents only a poor approximation for weakly-bound nuclei far from the valley of  $\beta$ -stability. In particular, for nuclei at the limits of particle stability (drip-line nuclei), the Fermi level lies close to the continuum, and the coupling between bound and continuum states has to be taken into account explicitly. The BCS model does not provide a correct description of the scattering of nucleonic pairs from bound states to the positive energy continuum,

and as a result levels high in the continuum become partially occupied. Including the system in a box of finite size, i.e. solving the HFB equations in coordinate space, leads to unreliable predictions for quantities that crucially depend on the size of the box, e.g. nuclear radii. The reason is that in the BCS approximation the pairing field does not vanish asymptotically. Thus for weakly-bound nuclei the full HFB theory, including the continuum, has to be employed [17, 18].

The asymptotic behavior of the HFB wave function is determined by the physical condition that at large distances from a nucleus the mean field  $\Gamma(\mathbf{r})$  and the pairing field  $\Delta(\mathbf{r})$  vanish. For a bound system (negative chemical potential  $\lambda < 0$ ), two distinct regions characterize the quasiparticle spectrum. This is illustrated in Figure 1. Between 0 and  $-\lambda$  the quasiparticle spectrum is discrete and both the upper and lower components of the radial HFB wave function decay exponentially at  $r \rightarrow \infty$ . In the continuum region above  $-\lambda$  one finds two types of HFB quasiparticle resonant

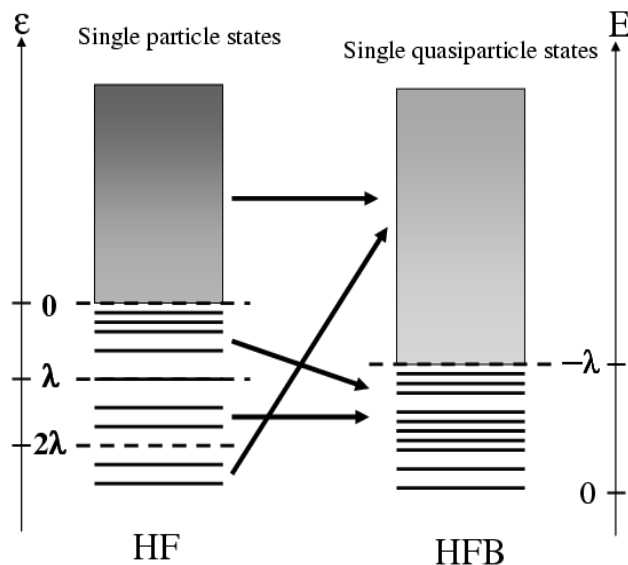


**Figure 1.** Illustrative representation of single-particle (left) and single-quasiparticle (right) spectra.  $\lambda$  is the chemical potential. The arrows depict the correspondence between the single-particle states and the single-quasiparticle states in the discrete and continuous regions of the spectra.

states. First, those which correspond to the single-particle resonances of the mean field. The low-lying single-particle resonances are particularly important in the treatment of pairing correlations of weakly-bound nuclei, because the pairing interaction scatters pairs of nucleons into positive-energy states above the particle threshold. A second type of resonant states is specific to the HFB method, and originates from bound single-particle states which, in the absence of pairing correlations, are found at energies  $\epsilon < 2\lambda$ . With the inclusion of the pairing field these bound states couple with the continuum single-particle states and, therefore, acquire finite widths.

The HFB equations are usually solved by imposing box boundary conditions,

i.e. the HFB wave functions are assumed to vanish beyond some distance, usually chosen to be a few times the nuclear radius. The energy continuum is thus replaced by a spectrum of discrete energies, whose density increases with the size of the box. Continuum HFB calculations can be performed either in the complex energy plane by employing Green's function techniques [19], or on the real energy axis [17, 18]. It is possible to treat the continuum exactly in HFB calculations on the real energy axis, by imposing the correct boundary conditions for the HFB wave functions  $U_k$  and  $V_k$  [20]. Far from the nuclear potential, the  $U_k$  and  $V_k$  which belong to the single quasiparticle continuum ( $E_k > -\lambda$ ), take the asymptotic form of a scattering state and a function that exponentially decreases at infinity, respectively. These asymptotic forms must, of course, be matched with the corresponding radial functions in the inner region of the potential. By comparing the exact treatment of the continuum with different levels of approximation (discretization in a box, HF-BCS including the resonant part of the continuum), it has been shown that the different ways in which the coupling to the continuum is treated in HFB strongly affect the resulting pairing correlations in nuclei close to the particle drip-lines.

## 2.2. The Relativistic Hartree-Bogoliubov model (RHB)

Self-consistent mean-field models based on the relativistic mean-field theory (RMF) [21, 22], have been very successfully employed in analyses of a variety of nuclear structure phenomena, not only in nuclei along the valley of  $\beta$ -stability, but also in exotic nuclei with extreme isospin values and close to the particle drip-lines. RMF-based models have reached a level of sophistication and accuracy comparable to the non-relativistic Hartree-Fock-Bogoliubov framework based on Skyrme and Gogny effective interactions [8].

Most applications have used the finite-range meson-exchange representation of the RMF theory, in which the nucleus is described as a system of Dirac nucleons coupled to effective mesons and the electromagnetic field. A medium dependence of the effective interaction can be introduced either by including non-linear meson self-interaction terms in the Lagrangian, or by assuming an explicit density dependence for the meson-nucleon couplings [8]. An alternative RMF representation is formulated in terms of point-coupling (PC) (contact) nucleon-nucleon interactions [23], without the inclusion of meson fields. The medium dependence of the interaction can be taken into account by terms of higher-order in the nucleon fields, or it can be encoded into the effective couplings, i.e. in the strength parameters of the interaction in the isoscalar and isovector channels. On the phenomenological level, when applied in studies of properties of finite nuclei, the meson-exchange and nucleon point-coupling representations produce results of comparable quality. The applications reviewed in this article are based on the finite-range meson-exchange picture of effective nuclear interactions, and in the following we outline its basic features.

The isoscalar scalar  $\sigma$ -meson, the isoscalar vector  $\omega$ -meson, and the isovector vector  $\rho$ -meson form the minimal set of meson fields which, together with the electromagnetic

field, are necessary for a quantitative description of bulk nuclear properties. The model is defined by the Lagrangian density

$$\mathcal{L} = \mathcal{L}_N + \mathcal{L}_m + \mathcal{L}_{int}. \quad (20)$$

$\mathcal{L}_N$  is the Lagrangian of the free nucleon

$$\mathcal{L}_N = \bar{\psi} (i\gamma^\mu \partial_\mu - m) \psi, \quad (21)$$

$m$  is the bare nucleon mass and  $\psi$  denotes the Dirac spinor.  $\mathcal{L}_m$  is the Lagrangian of the free  $\sigma$ ,  $\omega$  and  $\rho$  meson fields, and the electromagnetic field

$$\begin{aligned} \mathcal{L}_m = & \frac{1}{2} \partial_\mu \sigma \partial^\mu \sigma - \frac{1}{2} m_\sigma^2 \sigma^2 - \frac{1}{4} \Omega_{\mu\nu} \Omega^{\mu\nu} + \frac{1}{2} m_\omega^2 \omega_\mu \omega^\mu \\ & - \frac{1}{4} \vec{R}_{\mu\nu} \vec{R}^{\mu\nu} + \frac{1}{2} m_\rho^2 \vec{\rho}_\mu \vec{\rho}^\mu - \frac{1}{4} F_{\mu\nu} F^{\mu\nu}, \end{aligned} \quad (22)$$

with the corresponding masses  $m_\sigma$ ,  $m_\omega$ ,  $m_\rho$ . The field tensors  $\Omega_{\mu\nu}$ ,  $\vec{R}_{\mu\nu}$ ,  $F_{\mu\nu}$  read

$$\begin{aligned} \Omega_{\mu\nu} &= \partial_\mu \omega_\nu - \partial_\nu \omega_\mu \\ \vec{R}_{\mu\nu} &= \partial_\mu \vec{\rho}_\nu - \partial_\nu \vec{\rho}_\mu \\ F_{\mu\nu} &= \partial_\mu A_\nu - \partial_\nu A_\mu, \end{aligned} \quad (23)$$

where arrows denote isovector quantities. The minimal set of interaction terms is contained in

$$\mathcal{L}_{int} = -\bar{\psi} \Gamma_\sigma \sigma \psi - \bar{\psi} \Gamma_\omega^\mu \omega_\mu \psi - \bar{\psi} \vec{\Gamma}_\rho^\mu \vec{\rho}_\mu \psi - \bar{\psi} \Gamma_e^\mu A_\mu \psi, \quad (24)$$

where the vertices read

$$\Gamma_\sigma = g_\sigma, \quad \Gamma_\omega^\mu = g_\omega \gamma^\mu, \quad \vec{\Gamma}_\rho^\mu = g_\rho \vec{\tau} \gamma^\mu, \quad \Gamma_e^\mu = e \frac{1 - \tau_z}{2} \gamma^\mu, \quad (25)$$

with the coupling parameters  $g_\sigma$ ,  $g_\omega$ ,  $g_\rho$  and  $e$ . The phenomenological  $\sigma$ -meson approximates a large attractive scalar field that results from complicated microscopic processes, such as uncorrelated and correlated two-pion exchange. The  $\omega$ -meson describes the short-range repulsion between the nucleons, and the  $\rho$ -meson carries the isospin quantum number. The latter is required by the large empirical asymmetry potential in finite nuclear systems. Because of parity conservation there is no direct contribution from the pion field. The self-consistent RMF approach represents a particular realization of the relativistic Kohn-Sham density functional theory [10, 11], in which one attempts to effectively include in the nuclear energy density functional effects which go beyond the Hartree approximation (Fock terms, short-range correlations, vacuum-polarization effects). The many-body correlations of the energy density functional can be represented by a medium dependence of the corresponding effective nuclear interaction. An effective density dependence can be included, for instance, through meson self-interaction terms. Over the years a number of non-linear meson-exchange interactions have been adjusted to the nuclear matter equation of state and bulk properties of a set of spherical closed-shell nuclei, and applied in the description of nuclear properties along the  $\beta$ -stability line. One of the most successful phenomenological interactions of this type is the non-linear parameter set NL3 [24],

which has been employed in many studies of ground-state properties and collective excitations both in stable nuclei and in exotic systems far from the line of  $\beta$ -stability.

Another class of medium-dependent effective interactions is characterized by an explicit baryon-density dependence of the meson-nucleon vertices. Such an approach retains the basic structure of the relativistic mean-field framework, but can be more directly related to the underlying microscopic description of nuclear interactions. The functional form of the meson-nucleon vertices can be deduced from in-medium Dirac-Brueckner interactions, obtained from realistic free-space NN interactions, or a phenomenological approach can be adopted, with the density dependence for the  $\sigma$ ,  $\omega$  and  $\rho$  meson-nucleon couplings adjusted to properties of nuclear matter and a set of spherical nuclei. The former represents an *ab-initio* description of nuclear matter and finite nuclei, and the corresponding density-dependent relativistic mean-field model has also been applied to asymmetric nuclear matter and exotic nuclei [25]. In the latter approach very accurate phenomenological density-dependent relativistic effective interactions have recently been adjusted [26, 27, 28], and employed in analyses of both bulk nuclear properties and collective excitations. A number of recent studies have shown that, in comparison with non-linear meson self-interactions, relativistic models with an explicit density dependence of the meson-nucleon couplings provide an improved description of asymmetric nuclear matter, neutron matter and nuclei far from stability.

An extensive review of the relativistic extension of the HFB theory – the relativistic Hartree-Bogoliubov (RHB) model – including numerous applications, can be found in Ref. [8]. In this framework the ground state of an open-shell nucleus is determined by the single-quasiparticle solutions of the RHB equations (cf. also Eq. (6)):

$$\begin{pmatrix} \hat{h}_D - m - \lambda & \hat{\Delta} \\ -\hat{\Delta}^* & -\hat{h}_D^* + m + \lambda \end{pmatrix} \begin{pmatrix} U_k(\mathbf{r}) \\ V_k(\mathbf{r}) \end{pmatrix} = E_k \begin{pmatrix} U_k(\mathbf{r}) \\ V_k(\mathbf{r}) \end{pmatrix}. \quad (26)$$

The self-consistent mean field  $\hat{h}_D$  is the Dirac Hamiltonian determined by the Lagrangian density of Eq. (20),  $\hat{\Delta}$  denotes the pairing field, and  $(U_k, V_k)$  are quasiparticle spinors. Pairing effects in nuclei are restricted to a narrow window of a few MeV around the Fermi level, and their scale is well separated from the scale of binding energies which are in the range of several hundred to thousand MeV. There is no empirical evidence for any relativistic effect in the nuclear pairing field and, therefore, pairing can be treated as a non-relativistic phenomenon. In most applications of the RHB model for spherical and deformed nuclei the Gogny force (cf. Eq. (13)) has been employed in the *pp* channel.

The RHB equations are solved self-consistently, with mean-field potentials in the particle-hole channel determined from solutions of the stationary Klein-Gordon equations

$$[-\Delta + m_\sigma^2] \sigma(\mathbf{r}) = -g_\sigma(\rho_v) \rho_s(\mathbf{r}) \quad (27)$$

$$[-\Delta + m_\omega^2] \omega^0(\mathbf{r}) = g_\omega(\rho_v) \rho_v(\mathbf{r}) \quad (28)$$

$$[-\Delta + m_\rho^2] \rho^0(\mathbf{r}) = g_\rho(\rho_v) \rho_3(\mathbf{r}) \quad (29)$$

$$-\Delta A^0(\mathbf{r}) = e \rho_p(\mathbf{r}) \quad (30)$$

for the  $\sigma$ -meson, the  $\omega$ -meson, the  $\vec{\rho}$ -meson and the photon field, respectively. Because of charge conservation, only the 3-rd component of the isovector  $\rho$ -meson contributes. For the ground-state solution of an even-even nucleus there are no contributions from currents (time-reversal invariance) and the spatial components  $\boldsymbol{\omega}$ ,  $\boldsymbol{\rho}_3$ ,  $\mathbf{A}$  of the vector fields vanish. The source terms in equations (27) to (30) are sums of bilinear products of baryon amplitudes

$$\rho_s(\mathbf{r}) = \sum_{k>0} V_k^\dagger(\mathbf{r}) \gamma^0 V_k(\mathbf{r}) \quad (31)$$

$$\rho_v(\mathbf{r}) = \sum_{k>0} V_k^\dagger(\mathbf{r}) V_k(\mathbf{r}) \quad (32)$$

$$\rho_3(\mathbf{r}) = \sum_{k>0} V_k^\dagger(\mathbf{r}) \tau_3 V_k(\mathbf{r}) \quad (33)$$

$$\rho_{\text{em}}(\mathbf{r}) = \sum_{k>0} V_k^\dagger(\mathbf{r}) \frac{1 - \tau_3}{2} V_k(\mathbf{r}), \quad (34)$$

where the summation is performed only over occupied orbitals of positive energy. This is the *no-sea* approximation, in which the Dirac sea of negative-energy states does not contribute to the densities and currents in an explicit way. The self-consistent solution of the Dirac-Hartree-Bogoliubov integro-differential equations and Klein-Gordon equations for the meson fields determines the ground state of a nucleus.

### 2.3. Continuum QRPA

Small amplitude collective excitations of arbitrarily heavy nuclei can be accurately described by the random phase approximation (RPA) or, in the case of open-shell nuclei, by the quasiparticle random phase approximation (QRPA) [1, 2, 4, 5, 6]. As it has been already emphasized in the introduction to this section, a quantitative description of ground-states and excitations in weakly-bound nuclei characterized by the closeness of the Fermi surface to the particle continuum, must take into account the effects of the coupling between bound states and the particle continuum. Here we derive the QRPA response based on the continuum HFB description of the nuclear ground state in the coordinate space representation, which is naturally suitable for the treatment of the coupling to continuum states [29, 30]. The QRPA represents the small amplitude limit of the general time-dependent (TD) HFB theory, and we therefore start from the HFB equation which describes the response of the generalized density matrix to an external periodic perturbation [1]:

$$i\hbar \frac{\partial \mathcal{R}}{\partial t} = [\mathcal{H}(t) + \mathcal{F}(t), \mathcal{R}(t)]. \quad (35)$$

$\mathcal{R}$  and  $\mathcal{H}$  are the time-dependent generalized density and HFB Hamiltonian, respectively, and  $\mathcal{F}$  is the external periodic perturbation given by

$$\mathcal{F} = F e^{-i\omega t} + \text{h.c.} \quad (36)$$

In the presence of pairing correlations, the fluctuating field  $F$  in Eq. (36) is a generalized one-body operator which includes both particle-hole and two-particle transfer operators

$$F = \sum_{ij} F_{ij}^{11} c_i^\dagger c_j + \sum_{ij} (F_{ij}^{12} c_i^\dagger c_j^\dagger + F_{ij}^{21} c_i c_j), \quad (37)$$

and  $c_i^\dagger$ ,  $c_i$  are the single-particle creation and annihilation operators, respectively. We assume that the external field induces small oscillations around the stationary solution of the HFB equation (12), which we denote here as  $\mathcal{R}^0$  ( $\mathcal{H}^0$  being the corresponding Hamiltonian). Accordingly,

$$\mathcal{R}(t) = \mathcal{R}^0 + \mathcal{R}' e^{-i\omega t} + \text{h.c.}, \quad (38)$$

$$\mathcal{H}(t) = \mathcal{H}^0 + \mathcal{H}' e^{-i\omega t} + \text{h.c.}, \quad (39)$$

and the TDHFB equation (35) becomes

$$\hbar\omega \mathcal{R}' = [\mathcal{H}', \mathcal{R}^0] + [\mathcal{H}^0, \mathcal{R}'] + [F, \mathcal{R}^0]. \quad (40)$$

The variation of the generalized density has the form

$$\mathcal{R}' = \begin{pmatrix} \rho' & \kappa' \\ \bar{\kappa}' & -\rho' \end{pmatrix}, \quad (41)$$

where  $\rho'_{ij} = \langle 0 | c_j^\dagger c_i |' \rangle$  is the variation of the particle density,  $\kappa'_{ij} = \langle 0 | c_j c_i |' \rangle$  and  $\bar{\kappa}'_{ij} = \langle 0 | c_j^\dagger c_i^\dagger |' \rangle$  are the corresponding fluctuations of the pairing tensor, and  $|' \rangle$  denotes the change in the ground-state wavefunction  $|0\rangle$  caused by the external field. Instead of the variation of just one quantity ( $\rho'$ ) as in RPA, in QRPA we must specify the variations of three independent quantities, namely  $\rho'$ ,  $\kappa'$  and  $\bar{\kappa}'$ . If we use the notation

$$\boldsymbol{\rho}' \equiv \begin{pmatrix} \rho' \\ \kappa' \\ \bar{\kappa}' \end{pmatrix}, \quad (42)$$

for the density variations, the corresponding variation of the HFB Hamiltonian reads

$$\mathcal{H}' = \mathbf{V} \boldsymbol{\rho}', \quad (43)$$

where  $\mathbf{V}$  is the matrix of the residual interaction, expressed in terms of the second derivatives of the HFB energy functional  $E$ , defined in Sec. 2.1

$$\mathbf{V}^{\alpha\beta}(\mathbf{r}\sigma\tau, \mathbf{r}'\sigma'\tau') = \frac{\partial^2 E}{\partial \rho_\beta(\mathbf{r}'\sigma'\tau') \partial \rho_{\bar{\alpha}}(\mathbf{r}\sigma\tau)}, \quad \alpha, \beta = 1, 2, 3. \quad (44)$$

Here the notation  $\bar{\alpha}$  means that whenever  $\alpha$  is 2 or 3, then  $\bar{\alpha}$  is 3 or 2. In this three dimensional space, the first dimension represents the particle-hole ( $ph$ ) subspace, the second one the particle-particle ( $pp$ ), and the third one the hole-hole ( $hh$ ) subspace.

The QRPA Green's function  $\mathbf{G}$  relates the perturbing external field to the density variations

$$\boldsymbol{\rho}' = \mathbf{G} \mathbf{F}, \quad (45)$$



where  $\mathbf{F}$  is the three dimensional column vector

$$\mathbf{F} = \begin{pmatrix} F^{11} \\ F^{12} \\ F^{21} \end{pmatrix}. \quad (46)$$

$\mathbf{G}$  is the solution of the Bethe-Salpeter equation

$$\mathbf{G} = (\mathbf{1} - \mathbf{G}_0 \mathbf{V})^{-1} \mathbf{G}_0 = \mathbf{G}_0 + \mathbf{G}_0 \mathbf{V} \mathbf{G}, \quad (47)$$

and the unperturbed Green's function  $\mathbf{G}_0$  reads

$$\mathbf{G}_0^{\alpha\beta}(\mathbf{r}\sigma\tau, \mathbf{r}'\sigma'\tau'; \omega) = \sum_{ij} \frac{\mathcal{U}_{ij}^{\alpha 1}(\mathbf{r}\sigma\tau) \bar{\mathcal{U}}_{ij}^{*\beta 1}(\mathbf{r}'\sigma'\tau')}{\hbar\omega - (E_i + E_j) + i\eta} - \frac{\mathcal{U}_{ij}^{\alpha 2}(\mathbf{r}\sigma\tau) \bar{\mathcal{U}}_{ij}^{*\beta 2}(\mathbf{r}'\sigma'\tau')}{\hbar\omega + (E_i + E_j) + i\eta}, \quad (48)$$

where  $E_i$  are the quasiparticle energies and  $\mathcal{U}_{ij}$  are 3 by 2 matrices expressed in terms of the two components  $U$  and  $V$  of the HFB wave functions

$$\mathcal{U}_{ij}(\mathbf{r}\sigma) = \begin{pmatrix} U_i(\mathbf{r}\sigma)V_j(\mathbf{r}\sigma) & U_j^*(\mathbf{r}\sigma)V_i^*(\mathbf{r}\sigma) \\ U_i(\mathbf{r}\sigma)U_j(\mathbf{r}\bar{\sigma}) & V_i^*(\mathbf{r}\sigma)V_j^*(\mathbf{r}\bar{\sigma}) \\ -V_i(\mathbf{r}\sigma)V_j(\mathbf{r}\bar{\sigma}) & -U_i^*(\mathbf{r}\sigma)U_j^*(\mathbf{r}\bar{\sigma}) \end{pmatrix}, \quad (49)$$

with the notation  $f(\mathbf{r}\bar{\sigma}) = -2\sigma f(\mathbf{r} - \sigma)$ . The  $\sum$  symbol in Eq. (48) indicates that the summation is taken both over discrete and continuum quasiparticle states, i.e., the unperturbed Green's function  $\mathbf{G}_0$  takes into account the resonant states. This can be done either in the complex plane by integrating on a contour [30], or on the real axis by integrating the resonant states with the corresponding widths [29].

$\mathbf{G}_0$  in Eq. (48) is constructed from the solutions of the HFB equations, i.e. the quasiparticle energies and the corresponding wave functions  $U$  and  $V$ . For a given residual interaction in Eq. (44),  $\mathbf{G}$  is then calculated from the Bethe-Salpeter equation (47).  $\mathbf{G}$  can be used for calculating the strength functions associated with various external perturbations. For instance, in the case of transitions from the ground-state to excited states within the same nucleus, only the  $(ph, ph)$  component of  $\mathbf{G}$  is acting. If the interaction does not depend on spin variables, the strength function is then given by

$$S(\omega) = -\frac{1}{\pi} \text{Im} \int F^{11*}(\mathbf{r}) \mathbf{G}^{11}(\mathbf{r}, \mathbf{r}'; \omega) F^{11}(\mathbf{r}') d\mathbf{r} d\mathbf{r}' \quad (50)$$

where  $\mathbf{G}^{11}$  is the  $(ph, ph)$  component of the QRPA Green's function. Examples of such calculations can be found in Refs. [29, 30].

It should be noted that generally the notation includes the neutron-proton formalism, i.e. each supermatrix  $(\mathbf{G}_0, \mathbf{G}, \mathbf{V})$  consists of nine blocks which correspond to the  $ph$ ,  $pp$ ,  $hh$  channels, and each of these blocks is further divided into four sub-blocks corresponding to the neutron-neutron, neutron-proton, proton-neutron and proton-proton channels, respectively.

An important point that must be emphasized is the issue of self-consistency. Namely, since the characteristic ground-state properties of weakly-bound nuclei strongly influence the multipole response of these systems, it is particularly important that for

the QRPA residual interactions, both in  $ph$  and  $pp$  channels, the same interactions are used which also determine the ground-state solutions of the HFB equations.

It is, however, difficult to achieve full self-consistency in continuum RPA or QRPA calculations with Skyrme forces. While the zero-range terms of the interaction do not present any particular problem, the velocity-dependent terms introduce serious technical difficulties that are often avoided by approximating the residual interaction in the  $(ph, ph)$  subspace by its Landau-Migdal limit, in which the momenta of the interacting particle and hole are equal to the Fermi momentum, and the transferred momentum is zero. Taking the Landau-Migdal form for the  $ph$  interaction simplifies the numerical task considerably, however at the cost of losing the full self-consistency. This deficiency of the QRPA approach is cured by renormalizing the residual interaction. It should be noted, however, that an exact treatment of continuum effects within the general framework of the fully self-consistent QRPA is presently not available.

#### 2.4. Discrete QRPA

In addition to the linear response formalism based on Green's functions, the QRPA can also be formulated in a discrete basis. We therefore start from Eq. (40), and choose a discrete basis of two-quasiparticle configurations  $|kl\rangle \equiv \alpha_k^\dagger \alpha_l^\dagger |0\rangle$ , where  $\alpha^\dagger$  is a quasiparticle creation operator and  $|0\rangle$  is the quasiparticle vacuum. The energy of the configuration  $|kl\rangle$  is  $E_k + E_l$ . The quasiparticle space consists of discrete states, even when it describes configurations in the continuum. This discretization is achieved either by enclosing the nuclear system in a finite box, or by expanding the HFB wave functions in a discrete basis, e.g., in terms of eigenfunctions of a harmonic oscillator potential. In a QRPA description of transitions to low-lying excited states in open-shell weakly-bound nuclei, in particular, the two-quasiparticle configuration space must include states with both nucleons in discrete bound levels, states with one nucleon in a bound level and one nucleon in the continuum, and also states with both nucleons in the continuum.

The QRPA equation is obtained by taking the matrix elements of Eq. (40) between  $\langle kl|$  and  $|0\rangle$ , and then also between  $\langle 0|$  and  $|kl\rangle$ . Inserting a completeness relation in terms of a sum over all configurations labeled by  $k'l'$ , the QRPA matrix equation finally reads

$$\begin{pmatrix} A_{kl,k'l'} & B_{kl,k'l'} \\ -B_{kl,k'l'}^* & -A_{kl,k'l'}^* \end{pmatrix} \begin{pmatrix} X_{k'l'} \\ Y_{k'l'} \end{pmatrix} = E \begin{pmatrix} X_{kl} \\ Y_{kl} \end{pmatrix}. \quad (51)$$

$A$  and  $B$  contain matrix elements of the HFB or HF-BCS Hamiltonian. In the simplest case in which pairing is treated in the BCS approximation, the explicit expressions for the QRPA matrices read

$$\begin{aligned} A_{kl,k'l'} &= (E_k + E_l) \delta_{kk'} \delta_{ll'} + \\ &\quad + V_{klk'l'} (u_k u_l u_{k'} u_{l'} + v_k v_l v_{k'} v_{l'}) + \\ &\quad + W_{klk'l'} (u_k v_l u_{k'} v_{l'} + v_k u_l v_{k'} u_{l'}), \\ B_{kl,k'l'} &= -V_{klk'l'} (u_k u_l v_{k'} v_{l'} + v_k v_l u_{k'} u_{l'}) + \end{aligned}$$

$$+ W_{klk'l'}(u_k v_l u_{k'} v_{l'} + v_k u_l v_{k'} u_{l'}), \quad (52)$$

where  $V$  and  $W$  denote the matrix elements of the interactions in the  $pp$  and  $ph$  channels, respectively, and  $u$  and  $v$  are the corresponding BCS occupation factors of single-nucleon states.

The solution of the eigenvalue problem of Eq. (51) determines the energies  $E_n$  of the excited vibrational states  $|n\rangle$ , and the corresponding wave functions expressed in terms of the forward and backward amplitudes  $X_{kl}^{(n)}$  and  $Y_{kl}^{(n)}$

$$|n\rangle = \sum_{kl} \left( X_{kl}^{(n)} \alpha_k^\dagger \alpha_l^\dagger + Y_{kl}^{(n)} \alpha_k \alpha_l \right) |0\rangle. \quad (53)$$

If instead of the simpler HF-BCS model, the full HFB framework is used as a basis on which the QRPA is formulated, the matrix equation (51) remains valid, but the matrices  $A$  and  $B$  display a more complicated structure. In place of the simple  $u$  and  $v$  occupation factors which depend on a single index, one finds the Bogoliubov matrices  $U$  and  $V$ . One way to circumvent the technical difficulties of working in the quasiparticle basis is to formulate the QRPA in the canonical single-nucleon basis which diagonalizes the density matrix. The corresponding matrix equations require only the evaluation of matrix elements of the residual  $ph$  and pairing  $pp$  interactions in this basis, multiplied by certain combinations of occupation factors. The fully self-consistent QRPA, formulated in the HFB canonical single-particle basis, was introduced in Ref. [31]. Self-consistency requires the QRPA residual interaction to be derived from the same force or energy functional that determines the HFB solution. This is crucial for the decoupling of spurious states, associated with symmetry breaking by the mean field solution, from the spectrum of physical excitations. The details of the implementation of the fully self-consistent HFB+QRPA framework in the canonical basis, and accurate tests using Skyrme energy density functionals and density-dependent pairing functionals, have recently been reported in Ref. [32].

The principal source of arbitrariness in the matrix representation of QRPA is the truncation of the basis. In realistic applications it is, therefore, necessary to verify the stability of the results with respect to variations of parameters that determine the discretization and basis truncation (the size of the box in coordinate space or the harmonic oscillator parameter, and the upper limit for unperturbed energies of two-quasiparticle configurations).

Vibrational states can be excited by acting on the nucleus with an external operator  $\hat{F}(\mathbf{r})$ . The corresponding strength function is defined as

$$S(\omega) = \sum_n |\langle n | \hat{F} | 0 \rangle|^2 \delta(\hbar\omega - E_n). \quad (54)$$

If the explicit wave function of the state  $|n\rangle$  (Eq. (53)) is inserted in this expression, the strength of each peak can be evaluated in terms of the single-particle matrix elements of the operator  $\hat{F}(\mathbf{r})$ , the coefficients of the BCS or Bogoliubov transformations, and the forward  $X$  and backward  $Y$  amplitudes.

### 2.5. Relativistic QRPA

Relativistic RPA calculations have been performed since the early 1980s, but it is only more recently that non-linear meson self-interaction terms or density-dependent meson-nucleon couplings have been included in the RRPA framework [33, 34, 35]. As in the case of ground-state properties, the inclusion of a medium dependence in the residual interaction is necessary for a quantitative description of collective excited states. Another essential feature of the RRPA is the fully consistent treatment of the Dirac sea of negative energy states. Within the no-sea approximation, in addition to the usual particle-hole pairs, the RRPA configuration space must also include pair-configurations built from positive-energy states occupied in the ground-state solution, and empty negative-energy states in the Dirac sea [36]. Collective excitations in open-shell nuclei can be analyzed with the relativistic quasiparticle random-phase approximation (RQRPA), which in Ref. [37] has been formulated in the canonical single-nucleon basis of the relativistic Hartree-Bogoliubov (RHB) model. An alternative derivation of the RQRPA in the response function formalism, but with pairing correlations treated only in the BCS approximations, has recently been formulated in Ref. [38].

The RQRPA represents the small amplitude limit of the time-dependent relativistic Hartree-Bogoliubov (RHB) framework. The RQRPA matrix equations in the quasiparticle basis are, however, rather complicated and require the evaluation of the matrix elements of the Dirac Hamiltonian in the basis of the Hartree-Bogoliubov spinors  $U_k(\mathbf{r})$  and  $V_k(\mathbf{r})$ . A considerably simpler representation is provided by the canonical single-nucleon basis. Namely, any RHB wave function can be expressed either in the quasiparticle basis as a product of independent quasiparticle states, or in the canonical basis as a highly correlated BCS-state. The canonical basis is specified by the requirement that it diagonalizes the single-nucleon density matrix. The transformation to the canonical basis determines the energies and occupation probabilities of single-nucleon states that correspond to the self-consistent solution for the ground state of a nucleus. Since it diagonalizes the density matrix, the canonical basis is always localized. It describes both the bound states and the positive-energy single-particle continuum.

Taking into account the rotational invariance of the nuclear system, the matrix equations of the RQRPA read [37]:

$$\begin{pmatrix} A^J & B^J \\ B^{*J} & A^{*J} \end{pmatrix} \begin{pmatrix} X^{\nu, JM} \\ Y^{\nu, JM} \end{pmatrix} = \omega_\nu \begin{pmatrix} 1 & 0 \\ 0 & -1 \end{pmatrix} \begin{pmatrix} X^{\nu, JM} \\ Y^{\nu, JM} \end{pmatrix}. \quad (55)$$

For each RQRPA energy  $\omega_\nu$ ,  $X^\nu$  and  $Y^\nu$  denote the corresponding forward and backward two-quasiparticle amplitudes, respectively. The coupled RQRPA matrices in the canonical basis read

$$\begin{aligned} A_{kk' ll'}^J &= H_{kl}^{11(J)} \delta_{k'l'} - H_{k'l}^{11(J)} \delta_{kl'} - H_{k'l'}^{11(J)} \delta_{k'l} + H_{k'l'}^{11(J)} \delta_{kl} \\ &+ \frac{1}{2} (\xi_{kk'}^+ \xi_{ll'}^+ + \xi_{kk'}^- \xi_{ll'}^-) V_{kk' ll'}^J \\ &+ \zeta_{kk' ll'} \tilde{V}_{kl' k'l}^J \end{aligned} \quad (56)$$

$$\begin{aligned}
B_{kk'lw}^J &= \frac{1}{2}(\xi_{kk'}^+ \xi_{lw}^+ - \xi_{kk'}^- \xi_{lw}^-) V_{kk'lw}^J \\
&\quad + \zeta_{kk'lw} (-1)^{j_l - j_{l'} + J} \tilde{V}_{klk'l'}^J .
\end{aligned} \tag{57}$$

$H^{11}$  denotes the one-quasiparticle terms

$$H_{kl}^{11} = (u_k u_l - v_k v_l) h_{kl} - (u_k v_l + v_k u_l) \Delta_{kl} , \tag{58}$$

i.e. the canonical RHB basis does not diagonalize either the Dirac single-nucleon mean-field Hamiltonian  $\hat{h}_D$ , or the pairing field  $\hat{\Delta}$ . The occupation amplitudes  $v_k$  of the canonical states are eigenvalues of the density matrix.  $\tilde{V}$  and  $V$  are the particle-hole and particle-particle residual interactions, respectively. Their matrix elements are multiplied by the pairing factors  $\xi^\pm$  and  $\zeta$ , defined by the occupation amplitudes of the canonical states. The relativistic particle-hole interaction  $\tilde{V}$  is defined by the same effective Lagrangian density as the mean-field Dirac single-nucleon Hamiltonian  $\hat{h}_D$ .  $\tilde{V}$  includes the exchange of the isoscalar scalar  $\sigma$ -meson, the isoscalar vector  $\omega$ -meson, the isovector vector  $\rho$ -meson, and the electromagnetic interaction. The two-body matrix elements include also contributions from the spatial components of the vector fields. The pairing factors read

$$\zeta_{\kappa\kappa'\lambda\lambda'} = \begin{cases} \eta_{\kappa\kappa'}^+ \eta_{\lambda\lambda'}^+ & \text{for } \sigma, \omega^0, \rho^0, A^0; \text{ if } J \text{ is even} \\ & \text{for } \boldsymbol{\omega}, \boldsymbol{\rho}, \mathbf{A}; \text{ if } J \text{ is odd} \\ \eta_{\kappa\kappa'}^- \eta_{\lambda\lambda'}^- & \text{for } \sigma, \omega^0, \rho^0, A^0; \text{ if } J \text{ is odd} \\ & \text{for } \boldsymbol{\omega}, \boldsymbol{\rho}, \mathbf{A}; \text{ if } J \text{ is even} \end{cases} \tag{59}$$

with the  $\eta$ -coefficients defined by

$$\eta_{kk'}^\pm = u_k v_{k'} \pm v_k u_{k'} , \tag{60}$$

and

$$\xi_{kk'}^\pm = u_k u_{k'} \mp v_k v_{k'} . \tag{61}$$

$\sigma, \omega^0, \rho^0$ , and  $A^0$  denote the time-like components, and  $\boldsymbol{\omega}, \boldsymbol{\rho}, \mathbf{A}$  the spatial components of the meson and photon fields, respectively.

The RQRPA configuration space must also include the Dirac sea of negative energy states, i.e. pair-configurations formed from the fully or partially occupied states of positive energy and the empty negative-energy states from the Dirac sea. The inclusion of configurations built from occupied positive-energy states and empty negative-energy states is essential for current conservation and the decoupling of spurious states, as well as for a quantitative comparison with the experimental excitation energies of giant resonances.

The RQRPA model is fully self-consistent: the same interactions, in the particle-hole and particle-particle channels, are used both in the RHB equations that determine the canonical quasiparticle basis, and in the RQRPA equations. The parameters of the effective interactions are completely determined by the RHB calculations of ground-state properties, and no additional adjustment is needed in the RQRPA calculations. This is an essential feature of the RHB+RQRPA approach and it ensures that RQRPA

amplitudes do not contain spurious components associated with the mixing of the nucleon number in the RHB ground state, or with the center-of-mass translational motion.

## 2.6. Multipole Transition Strength and Transition Densities

We conclude this section with a brief overview of the operators associated with nuclear collective excitations, and provide a summary of basic definitions and useful relations.

In the simplest case the number of protons and neutrons does not change when an external perturbation acts on the nucleus. The one-body operator  $F(\mathbf{r})$  associated with the external field can then induce, even in a superfluid system, only  $ph$  excitations. Later on we will also consider more general cases, including pairing vibrations and charge-exchange excitations.

The case which is best defined is the electromagnetic excitation of a nucleus with real photons. A detailed discussion of this process can be found in many textbooks, for instance in Refs. [4, 5, 6]. The multipole decomposition of the photon field plane wave leads to terms which contain Bessel functions  $j_J(kr)$ , where  $k$  is the photon momentum. In the cases of interest here the photon energy is of the order of MeV, and  $r$  can be the size of the nuclear radius, so that  $kr \approx 10^{-2}$  and the Bessel function is approximated by  $\frac{(kr)^J}{(2J+1)!!}$ . In this approximation the dominant part of the matrix element which corresponds to the electric multipole  $J$ , is proportional to

$$\int \rho(\mathbf{r}) r^J Y_{JM}(\hat{r}) d\mathbf{r} \quad (62)$$

where  $\rho$  is the charge density. The transition amplitude is therefore the matrix element of the operator

$$\hat{F}_{JM}(\mathbf{r}) = \sum_{i=1}^Z e r_i^J Y_{JM}(\hat{r}_i) \quad (63)$$

between the initial and the final state (the sum is over protons). For states with good angular momentum, the response to the electric multipole transition operator is described by the reduced transition probability

$$B(EJ, J_i \rightarrow J_f) = \frac{1}{2J_i + 1} |\langle f || \hat{F}_J || i \rangle|^2. \quad (64)$$

This relation is, of course, also valid for magnetic multipole transition operators.

In many cases studies of excited states with electromagnetic probes are not possible, either because forbidden by selection rules, like for example the isoscalar monopole resonance which has zero angular momentum and therefore cannot be excited by photons, or because strongly hindered by nuclear excitations. Transitions induced by the strong interaction are typically studied by means of hadron inelastic scattering. In analogy with the electromagnetic case, the strong field is described by a plane wave

and, in the limit of small momentum transfer, the nuclear multipole transition operator reads

$$\hat{F}_{JM}(\mathbf{r}) = \sum_{i=1}^A r_i^J Y_{JM}(\hat{r}_i) \quad (65)$$

when neutrons and protons are excited in phase (isoscalar excitation), or

$$\hat{F}_{JM}(\mathbf{r}) = \sum_{i=1}^A r_i^J Y_{JM}(\hat{r}_i) \tau_z(i), \quad (66)$$

when neutrons and protons are excited with opposite phases (isovector excitations), and where  $\tau_z(i)$  is the third component of the isospin operator.

There is no compelling theoretical justification for the choice of the “effective” nuclear operators of Eqs. (65) and (66). In those cases when the transferred momentum is not small, excitations of “overtone” induced by the component of the operator proportional to  $r_i^{J+2}$  are also observed. Nevertheless, it has been shown that properties of nuclear giant resonances can be consistently described with the excitation operators Eqs. (65) and (66) [5, 6]. Concerning the isospin degree of freedom, some nuclear reactions are selective and either isoscalar or isovector states are excited. This is the case, for instance, in  $(\alpha, \alpha')$  inelastic scattering which predominantly excites isoscalar states. In other cases, like  $(p, p')$  inelastic scattering, the reaction itself is not isospin selective but, if the target is a light nucleus with good isospin quantum number, then isoscalar and isovector excitations can be separated. In those nuclei where isospin is no longer a good quantum number, e.g. light neutron-rich nuclei far from stability, nuclear excitations will correspond to a mixture of isoscalar and isovector modes.

When excitations include the spin degree of freedom, the corresponding isoscalar and isovector multipole operators read

$$\hat{F}_{JM}(\mathbf{r}) = \sum_{i=1}^A r_i^L [Y_L(\hat{r}_i) \otimes \vec{\sigma}(i)]_{JM} , \quad (67)$$

and

$$\hat{F}_{JM}(\mathbf{r}) = \sum_{i=1}^A r_i^L [Y_L(\hat{r}_i) \otimes \vec{\sigma}(i)]_{JM} \tau_z(i) , \quad (68)$$

respectively, with  $J = L, L \pm 1$ .

The strength function  $S(\omega)$  associated with the transition operator  $\hat{F}$  is defined by Eq.(54). It is often useful to consider moments of the strength function:

$$m_k(\hat{F}) = \int (\hbar\omega)^k S(\omega) d(\hbar\omega) = \sum_n E_n^k |\langle n | \hat{F} | 0 \rangle|^2 \delta(\hbar\omega - E_n). \quad (69)$$

The first moment, or the energy-weighted sum rule (EWSR), is very important because its value equals the ground-state expectation value of the double commutator  $[\hat{F}, [\hat{H}, \hat{F}]]$ , and therefore it can be evaluated without actually calculating the strength function. This is the well known Thouless theorem, and its non-trivial extension to the HFB-QRPA case has been proven in Ref. [29]. The ratio  $m_1/m_0$  is the quantity often compared

with the experimental excitation energy of the corresponding resonance although, of course, this is only correct if there are no multiple peaks within the energy interval over which the integration in Eq. (69) is performed. One often finds the notation  $E_0$  ( $E_{-1}$ ) for  $m_1/m_0$  ( $\sqrt{m_1/m_{-1}}$ ).

When  $\hat{F}$  represents the isovector electric dipole operator, and the residual interaction does not include velocity-dependent or exchange terms, a very simple result is obtained for the EWSR:

$$m_1 = \frac{2\pi^2 e^2 \hbar NZ}{mc A} \simeq 60 \frac{NZ}{A} \text{ MeV} \cdot \text{mb}. \quad (70)$$

This is the well known Thomas-Reiche-Kuhn (TRK) sum rule, which only includes the numbers of neutrons and protons, and is therefore completely model independent. For Skyrme and Gogny forces, which exhibit velocity-dependent and exchange terms, respectively, the value of  $m_1$  in the above expression is multiplied by  $(1 + \kappa)$ , where  $\kappa$  is typically  $\approx 0.2-0.3$ . In the general case of a spin-independent isoscalar operator of multipole  $L$ , one can derive the following result:

$$m_1 = \frac{\hbar^2}{2m} \frac{L(L+1)^2}{4\pi} A \langle r^{(2L-2)} \rangle, \quad (71)$$

where  $\langle r^{(2L-2)} \rangle$  denotes the ground-state expectation value.

Essential information on the dynamics of a nuclear collective mode is contained in the transition density. For the state  $|\nu\rangle$  this quantity is defined as the matrix element of the density operator:

$$\delta\rho_J^\nu(\mathbf{r}) = \langle \nu | \sum_i \delta(\mathbf{r} - \mathbf{r}_i) | 0 \rangle, \quad (72)$$

where  $|0\rangle$  denotes the ground state. The proton (neutron) transition density includes summation over protons (neutrons) in Eq. (72), and the isoscalar ( $T = 0$ ) and isovector ( $T = 1$ ) transition densities are defined by:

$$\delta\rho_J^{T,\nu} = \delta\rho_J^{n,\nu} + (-1)^T \delta\rho_J^{p,\nu}. \quad (73)$$

Assuming spherical symmetry, the transition density reads

$$\delta\rho_J^{n(p),\nu}(\mathbf{r}) = \delta\rho_J^{n(p),\nu}(r) Y_{JM}^*(\hat{r}), \quad (74)$$

where the radial factor can be expressed in terms of the forward ( $X$ ) and backward ( $Y$ ) QRPA amplitudes, and the single-nucleon radial wave functions multiplied by the corresponding occupation factors:

$$\delta\rho_J^{n(p),\nu}(\mathbf{r}) = \sum_{kl \in n(p)} (X_{kl}^\nu + Y_{kl}^\nu) (u_k v_l + v_k u_l) \langle k || Y_J || l \rangle R_k(r) R_l(r). \quad (75)$$

### 3. Beyond the Mean-Field Approximation

#### 3.1. Extensions of the (Q)RPA

The mean field theories which have been discussed in the previous Section, cannot provide a complete description of the physical phenomena associated with collective



nuclear excitations. The stationary models based on effective interactions, e.g. the HF or HFB, certainly include a large amount of correlations in their phenomenological parameters, and predict nuclear binding energies with remarkable accuracy. However, these models fail to reproduce the empirical features of single-particle levels around the Fermi surface [39, 40], which is essential for a complete description of collective excitations.

Time-dependent theories, and their small amplitude limit such as the RPA and QRPA, provide an accurate description of the two principal integral characteristics of giant resonances: the total strength  $m_0$  and the energy-weighted sum rule  $m_1$ . Accordingly, the calculated centroid energies  $m_1/m_0$  will not be modified by including additional correlations. On the other hand, the second moment of the strength distribution, which in the case of a single peak is associated with its full width at half-maximum (FWHM), or other details of the response function, cannot be described at the level of a mean-field theory. (Q)RPA calculations do not reproduce the experimental values of the total width of vibrational states.

At the (Q)RPA level, nuclear collective motion is represented as a coherent superposition of  $1p - 1h$  (or two-quasiparticle) states. The energy and angular momentum of these vibrations can be released to other degrees of freedom, because vibrational states are embedded in a dense background of excited states. When the energy of a vibrational state lies above the particle emission threshold, the state can decay by neutron or proton emission. This damping mechanism is associated with the escape width  $\Gamma^\uparrow$ , which can be taken into account within the framework of continuum-(Q)RPA (see Sec. 2.3). The spreading width  $\Gamma^\downarrow$  arises because the energy and angular momentum of coherent vibrations can be transferred to more complicated nuclear states, of  $2p - 2h$  (and eventually  $3p - 3h \dots np-nh$ ) character. In order to describe  $\Gamma^\downarrow$  a theoretical framework must include the coupling to these complex configurations.

A vast amount of data on widths of giant resonances in stable nuclei has been accumulated. Escape widths are large in light nuclei, but become less important in medium-heavy and heavy systems, where typical values are of the order of 1 MeV or less. On the other hand, spreading widths of several MeV are typical for resonances in heavier nuclei. For an extensive review on this subject the reader is referred to Ref. [39]. Much less is experimentally known about transition strengths of giant resonances in unstable nuclei, however, it has been pointed out that in neutron-rich nuclei far from stability spreading widths could be enhanced with respect to stable nuclei [41].

In the following we will briefly review several models which go beyond the mean-field approximation in the description of collective excitation phenomena. Simple  $1p - 1h$ , or two-quasiparticle states are coupled by the residual interaction to more complicated configurations. A straightforward approach to this problem would be the diagonalization of the effective Hamiltonian in the configuration space which includes at least the  $2p - 2h$ , or four-quasiparticle states. This avenue, however, is usually not feasible because the number of  $2p - 2h$  configurations can become very large ( $\approx 10^2$  or  $10^3$  per MeV). The second RPA (SRPA) is based on non-interacting  $2p - 2h$  configurations and, in

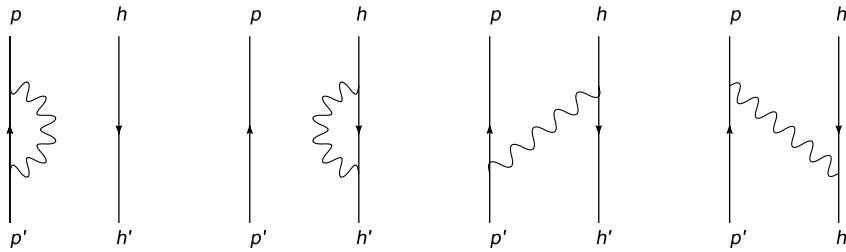


**Figure 2.** Diagrams which correspond to the coupling of the  $p - h$  components of a giant resonance with phonon states.

addition to interaction terms acting in the  $1p - 1h$  space, only interactions between  $2p - 2h$  and  $1p - 1h$  configurations are explicitly taken into account. The SRPA retains basic properties of the RPA, e.g. the conservation of the EWSR [42]. Practical implementations of this framework have been restricted to relatively light nuclei, and only with radical truncations of the configuration space (for a detailed discussion, cf. [43] and references therein). In addition, the current SRPA models are not self-consistent, e.g. in Ref. [43] the Woods-Saxon potential is used to determine the single-particle energies and wave functions, whereas the RPA residual interaction and terms that mix complex configurations are derived from a G-matrix. A more complete SRPA description of collective excitations necessitates a fully self-consistent implementation of the effective interaction, both in the ground-state and in the construction of the SRPA matrix, and also the inclusion of contributions from complex configurations that have been omitted in the current versions of the SRPA.

Another theoretical framework which takes into account the spreading width is based on the concept of particle-vibration coupling. Since the nucleus is a highly correlated system, a nucleon which propagates in the nuclear medium can excite the whole nucleus. The low-lying nuclear excitations correspond predominantly to surface vibrations, and theories which are based on particle-vibration coupling take into account the fact that the nucleons are confined inside the nucleus because of the surface, but at the same time they strongly couple to the dynamical fluctuations of the surface.

The particle-vibration coupling concept lies at the basis of Nuclear Field Theory (NFT) [44]. At the lowest order of NFT the nucleons and the collective vibrations are taken as independent degrees of freedom, and nuclear dynamics is determined from the hierarchy of their couplings. These couplings are described by a (non-relativistic) field theory. Diagrams which correct for the violation of the Pauli principle and appear in lowest order, because vibrations are microscopically built from  $p - h$  pairs, are also included. In the NFT framework the natural extension of the RPA is a model in which the  $1p - 1h$  configurations are coupled with states composed of  $1p - 1h$  pair plus a phonon (instead of  $2p - 2h$  states). This coupling is expressed by the sum of the four diagrams depicted in Fig. 2.

The more recent Extended Theory of Finite Fermion Systems (ETFFS) [45, 46] takes into account  $1p - 1h$ , complex  $1p - 1h \otimes$  phonon configurations, the single-particle

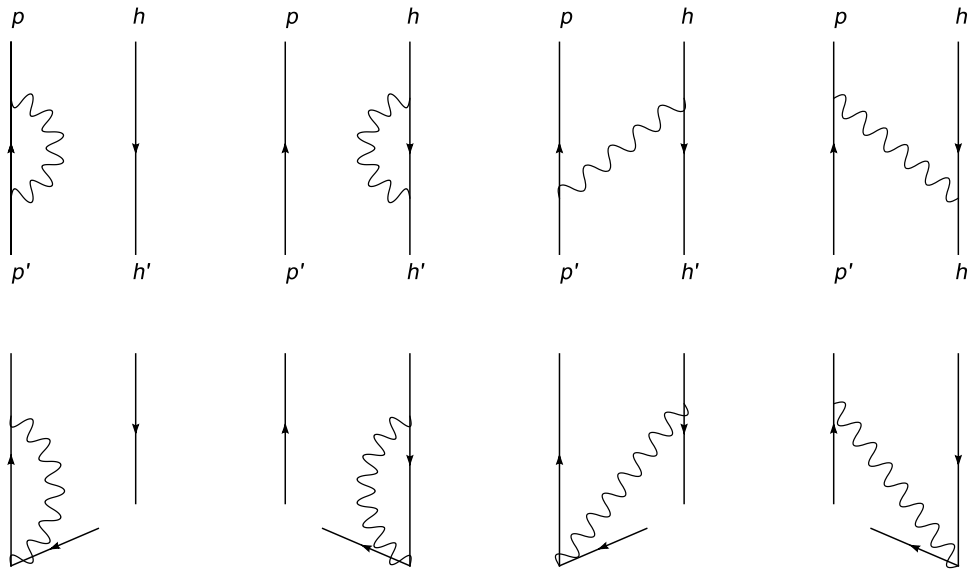


**Figure 3.** Diagrams included in the model of Ref. [45]. The upper row contains the same diagrams as Fig. 2, whereas the lower row displays the “ground-state correlations” diagrams.

continuum and ground-state correlations. The starting point is the exact Bethe-Salpeter equation for the  $p - h$  Green’s function, which is approximated in such a way that it basically corresponds to the RPA solution, plus the contribution of the coupling of  $1p - 1h$  configurations with phonon configurations. These couplings are depicted by the diagrams in Fig. 3. The ETFFS approach includes diagrams associated with the presence of  $1p - 1h$  plus phonon components in the ground-state (bottom row of Fig. 3), i.e. “ground-state correlations”.

Another theoretical framework based on the idea that the interaction between nucleons and phonons determines nuclear dynamics, is the Quasiparticle-Phonon Model (QPM) [47, 48]. Within the QPM the excited states of even-even nuclei are treated as phonons built from two-quasiparticle pairs, i.e. they correspond to solutions of QRPA equations. The ground state is considered as a phonon vacuum and the QRPA yields several collective phonons of each multipolarity, as well as many non-collective (or almost pure two-quasiparticle) solutions; for simplicity all these solutions are referred to as phonons. The main advantage of the QPM approach is that it accounts for the coupling between simple (one-phonon) and complex (two- or three-phonon) configurations, even in cases which are numerically very demanding. The wave function of the excited states represents a combination of one-, two- and three-phonon configurations, with the one-phonon configurations corresponding to the set of all QRPA solutions (of given multipolarity  $J^\pi$ ). The two- and three-phonon configurations are composed of the phonons of different multiplicities coupled to the given  $J^\pi$ . The model Hamiltonian is diagonalized in this basis, and the result are the eigenvalues and the microscopic structure of each excited state (i.e., the amplitudes of one-, two- and three-phonon configurations in the wave function). The NFT and QPM produce similar results. In

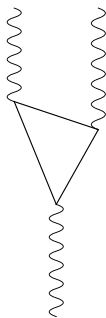


**Figure 4.** Basic diagram which gives rise to the spreading width of one-phonon states in the QPM.

the QPM the basic process which gives rise to the spreading width of giant resonances, is the coupling of one- and two-phonon configurations. The leading diagram is depicted in Fig. 4. It has been shown that the largest contributions come from configurations in which one of the two phonons in the intermediate state is non-collective. In this case the equivalence with the NFT diagrams in Fig. 3 can be demonstrated [39]. The model Hamiltonian contains terms which correspond to the mean-field for protons and neutrons (with some simplified form of pairing in the case of open-shell nuclei), plus a residual effective nucleon-nucleon interaction. In most applications the mean-field is a phenomenological Woods-Saxon potential  $U$ , and the residual nucleon-nucleon interaction has a separable form. A separable interaction is characterized either by a form factor  $r^L$ , or by the Bohr-Mottelson form factor  $\frac{\partial U}{\partial r}$ , and is used both in the (Q)RPA and as the particle-vibration coupling interaction:

$$H_{\text{PVC}} \equiv \sum_{k,k';n,LM} \frac{\beta_{nL}}{\sqrt{2L+1}} \langle k | R_0 \frac{\partial U}{\partial r} Y_{LM}^* | k' \rangle \left[ \Gamma_{nLM}^\dagger + (-)^{L+M} \Gamma_{nL-M} \right] c_k^\dagger c_{k'}, \quad (76)$$

where  $k$  and  $k'$  ( $n$ ,  $\lambda$  and  $\mu$ ) label single-nucleon states (phonons).  $R_0$  is the nuclear radius, and  $\beta_{nL}$  is proportional to the square root of the reduced transition probability Eq. (64), i.e. it is a measure of the collectivity of the phonon state.

The time-dependent density-matrix (TDDM) model [49] is an extension of the time-dependent Hartree-Fock theory beyond the mean-field level. The model describes the time evolution of one-body and two-body density matrices and, therefore, includes the effects of both a mean-field potential and two-body correlations. TDDM has originally been formulated to describe large-amplitude collective motion, but it has also been applied in studies of small-amplitude oscillations, in particular low-energy excitations in unstable oxygen isotopes [50].

Concluding, we emphasize that the basic advantage of mean-field models lies in the fact that they can be formulated in a fully self-consistent way, and easily applied to nuclei all over the periodic table. They reproduce global properties of nuclear collective excitations, but fail to describe specific phenomena in which particular orbitals around the Fermi surface play a special role, or when the inclusion of damping mechanism becomes essential. The models that we have described above extend the physical

picture beyond the mean-field approximation. They can be considered microscopic in the sense that they are based on rigorous formal schemes but, on the other hand, in most applications the particle-vibration coupling vertex is phenomenological.

### 3.2. Illustrative calculations

There are, of course, many applications of the NFT theory [51]. We would like to mention, in particular, a recent study of the effective pairing interaction which arises from the exchange of vibrations between nucleons close to the Fermi surface [52]. Here we review another NFT-based approach to nuclear collective excitations, which uses Skyrme effective interactions [53]. Starting from the self-consistent Skyrme HF-RPA, this model includes the couplings associated with the diagrams shown in Fig. 2. Both the phonons in the intermediate states, and the particle-vibration couplings are consistently calculated using the same Skyrme force.

In the original formulation of the model, which does not include pairing correlations, the coupling with the one-particle continuum is considered. In this way both the escape and the spreading width of the vibrations are taken into account. In some cases [54] it has been possible to describe the particle decay of giant resonances (i.e. partial escape widths to definite hole channels in the residual  $A - 1$  system). More recently this model has been extended to include pairing, but without considering the coupling to the continuum. As an illustrative example, in Fig. 5 we display the calculated IVGDR strength distribution in  $^{120}\text{Sn}$ , obtained with the Skyrme force SIII. Both the QRPA discrete peaks (vertical bars), and the result obtained with the inclusion of phonon coupling – (Q)RPA-PC, are shown. We notice that the dipole strength is significantly redistributed by the phonon coupling, but the position of the centroid energy  $E_0$  does not change from the QRPA value. The (Q)RPA-PC result is in very good agreement with the experimental photoabsorption cross section for  $^{120}\text{Sn}$ , which is also included in the figure. The most important QRPA-PC additional contributions originate from the coupling to the low-energy density vibrations with  $J^\pi$  equal to  $2^+$ ,  $3^-$ ,  $4^+$  and  $5^-$ . When these phonons are collective, corrections associated with the violation of the Pauli principle are less important. In addition, the coupling to giant resonances can also be taken into account, but this gives minor contributions. The reason can be understood from the diagrams shown in Fig. 2: the coupling to low-energy phonons is associated with smaller energy denominators.

In the QPM [48] the model Hamiltonian is composed of terms corresponding to the mean-fields for protons and neutrons, a monopole pairing, and a residual nucleon-nucleon interaction. The mean field is a phenomenological Woods-Saxon potential  $U$ . The residual nucleon-nucleon interaction is separable, and can be characterized either by a form factor  $r^\lambda$ , or by a Bohr-Mottelson form factor. The strength parameters of the residual interaction are adjusted in each particular nucleus to reproduce the energy position and the  $B(E\lambda)$  value of the low-lying  $2_1^+$  and  $3_1^-$  levels. The spurious  $1^-$  state is excluded from the excitation spectra by adjusting the isoscalar strength of the residual

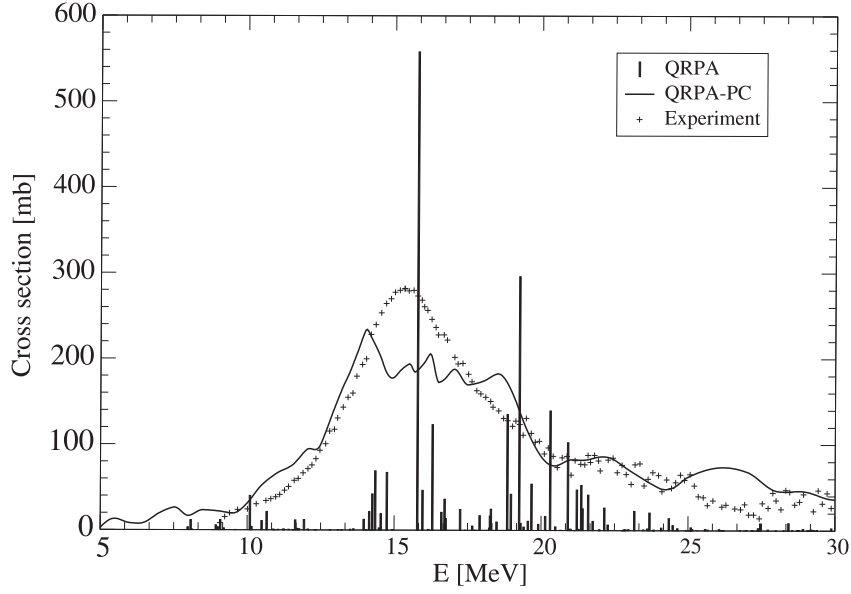


**Figure 5.** Photoabsorption cross section for  $^{120}\text{Sn}$ , calculated with the QRPA (vertical bars) and QRPA-PC (solid curve). The theoretical results are shown in comparison with experimental values.

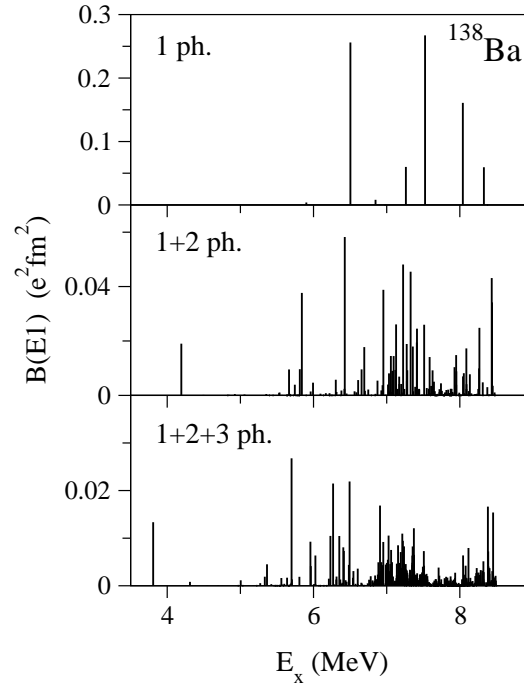


**Figure 6.** Fragmentation of the low-lying electric dipole strength in  $^{138}\text{Ba}$ . Calculations are performed in the one-phonon approximation (top panel), and taking into account the coupling to two-phonon configurations (middle panel), or to two- and three-phonon configurations (bottom panel).

interaction for  $\lambda^\pi = 1^-$ , so that this state has zero energy.

Here we present an example of the fragmentation of one-phonon configurations in

QPM calculations [55]. In Fig. 6 the low-energy portion of the electric dipole transition strength of  $^{138}\text{Ba}$  is plotted for three QPM calculations. In the upper panel the  $B(E1)$  strength distribution corresponds to the one-phonon approximation, and only five QRPA states carry visible  $E1$  strength. When the coupling to two-phonon configurations is included, the  $E1$  strength becomes strongly fragmented, and is distributed over a hundred of states (middle panel). The fragmentation becomes even stronger when three-phonon configurations are included in the wave function (bottom panel). The  $B(E1)$ 's of the strongest  $1^-$  states in the bottom part of Fig. 6, are in quantitative agreement with the experimental values [56]. In the calculation presented in the bottom panel all two- and three-phonon configurations with an energy below 8.5 MeV are included. These configurations include phonons with multipolarity from  $1^\pm$  to  $9^\pm$ , and their total number is about 1200. At higher energies the density of complex configurations increases rapidly, and for a feasible calculation truncation become necessary.

## 4. Low-Energy Electric Dipole Strength

### 4.1. Low-Energy Response of Light Nuclei

Evidence of unusually strong dipole response at low-energy in light nuclei was first reported in fragmentation experiments of halo nuclei on heavy targets with a large number of protons. In the reaction  $^{208}\text{Pb}(^{11}\text{Li}, ^9\text{Li})$  at 800 MeV/nucleon [57] a large Coulomb excitation cross section of 0.9  $b$  was extracted (see also [58]). This cross section is associated with a large peak in the  $B(E1)$  distribution that appears around the two-neutron separation energy, which is of the order of 300 keV. Such a small value of the separation energy could be correlated with the enhancement of the low-lying dipole strength. Namely, the wave functions of the two weakly bound neutrons which form the halo structure are extended far beyond the  $^9\text{Li}$  core. As a result, the excitation of the halo neutrons to the continuum is intensified, and the low-lying dipole response is decoupled from the IV GDR. Initial calculations could reproduce this phenomenon only qualitatively. In Ref. [59] for instance, a simple RPA calculation was performed on top of a Woods-Saxon mean-field potential, whose parameters were adjusted in such a way that the  $p_{1/2}$  neutron state was located at  $-0.2$  MeV. Such an approximation is not satisfactory, of course, because recent experiments have shown that, in addition to the  $(p_{1/2})^2$  orbital, the two halo neutrons outside the  $^9\text{Li}$  core distribute their spectroscopic amplitudes between the  $(s_{1/2})^2$  and  $(d_{5/2})^2$  configurations [60].

The enhancement of the low-lying multipole strength is expected to be a general phenomenon in nuclear systems characterized by small values of particle (e.g. neutrons) separation energies. For a simple spherical potential well, the  $1p-1h$  transition strength can be evaluated analytically, and it has been shown that weakly-bound particles produce a non-resonant concentration of strength just at the threshold energy [61]. The origin of this strength is in the optimal matching of the continuum wave functions with the tail of the wave functions of the outermost weakly-bound orbitals (orbitals are

said to be weakly bound when the corresponding value of  $k \equiv \sqrt{2m|\varepsilon|}/\hbar$ , associated to the single-particle energy  $\varepsilon$ , is much smaller than the inverse of the nuclear radius). Such a simple model could explain the experimentally observed “threshold effect” in the response of one-neutron halo nuclei, like  $^{11}\text{Be}$  [62]. The occurrence of threshold strength is also predicted by more realistic continuum RPA calculations. For instance, RPA transition densities and currents in  $^{11}\text{Be}$  have been studied in Ref. [63]. In Fig. 7 we plot the strength distributions and transition densities for the lowest isoscalar monopole, isovector dipole and isoscalar quadrupole modes. The transition densities differ from the prediction of the macroscopic model, not only because of the long tail associated with the excitations of the weakly-bound neutrons, but also due to the node of the  $2s_{1/2}$  radial function. Macroscopic models, by definition, do not include single-particle shell structures. For  $^{11}\text{Li}$ ,  $^{11}\text{Be}$ , and other light nuclei that we mention below, the term “threshold effect” probably applies much better to the phenomenon under study than “soft mode”. The latter expression is generic, and has also been used for low-lying states in stable nuclei, which absorb only a tiny fraction of the total strength for a given multipole. Even though the occurrence of pronounced threshold strength can be expected also for other multipoles when the separation energies become small, in Ref. [64] it has been pointed out that the contributions of  $L \neq 1$  to the cross section are negligible in experiments with Coulomb excitations on high- $Z$  targets.

An interesting question is whether the response of a two-neutron halo system like  $^{11}\text{Li}$ , is very different from that of a one-neutron halo, e.g.  $^{11}\text{Be}$ . Two-neutron correlations are, of course, essential for the binding of  $^{11}\text{Li}$ , considering that  $^{10}\text{Li}$  is not a bound system. In Ref. [65] the ground state and the dipole response of  $^{11}\text{Li}$  were studied by solving a Hamiltonian that includes a Woods-Saxon potential for the two neutrons outside the structureless  $^9\text{Li}$  core, plus a density-dependent zero-range pairing force. With a careful treatment of the continuum [66], it was shown that in this model the dipole response of the correlated system differs from the free response by 15%-20%. In the description of the dipole response the recoil of the  $^9\text{Li}$  was not taken into account. This term has been shown to play a role, however, in the quantitative description of the ground state of  $^{11}\text{Li}$  [67]. More generally, one expects that not only the recoil, but also the polarization of the  $^9\text{Li}$  core is important for a quantitative description of the dynamical response [68].

Electromagnetic dissociation measurements have been performed for a series of neutron halo nuclei:  $^6\text{He}$  [69],  $^8\text{He}$  [70],  $^{11}\text{Li}$  [71, 72, 73],  $^{12}\text{Be}$  [74],  $^{14}\text{Be}$  [75],  $^{19}\text{C}$  [76], and for the proton halo nucleus  $^8\text{B}$  [77]. Appreciable E1 strength is generally found already at low excitation energy, far below the domain of the GDR. For  $^{11}\text{Li}$ , in particular, the E1 strength observed below 4 MeV excitation energy corresponds to  $\approx 8\%$  of the TRK sum rule, and can be decomposed into at least two broad structures with peak energies at  $\approx 1.0$  MeV and at  $\approx 2.4$  MeV. In a  $(p, p')$  experiment, the corresponding peaks have been observed at 1.3 and 2.9 MeV [78]. A long-standing issue in  $^{11}\text{Li}$  is the description of the low-energy E1 excitations in terms of its halo structure and, particularly, the question of whether the two halo neutrons are subject to strong correlations and eventually form



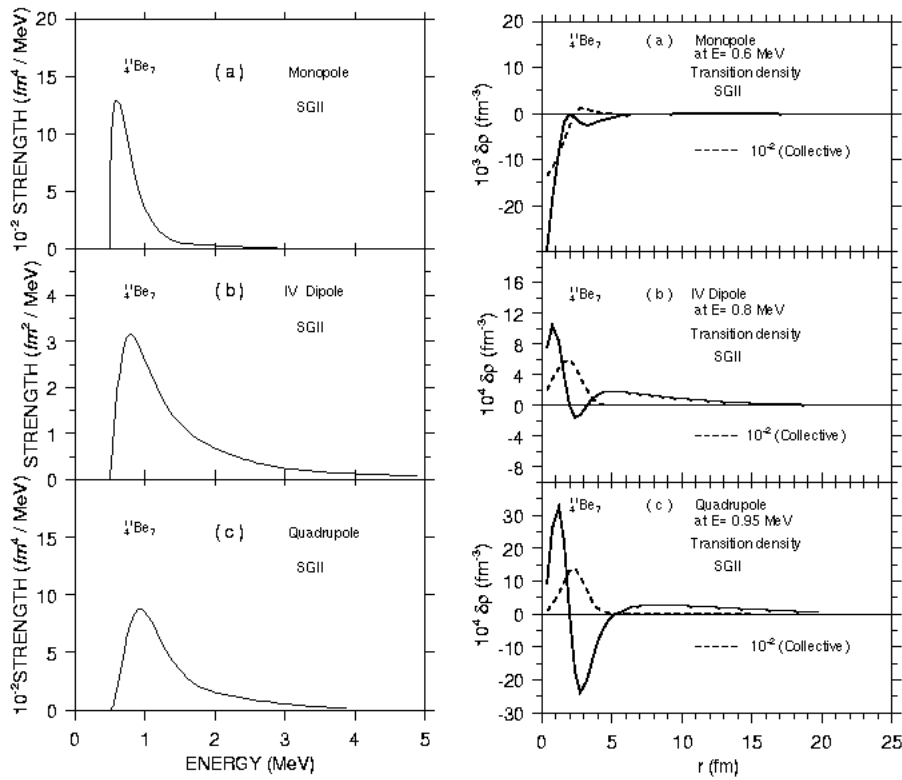


**Figure 7.** Left panel: low-energy isoscalar monopole, isovector dipole and isoscalar quadrupole strength distributions in  $^{11}\text{Be}$ , calculated with the self-consistent continuum RPA [63]. For the peak states the radial transition densities are shown in the panel on the right, and compared with collective transition densities.

a dineutron cluster. While several early experiments [71, 72] did not find evidence for strong correlations between the halo neutrons, a new and significantly improved measurement of the low-lying  $B(E1)$  distribution [73] has revealed a strong low-energy E1 excitation peaked at  $E_x = 0.6$  MeV with  $B(E1) = 4.5(6)$  Weisskopf units, which is the largest low-lying E1 strength ever observed in nuclei, and the  $B(E1)$  distribution could only be reproduced by a three-body model with a pronounced two-neutron correlation.

The structure and excitations of these light systems are best described in a shell-model approach, and calculations have been reported [79] which include model spaces of  $2\hbar\omega$ , or even  $3\hbar\omega$  configurations. Many more transition amplitudes are included than in ordinary mean-field, e.g. RPA calculations, and the coherence between these amplitudes is crucial in enhancing the dipole strength at low energy. In order to obtain realistic results for the  $B(E1)$  values, extended Woods-Saxon single-particle wave functions have to be used in calculations, adjusted in such a way that separation energies reproduce the experimental values. This procedure introduces spurious components that have to be carefully removed from the wave functions.

Let us also mention that the continuum RPA model with Skyrme interactions has been used in studies of the isovector and isoscalar dipole response in  $^{34}\text{Ca}$ ,  $^{28}\text{O}$ ,

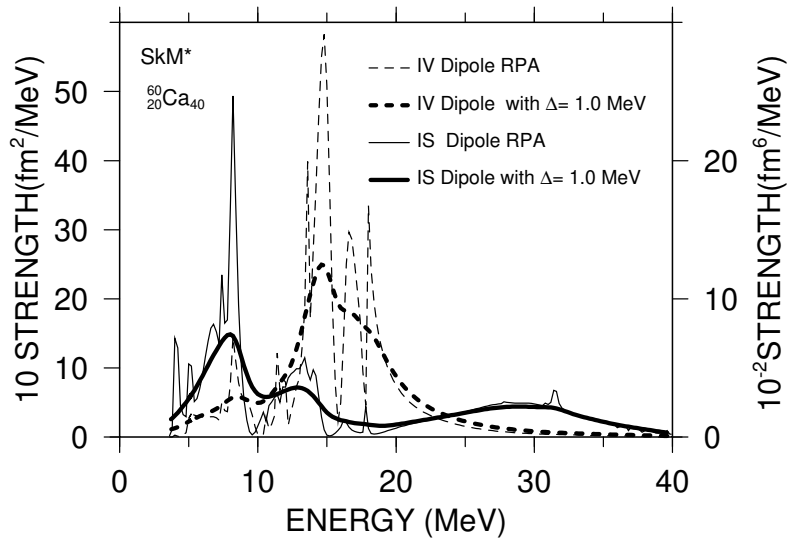


**Figure 8.** Continuum RPA IS and IV dipole strength functions in the nucleus  $^{60}\text{Ca}$ . The scale of the IS dipole strength is shown on the right-hand side, whereas on the left we plot the scale of the IV dipole strength. The thick curves are obtained by averaging the calculated RPA strength with Lorentzian functions of 1 MeV width.

$^{60}\text{Ca}$  and  $^{22}\text{C}$  [80]. These nuclei could be considered as benchmark systems for the dipole response at the nucleon drip-line. It has been shown that the low-lying neutron excitations are characterized by the mixing of isovector and isoscalar modes, and that the threshold strength is predominantly of isoscalar nature. For the nucleus  $^{60}\text{Ca}$  the dipole strength functions calculated with the SkM\* force are shown in Fig. 8. The isoscalar strength found at high excitation energies above the IV GDR can be associated with the dipole compressional mode. Such extremely neutron-rich systems are, of course, not yet accessible in experiments, but the calculation nicely illustrates the features of the dipole response at the limit of neutron binding.

#### 4.2. Low-Energy Dipole Excitations in Oxygen Isotopes

In the oxygen isotopic chain the drip-line nucleus  $^{24}\text{O}$  is located only eight neutrons away from the stable isotope  $^{16}\text{O}$  and, therefore, the evolution of the low-energy dipole strength can in principle be traced up to the neutron drip-line. The possible occurrence of low-lying collective dipole strength in neutron-rich oxygen isotopes has attracted considerable experimental and theoretical interest in recent years.

While in the stable nucleus  $^{16}\text{O}$  earlier experiments [81, 82, 83] did not find any appreciable low-lying dipole strength, more recent electromagnetic excitation experiments (at beam energies around 600 MeV/nucleon) have confirmed the expected occurrence of low-energy dipole strength in the isotopes  $^{18-22}\text{O}$  [84, 85]. Low-energy transition strength has been observed in all neutron-rich oxygen isotopes that were studied, exhausting up to 12% of the TRK sum rule (70) at excitation energies below 15

MeV, i.e., below the region of giant resonances. The low-energy  $E1$  structure in  $^{18}\text{O}$  and  $^{20}\text{O}$  was also studied by intermediate-energy Coulomb excitation at 100 MeV/nucleon, and new low-energy dipole states were found in  $^{20}\text{O}$  [86, 87, 88]. The dynamics of these low-lying dipole excitations, however, has not been resolved in experiments. In particular, it is not clear whether some of these states correspond to a collective soft mode, or they all simply result from incoherent single-particle excitations.

Several modern theoretical approaches have recently been employed in the description of the evolution of low-lying dipole strength in oxygen isotopes. In one of the first studies, large-scale shell-model calculations were performed for neutron-rich oxygen isotopes with up to  $3\hbar\omega$  excitations in the  $0p-1s0d-1p0f$  model space. Pronounced low-lying dipole transition strength below 15 MeV was predicted for  $^{17}\text{O}$ ,  $^{18}\text{O}$ ,  $^{20}\text{O}$  and  $^{22}\text{O}$ , exhausting  $\approx 10\%$  of the TRK sum-rule [89, 90]. The calculated low-lying strength in  $^{17}\text{O}$  and  $^{18}\text{O}$  was found to be consistent with the experimental photoreaction cross sections. The continuum QRPA on top of the coordinate-space HFB [30, 91], with a Woods-Saxon single-particle potential, a Skyrme force as the residual interaction in the  $ph$  channel, and a density-dependent  $\delta$ -force in the pairing channel, has also been employed to analyse the low-energy modes in oxygen isotopes. Pairing is not very strong in these isotopes, in particular the pairing gap is considerably below the empirical  $12/\sqrt{A}$  estimate in  $^{22,24}\text{O}$ . However, since the residual pairing interaction in QRPA generates dynamical correlation effects on the response function through pair density fluctuations, and therefore provides a contribution to the low-lying multipole strength, it is important to include a consistent treatment of pairing correlations within the HFB+QRPA framework. Moreover, the energy weighted sum rules are fulfilled only if the pairing interaction is consistently included both in the solution for the stationary ground state, and in the dynamical linear response [30, 37]. In Ref. [37] the self-consistent RHB+RQRPA has been applied in the study of multipole excitations of neutron-rich oxygen isotopes and, in particular, in the analysis of the evolution of the low-lying isovector dipole strength.

The overall picture emerging from all these calculations is that the onset of dipole strength in the low-energy region is caused by nonresonant independent single-particle excitations of the last bound neutrons. This is similar to the case of light nuclei discussed in the previous subsection. The difference, however, is that for the oxygen isotopes the neutron separation energies are larger, i.e. 3.61 MeV for  $^{24}\text{O}$ , and thus the low-lying strength is much less pronounced than for the threshold effect in light systems.

In order to illustrate the evolution of low-lying dipole strength along the chain of neutron-rich oxygen isotopes, we show the results of the self-consistent RHB+RQRPA calculation [37], based on the density-dependent effective interaction DD-ME2 [28] plus the Gogny D1S force in the pairing channel. The strength distributions associated with the dipole operator Eq. (66) are displayed in Fig. 9. With the increase of the number of neutrons one finds a pronounced fragmentation of the dipole strength, and low-lying strength appears below 15 MeV. The centroid energy of the low-lying  $E1$  states is lowered with the increase of neutron excess, whereas the total strength is enhanced.

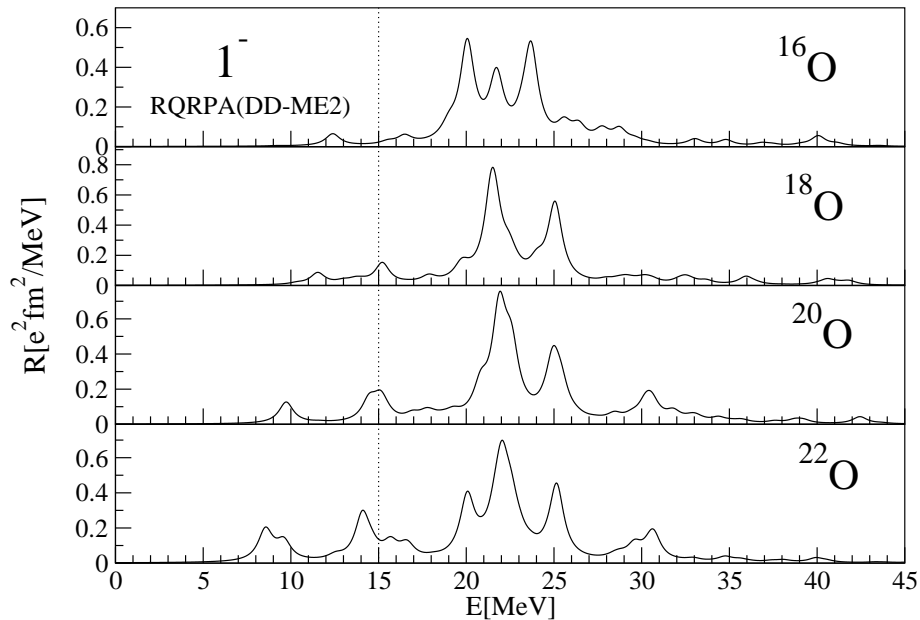


**Figure 9.** Evolution of the isovector dipole strength distribution in oxygen isotopes, calculated within the RHB+RQRPA model using the DD-ME2 effective interaction.

The electric dipole strength distributions in  $^{18}\text{O}$ ,  $^{20}\text{O}$ , and  $^{22}\text{O}$  have also been analyzed in calculations which go beyond the mean-field level by including the coupling of single-quasiparticle states to vibrational modes [92]. By employing the QRPA-PC model with up to four-quasiparticle configurations (two uncorrelated quasiparticles plus a collective phonon), it has been shown that the calculated total photoabsorption cross section below 15 MeV is in very good agreement with experiment. While the simple QRPA analyses predict values which are systematically below the data, the coupling with phonons increases the cross section in the low-energy region. Because of the repulsion between the simple two-quasiparticle states and the complex configurations that include a phonon, the former are shifted to lower energy and this increases the total QRPA strength in the low-energy region. The QRPA-PC photoabsorption cross sections are shown in Fig. 10. We note that the calculation predicts the spreading widths, both for the low-energy dipole strength and for the giant dipole resonance.

The QRPA-PC analysis of Ref. [92] is self-consistent, in the sense that the only input is the Skyrme force which determines the ground state, and no further adjustment of parameters is necessary in the calculation of the response function. A more phenomenological model which also emphasizes the role of phonon coupling is the quasiparticle representation of the phonon damping model [93]. In Ref. [50] the time-dependent density-matrix (TDDM) model, which is an extension of the time-dependent Hartree-Fock theory beyond the mean-field level, was used to calculate the isovector

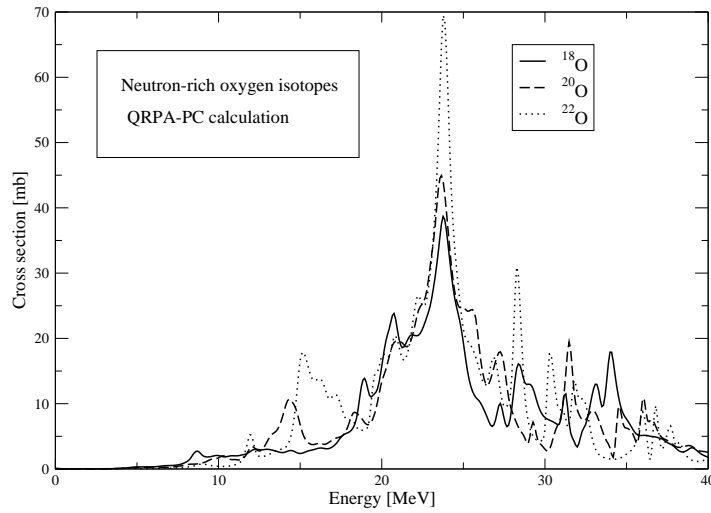


**Figure 10.** Total photoabsorption cross section for the isotopes  $^{18,20,22}\text{O}$ , calculated using the full QRPA plus phonon coupling [92].

dipole strength functions of the even-A isotopes  $^{18-24}\text{O}$ . By adjusting the strength of the residual interaction, the observed isotopic dependence of low-lying dipole strength was reproduced.

In Table 1 the predictions of several models for the low-lying  $E1$  strength in  $^{18-24}\text{O}$  are summarized and compared with data [85, 94]. The sum of the energy-weighted  $E1$  transition strength below 15 MeV is given in units of the classical TRK sum rule. Even though all models agree on the overall effect of the neutron excess on the  $E1$  transition strength, significant differences can be noted in isotopes close to the drip-line. In particular, the inclusion of particle-vibration coupling brings the results in closer agreement with experiment.

A	18	20	22	24
Shell model [90]	0.06	0.11	0.10	0.09
continuum QRPA [91]	0.07	0.11	0.16	0.21
QRPA-PC [92]	0.07	0.09	0.07	
RHB + RQRPA(DD-ME2)	0.04	0.06	0.15	0.18
Exp. [85]	0.08	0.12	0.07	
Exp. [94]	0.11			

**Table 1.** Sum of the energy-weighted dipole strength for  $^{18-24}\text{O}$  up to 15 MeV excitation energy, in units of the TRK sum rule.

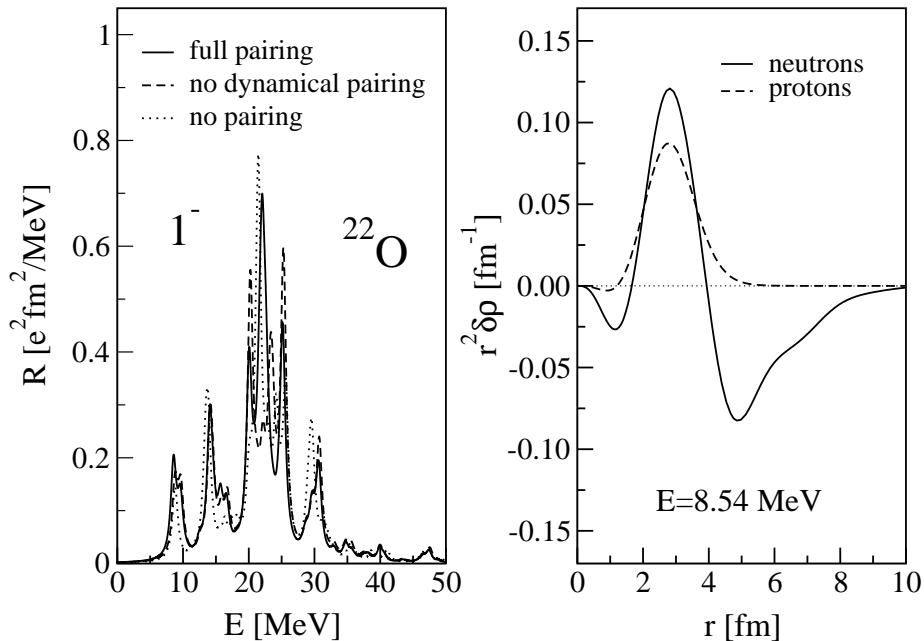


**Figure 11.** The strength function of the IV dipole operator in  $^{22}\text{O}$  (left). The fully self-consistent RHB+RQRPA response (solid line) is compared with the RMF+RRPA calculation without pairing (dotted line), and with the RHB+RRPA calculation which includes pairing correlations only in the ground state (dashed line). The proton and neutron transition densities for the peak at  $E = 8.54 \text{ MeV}$  are shown in the right panel.

The role of dynamical pairing correlations is illustrated in the example of  $^{22}\text{O}$ . The RHB+RQRPA isovector dipole transition strength functions are plotted in the left panel of Fig. 11 for three different calculations: a) the RMF+RRPA calculation without pairing, b) pairing correlations included in the RHB calculation of the ground state, but not in the RQRPA residual interaction (no dynamical pairing), and c) the fully self-consistent RHB+RQRPA calculation. The residual pairing interaction in the RQRPA generates pronounced dynamical correlation effects on the responses through pair density fluctuations. Moreover, the energy-weighted sum rules are only satisfied if the pairing interaction is consistently included both in the static RHB and in the dynamical linear response. Pairing is, of course, particularly important for the low-lying strength. The inclusion of pairing correlations in the full RHB+RQRPA calculation enhances the low-energy dipole strength near the threshold [30, 37].

For the main peak in the low-energy region ( $\approx 8.54 \text{ MeV}$ ), in the right panel of Fig. 11 we display the proton and neutron transition densities. In contrast to the well known radial dependence of the IVGDR transition densities (proton and neutron densities oscillate with opposite phases, the amplitude of the isovector transition density is much larger than that of the isoscalar component), the proton and neutron transition densities for the main low-energy peak are in phase in the nuclear interior, there

is no contribution from the protons in the surface region, the isoscalar transition density dominates over the isovector one in the interior, and the strong neutron transition density displays a long tail in the radial coordinate. However, a detailed analysis of R(Q)RPA amplitudes associated with the low-lying states in oxygen isotopes indicated that they originate mainly from the single-nucleon transitions from the loosely bound neutron orbits [37, 95]. Similar results have been obtained with Skyrme (Q)RPA calculations. For instance, in the study of  $^{28}\text{O}$  performed with the self-consistent Hartree-Fock-Skyrme plus RPA, it was shown that the strength around the threshold originates essentially from uncorrelated excitations of neutrons with small binding energies [80]. Even though in open-shell nuclei the number of partially occupied configurations increases because of the smearing of the Fermi surface, both non-relativistic and relativistic QRPA calculations do not predict the occurrence of pronounced collectivity for the low-lying dipole states in neutron-rich oxygen isotopes.

#### 4.3. Pygmy Dipole Resonances in Heavier Neutron-Rich Nuclei

Medium-heavy and heavy neutron-rich isotopes are characterized by the appearance of a neutron skin, i.e. a layer of excess neutrons on the nuclear surface [96, 97, 98, 99]. When approaching the neutron drip-line, in particular, the large proton – neutron asymmetry leads to a pronounced difference between the corresponding Fermi energies, and neutron orbitals just above the Fermi surface can become unbound. The radial wave functions of very weakly-bound or unbound neutron states are extended far beyond the nuclear surface and this results in the formation of diffuse surface neutron density distributions: skin and halo structures. Experimental evidence for the formation of neutron skin is available from antiproton absorption [100], heavy-ion reaction cross sections [101], and from studies of isovector dipole and spin-dipole resonances [102]. Estimates about the size of the neutron skin can be deduced from experimental radii of charge distributions [103, 104] and mirror displacement energies [105].

The question whether the excess neutrons in the skin can be excited to perform collective oscillations against the rest of the nucleus, or they only contribute to the non-collective threshold strength, has attracted considerable interest in recent years. In the former case one expects that, because the outer neutron orbitals are weakly bound, the resulting dipole mode will be rather soft, i.e. its excitation energy will be far below the giant resonance region. From the theoretical point of view, such a mode also provides a unique test of the isospin-dependent components of effective nuclear interactions, which are particularly pronounced in nuclei with a large proton – neutron asymmetry. Besides being intrinsically interesting as an exotic mode of excitation, the occurrence of low-lying dipole strength plays an important role in predictions of neutron capture rates in the r-process nucleosynthesis, and consequently in the calculated elemental abundance distribution. Namely, although its transition strength is small compared to the total dipole strength, the low-lying collective dipole state located close to the neutron threshold can significantly enhance the radiative neutron capture cross section

on neutron-rich nuclei, as shown in recent large-scale QRPA calculations [106, 107]. This issue will be discussed in more details in Sec. 4.4.

The possible occurrence of a soft dipole mode, or Pygmy Dipole Resonance (PDR) in neutron-rich nuclei, has been analyzed using a variety of theoretical approaches. Early studies of the PDR were based on rather simple hydrodynamical models which involve classical oscillations of the nucleon fluids. These include the three-fluid (protons, neutrons in the same orbitals as protons, and excess neutrons) hydrodynamical model [108], the Steinwedel-Jensen [109] and Goldhaber-Teller models [110]. The low-lying mode has been qualitatively described as a collective oscillation of the neutron enriched surface layer against the core nucleons. It was also suggested, however, that the PDR could arise in nuclear systems with only moderate neutron excess, for instance in Ca isotopes [111].

More recently, microscopic calculations based on Skyrme effective interactions have been employed in studies of the isovector dipole response in neutron-rich nuclei: the Hartree-Fock+RPA [112, 113, 114], the continuum RPA approaches [80, 115, 116, 117, 118, 119], and the self-consistent HFB+QRPA framework formulated in the canonical basis [32, 120]. By employing the continuum RPA, rather large escape widths for direct neutron decay from low-energy dipole states were estimated, implying a pronounced coupling to the continuum [121]. The results of these studies can be summarized as follows: (a) the dipole strength distributions in neutron-rich nuclei are more fragmented than in stable nuclei; (b) the centroids are calculated at significantly lower energies; (c) the ratio of neutron to proton particle-hole amplitudes of low-lying dipole states is much higher than in stable nuclei and, accordingly, the isoscalar (IS) transition densities do not vanish and isoscalar probes can excite these states.

The mixing of isoscalar and isovector states in the low-lying dipole response has been analyzed in several studies [95, 112, 122, 120]. More information about the isospin structure of the PDR can be obtained from a comparison between the RPA dipole strength distribution and the unperturbed response. For  $^{132}\text{Sn}$  this is illustrated in Fig. 12, where we display the discrete dipole spectra for the unperturbed Dirac-Hartree response and the relativistic RPA response. When the residual interaction is turned on, most of the unperturbed strength is pushed towards higher energies, as one expects for isovector states. The pygmy states, however, are shifted below the Dirac-Hartree response. Since the residual interaction is attractive in the isoscalar channel, it appears that the structure of the PDR is predominantly isoscalar. Experimentally the isospin structure of the low-lying E1 states could be, at least in principle, probed by a complementary study of  $(\alpha, \alpha')$  and  $(p, p')$  scattering [123]. Assuming a simplified picture, only isoscalar modes should be excited when the scattered  $\alpha$  particle is detected under extreme forward angles.

RPA calculations with zero-range Skyrme forces have shown that, when the densities of the core nucleons and the excess neutrons are well separated, more like in halo nuclei, oscillations of these densities give rise to pronounced low-energy dipole strength. On the other hand, if the two densities overlap, which is the case in neutron-



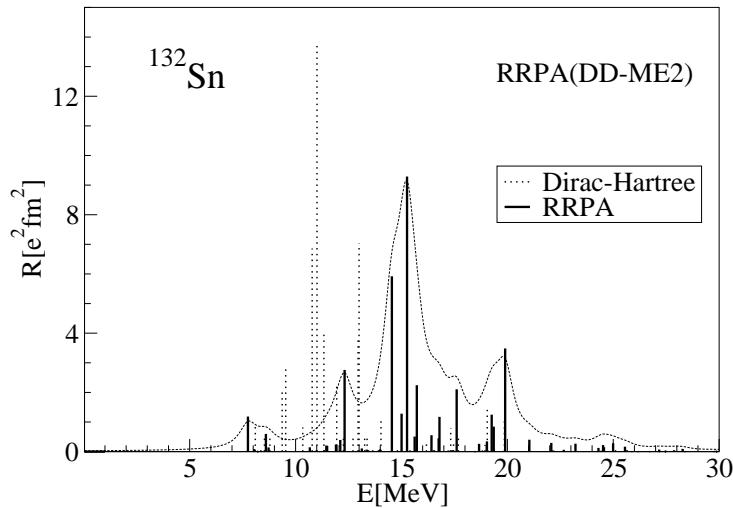


**Figure 12.** The discrete RRPA dipole strength distribution in  $^{132}\text{Sn}$ , in comparison with the unperturbed Dirac-Hartree response.

skin nuclei, then the coupling between the low-lying excitations and the GDR depletes the strength of the former [118]. This result has also been confirmed in studies which have used the self-consistent Hartree-Fock+RPA with the finite-range Gogny interaction [124, 125].

In open-shell neutron-rich nuclei, where pairing correlations play an important role also for low-lying excitations, a fully self-consistent QRPA approach is essential. Two such frameworks have been developed recently: the relativistic QRPA formulated in the canonical basis of the Relativistic Hartree-Bogoliubov model [37], and the HFB+QRPA based on Skyrme energy-density functionals [32, 126, 127]. These models consistently employ for the QRPA residual interactions, both in the  $ph$  and  $pp$  channels, the same effective interactions which determine the nuclear ground state. In this way a direct relation is established between the unique ground-state properties of exotic nuclei and low-lying collective excitations. In addition, the fully self-consistent formulation of QRPA is particularly important for excitations in  $1^-$  channel, because it ensures the separation of spurious center-of-mass motion without introducing additional adjustable parameters. The relativistic (Q)RPA has been employed in several studies of low-lying dipole strength in neutron-rich nuclei. These include the analysis of transition densities and velocity fields associated with the PDR in  $^{208}\text{Pb}$  [128, 129], the evolution of the PDR in exotic isotopes far from the valley of  $\beta$ -stability [95], the study of the effects of pairing correlations on the low-lying E1 strength in exotic nuclei, the isotopic dependence of PDR excitation energies and transition strength distributions [37], and the relationship between the PDR excitation energies and one-neutron separation threshold [130]. An alternative approach to the RQRPA, based on the response function formalism and the

BCS approximation for the description of pairing correlations, has recently been used in studies of low-lying E1 modes in  $^{26,28}\text{Ne}$  [38] and Ni isotopes [131].

The fully self-consistent non-relativistic HFB+QRPA, based on Skyrme density functionals and density-independent delta pairing, has recently been employed in an extensive analysis of strength functions and transition densities in the  $J^\pi = 0^+, 1^-,$  and  $2^+$  channels for the even Ca, Ni and Sn isotopes from the proton to the neutron drip-lines [120]. It has been shown that the low-energy strength increases with neutron number in all multipoles. However, in all channels the correlation between strength and collectivity is found to be much weaker than in stable nuclei.

The spreading width of the low-lying dipole transition strength in neutron-rich nuclei has been evaluated with the phonon damping model [132], the consistent Skyrme Hartree-Fock + QRPA with phonon coupling [92], the quasiparticle phonon model (QPM) [133, 134, 135], and the Extended Theory of Finite Fermion Systems (ETFFS) [46, 136]. These models do not agree on the effects of the coupling to complex configurations on low-lying E1 strength, e.g. for  $^{48}\text{Ca}$  the ETFFS reduces the pygmy strength by 31% with respect to the QRPA result [136], whereas for neutron-rich Sn isotopes the QPM predicts a low-lying dipole strength enhanced by a factor 1.5-2 with respect to the QRPA value [135]. The differences result from different approaches to the coupling with complex phonon configurations. A consistent description of the fine structure of low-lying dipole strength would, of course, necessitate a consistent implementation of a nuclear effective interaction in the calculation of ground state properties, in the (Q)RPA residual interaction, and in the interaction terms which describe the coupling to complex configurations.

On the experimental side, extensive studies of low-lying electric dipole excitations have been performed in recent years. Low-lying E1 states were observed in neutron-capture  $\gamma$ -ray spectra [137, 138], and in resonant scattering of real photons [139]. The latter method, although mainly restricted to nuclei with moderate proton – neutron asymmetry, provides detailed information about the fine structure of dipole transition spectra below the neutron threshold. In particular, pronounced low-energy E1 strength has been observed in  $^{44,48}\text{Ca}$  [136, 140],  $^{56}\text{Fe}$  and  $^{58}\text{Ni}$  [141],  $^{88}\text{Sr}$  [142],  $^{112}\text{Sn}$  [143],  $^{116,124}\text{Sn}$  [144], N=82 isotones [56, 145, 146], and  $^{204,206,207,208}\text{Pb}$  [133, 147, 148, 149]. Recent advances in studies of low-lying dipole modes by photon scattering have been reviewed in Ref. [150]. Radioactive nuclear beams provide new opportunities for studies of low-lying dipole excitations in heavier nuclei with large proton – neutron asymmetry [151]. In a recent experiment of the Coulomb dissociation of secondary Sn beams produced by in-flight fission of a primary  $^{238}\text{U}$  beam, the dipole strength distribution above the one-neutron separation energy was measured in the unstable  $^{130}\text{Sn}$  and the doubly-magic  $^{132}\text{Sn}$  [152]. In addition to the giant dipole resonance (GDR), evidence was reported for a PDR structure at excitation energy around 10 MeV both in  $^{130}\text{Sn}$  and  $^{132}\text{Sn}$ , exhausting a few percent of the E1 energy-weighted sum rule.

Similar to the results obtained with nonrelativistic models, the relativistic QRPA

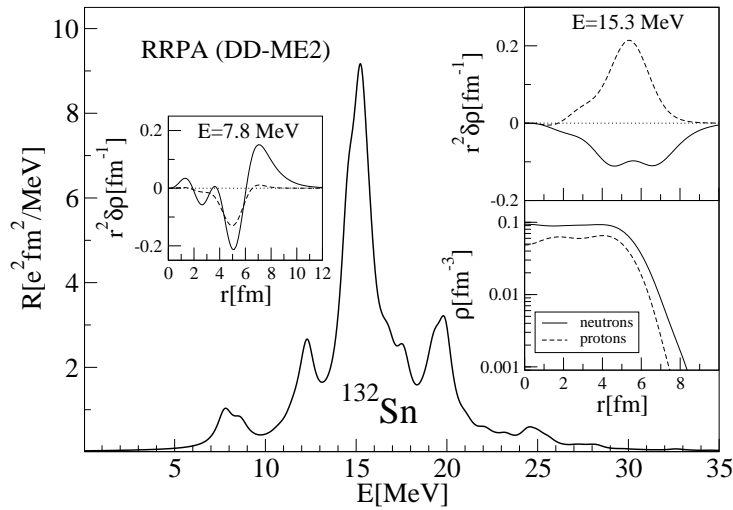


**Figure 13.** The RRPA dipole strength distribution in  $^{132}\text{Sn}$ , calculated with the DD-ME2 effective interaction. In the insertions we plot the ground-state proton and neutron density profiles, and the proton and neutron transition densities for the peaks at 7.8 MeV and 15.3 MeV excitation energy.

dipole response of neutron-rich nuclei is characterized by the fragmentation of the strength distribution and its spreading into the low-energy region. Fully consistent R(Q)RPA calculations have shown that with the increase of the number of neutrons along an isotopic chain, a relatively strong E1 peak appears below 10 MeV. The dynamics of this peak is very different from that of the isovector giant dipole resonance (IV GDR) [37, 95]. This is illustrated in Fig. 13 with the example of  $^{132}\text{Sn}$ , where we plot the RRPA strength distribution which corresponds to the isovector dipole operator, and is calculated with the DD-ME2 effective interaction [28]. In the inserted panels we display the neutron and proton ground-state density distributions, and the neutron and proton transition densities for the low-lying state at 7.8 MeV, and for the IV GDR at 15.3 MeV. For the main peak at 15.3 MeV the transition densities display a radial dependence which is characteristic for the isovector dipole mode (IV GDR): the proton and neutron densities oscillate with opposite phases. The dynamics of the state at 7.8 MeV is completely different: the proton and neutron transition densities are in phase in the bulk of the nucleus, whereas only neutron excitations contribute to the transition density in the surface region. Thus the low-lying pygmy state does not belong to statistical E1 excitations sitting on the tail of the IV GDR, but rather represents a new mode – the PDR: the neutron skin oscillates against the core. The neutron skin, i.e. the difference between the neutron and proton density distributions in the ground state (shown in the right panel in Fig. 13) basically determines the properties of the PDR [134]. Therefore, for a quantitative description of PDR dynamics it is essential to use effective interactions that reproduce available data on the neutron skin. This is

the case, for instance, of the relativistic density-dependent interactions DD-ME1 [27] and DD-ME2 [28], which have been specifically designed to reproduce the differences between the *rms*-radii of neutron and proton density distributions.

In light nuclei the low-energy dipole strength predominantly originates from non-resonant independent single particle excitations of the loosely bound neutrons. However, the structure of the low-lying strength changes with mass. As has been shown in the RRPA analysis of Ref. [95], in heavier nuclei some of the low-lying dipole states display a more distributed structure of the RRPA amplitudes. Among several peaks characterized by single particle transitions, a single collective dipole state is identified below 10 MeV and its RRPA amplitude presents a coherent superposition of many neutron particle-hole configurations. For instance, in the case of  $^{132}\text{Sn}$  (see the dipole strength distribution in Fig. 13) the following neutron *ph* transitions principally contribute to the RRPA amplitude of the state at 7.8 MeV:  $3s_{1/2} \rightarrow 3p_{3/2}$  (51%),  $2d_{3/2} \rightarrow 3p_{3/2}$  (19%),  $2d_{3/2} \rightarrow 3p_{1/2}$  (11%),  $3s_{1/2} \rightarrow 3p_{1/2}$  (7%),  $1h_{11/2} \rightarrow 1i_{13/2}$  (4%),  $1g_{7/2} \rightarrow 1h_{9/2}$  (0.9%),  $2d_{5/2} \rightarrow 3p_{3/2}$  (0.4%),  $2d_{5/2} \rightarrow 2f_{7/2}$  (0.3%),  $2d_{3/2} \rightarrow 4p_{1/2}$  (0.2%),  $1g_{7/2} \rightarrow 2f_{5/2}$  (0.1%), etc. On the other hand, the total contribution from all proton transitions to the state at 7.8 MeV is small:  $\approx 3\%$ , thus the ratio of neutron to proton contribution is much higher than the value  $N/Z$ , typical for the IV GDR state. Such a rich structure of the RRPA amplitude is in contrast to the situation found in light neutron-rich nuclei, where the low-lying dipole peaks below 10 MeV are usually dominated by just one or two neutron *ph* transitions. The level of collectivity can be further enhanced in open-shell nuclei, where because of pairing correlations many additional neutron states become partially occupied and, therefore, many more  $2qp$  transitions contribute to the RRPA amplitude.

A similar analysis of neutron particle-hole components of strong low-energy  $1^-$  excited states in  $^{132}\text{Sn}$  has also been performed in Ref. [120], for the self-consistent HFB+RPA calculation with the Skyrme SkM\* interaction. The distribution of the largest neutron *ph* components and the degree of collectivity for the most pronounced low-energy states is comparable to the results of the relativistic RPA, but the two models differ in the integrated energy-weighted strength in the low-energy region. While relativistic RPA calculations typically predict  $\approx 5\%$  of the classical TRK sum rule in the energy region below 10 MeV, only about 1% is obtained in the calculation with the Skyrme SkM\* interaction. In Ref. [120] it has been suggested that this difference is related to the larger neutron skin typically calculated with relativistic mean-field models, which may be responsible for the more pronounced pygmy resonances. However, this does not seem to be the case for the DD-ME2 relativistic interaction (see Fig. 19), which does not overestimate the empirical values for the neutron skin in Sn isotopes and, at the same time, reproduces the experimental results for the integrated energy-weighted dipole strength in the low-energy region.

The RPA and QRPA analyses of the dynamics of low-lying E1 strength distributions have mostly been performed on the mean-field level, i.e. without taking into account the spreading effects which arise from the coupling of single-nucleon states to the collective low-lying excitations (phonons). The principal effect of the particle-vibration coupling

is an increase of the nucleon effective mass at the Fermi surface, and this is reflected in an increase of the density of single-nucleon states close to the Fermi energy. It has been argued that the inclusion of particle-vibration coupling in (Q)RPA calculations, i.e. extending the (Q)RPA model space to include selected two-quasiparticle  $\otimes$  phonon states, would not only improve the agreement between the calculated and empirical widths of the GDR structures, but it could also have a pronounced effect on the low-lying E1 strength. For instance, the coupling to low-lying phonons could fragment the PDR structure over a wide region of excitation energies. As a result of this fragmentation only an enhancement of the E1 strength would be observed in the low-energy region, rather than a prominent PDR peak. The importance of particle-vibration coupling effects for the multipole response of neutron-rich nuclei has particularly been emphasized in studies that have used the QRPA plus phonon coupling model based on the Hartree-Fock (Q)RPA with Skyrme effective forces [92, 153]. In Ref. [153] the QRPA plus phonon coupling model was applied in the analysis of dipole excitations in  $^{208}\text{Pb}$ ,  $^{120}\text{Sn}$  and  $^{132}\text{Sn}$ . In contrast to the results obtained in the relativistic (Q)RPA framework, the QRPA plus phonon coupling model predicts low-lying E1 strength of non-collective nature in all three nuclei.

In Fig. 14 we display the photoabsorption cross section for  $^{132}\text{Sn}$ , calculated with the fully consistent RPA and RPA-PC models using the Skyrme force SIII. The corresponding RPA-PC transition densities for the GDR state at 13.5 MeV and for the most pronounced low-energy peak at 9.7 MeV are shown in Fig. 15. Even though the transition densities, both for the GDR and for the low-lying peak at 9.7 MeV, are similar to those calculated with the relativistic RPA (see Fig. 13) the analysis of the structure of RPA (RPA-PC) amplitudes shows that none of the peaks below 10 MeV contain contributions of more than two or three different neutron particle-hole ( $ph$ ) configurations. Predominantly these peaks correspond to just a single-neutron transition, and each of them exhausts less than 0.5% of the energy-weighted sum rule.

Low-lying E1 excitations in neutron-rich Sn isotopes have also been studied in the Quasiparticle Phonon Model [134], in a model space that included up to three-phonon configurations built from a basis of QRPA states, and with separable multipole-multipole residual interactions. The single-nucleon spectra were calculated for a Woods-Saxon potential with adjustable parameters. Empirical couplings were used for the QPM residual interactions. In the QPM spectra for  $^{120-132}\text{Sn}$  the low-energy dipole strength was found concentrated in a narrow energy interval such that the PDR could be identified. It was shown that, despite significant multi-phonon contributions to the mean-energy and transition strength, the PDR states basically retain their one-phonon character.

Because of its relatively large neutron excess, the stable nucleus  $^{208}\text{Pb}$  has also been investigated for a possible occurrence of pygmy dipole resonant states. Experimental evidence has been reported in elastic photon [154] and photoneutron scattering [155], and in electron scattering [156]: pronounced E1 strength has been observed in the energy region between 9 and 11 MeV, several MeV below the IV GDR in  $^{208}\text{Pb}$ . On

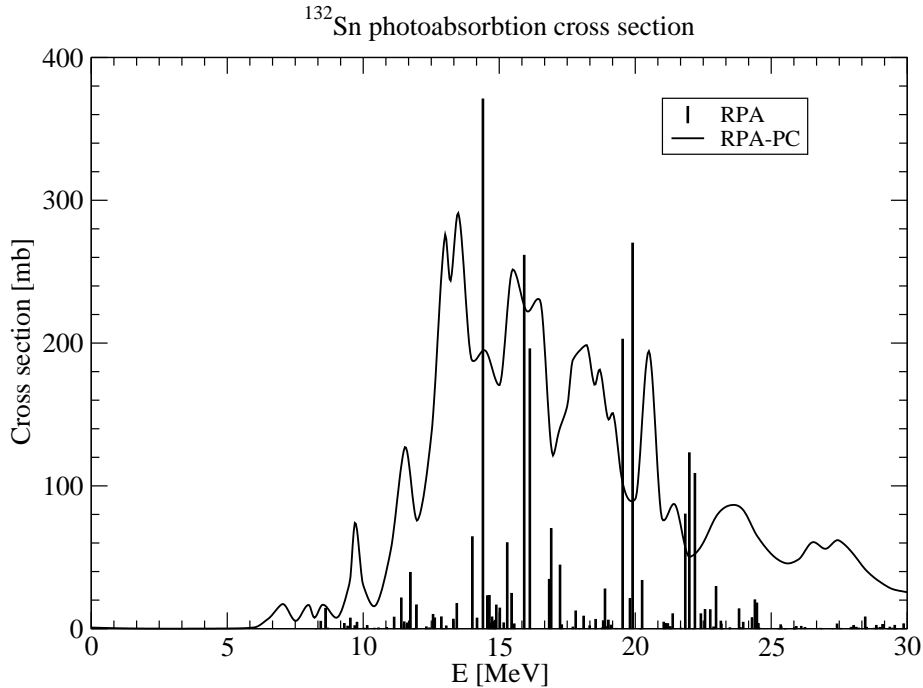


**Figure 14.** Photoabsorption cross section for  $^{132}\text{Sn}$ , calculated with the RPA and RPA-PC models. The effective interaction is Skyrme SIII.

the theoretical side, one of the first microscopic analysis was performed in the Hartree-Fock plus RPA model based on the Skyrme interaction SGII [157]. Two pronounced peaks were calculated at 8.7 MeV and 9.5 MeV, which appeared as likely candidates for the PDR. In a recent self-consistent relativistic RPA study based on the NL3 effective interaction, a pronounced low-energy dipole peak was calculated at 7.29 MeV [128]. The structure of the RRPA amplitude, the corresponding transition densities and velocity fields indicate that this state can be interpreted as a collective PDR mode. The RRPA prediction for the PDR state has been confirmed in a subsequent  $(\gamma, \gamma')$  experiment, which disclosed a resonance-like structure centered at 7.37 MeV, approximately at the neutron emission threshold [133].

In Fig. 16 we display the isovector dipole strength distribution in  $^{208}\text{Pb}$ , evaluated with the self-consistent RRPA model employing the DD-ME2 effective interaction [28]. The calculated energy of the main peak at 13.4 MeV is in excellent agreement with the experimental value of the excitation energy of IV GDR:  $13.3 \pm 0.1$  MeV [158]. The pronounced low-energy peak at 7.2 MeV is close to the experimental centroid of the low-lying dipole strength at 7.37 MeV [133]. In the panels on the right in Fig. 16 we plot the

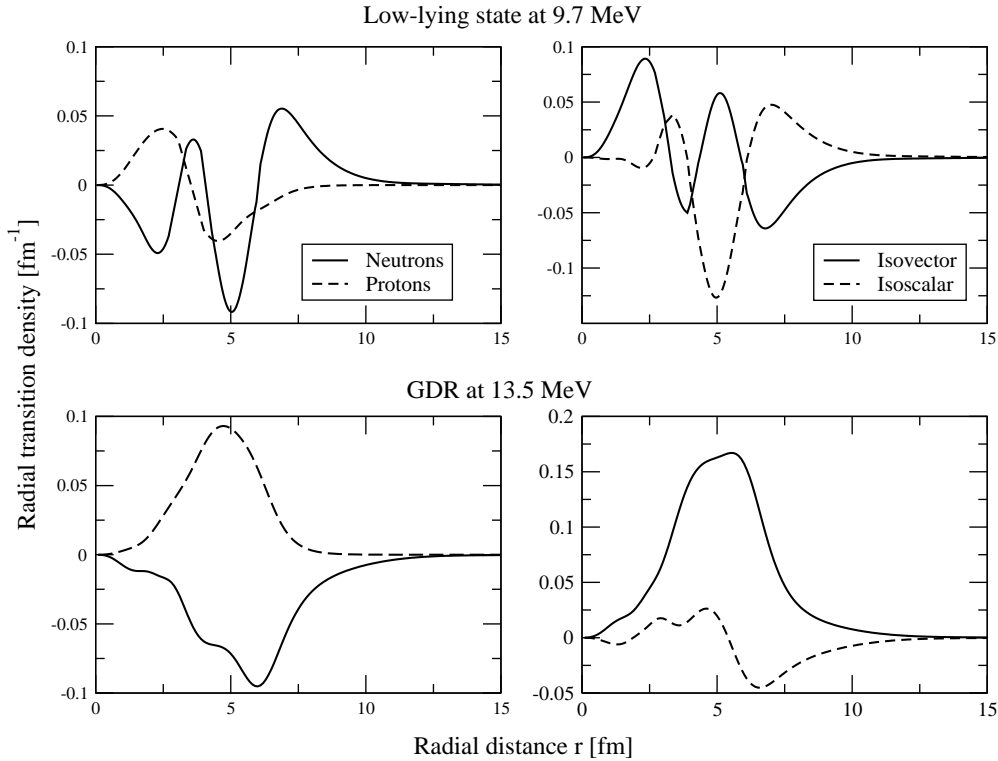


**Figure 15.** RPA-PC transition densities for  $^{132}\text{Sn}$ . In the upper panels the proton and neutron (right panel), and isoscalar and isovector (left panel) transitions densities for the state at 9.7 MeV are shown. For comparison in the lower panels we plot the corresponding transition densities for the IV GDR at 13.5 MeV.

RRPA transition densities for the low-energy state at 7.2 MeV, and the IV GDR state at 13.4 MeV, respectively. Obviously, the dynamics of the low-lying mode is very different from that of the isovector giant resonance: the proton and neutron transition densities are in phase in the nuclear interior and there is large contribution from the neutrons in the surface region. For the IV GDR state the total isovector transition density is much stronger than the isoscalar component. On the other hand, for the state at 7.2 MeV the isoscalar transition density dominates over the isovector one in the interior, and the large neutron component in the surface region contributes to the formation of the node in the isoscalar transition density [95, 112, 122].

Low-lying E1 excitations have also been observed below 10 MeV in  $(\gamma, \gamma')$  scattering on the N=82 isotones:  $^{138}\text{Ba}$ ,  $^{140}\text{Ce}$ ,  $^{142}\text{Nd}$ , and  $^{144}\text{Sm}$  [56, 123]. The subsequent analysis of the RHB+RQRPA transition densities for the calculated low-lying states in these nuclei has shown that a collective PDR mode indeed develops. However, the calculated

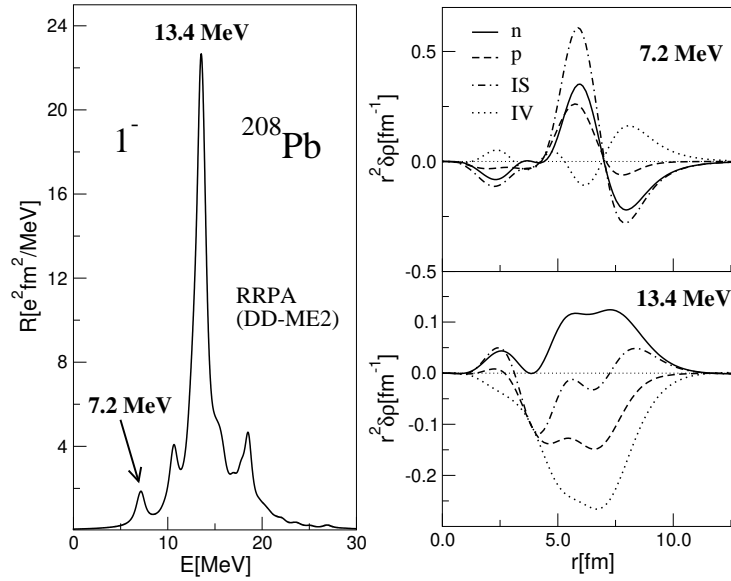


**Figure 16.** The RRPA dipole strength distribution in  $^{208}\text{Pb}$ , calculated with the DD-ME2 effective interaction. The neutron, proton, isoscalar(IS), and isovector(IV) transition densities, for the pygmy state at 7.2 MeV and the IV GDR state at 13.4 MeV are plotted in the panels on the right.

PDR are located  $\approx 1\text{-}2$  MeV above the experimental centroids [37]. The evolution of the isovector dipole strength distribution in  $N=82$  isotones, evaluated in the fully self-consistent RHB+RQRPA with the DD-ME2 effective interaction, is illustrated in Fig. 17. The dotted vertical line separates the low-energy region below 10 MeV from the region of giant resonances. In contrast to the IV GDR, which weakly decreases in excitation energy with the increase of the proton number, i.e. with mass number, the centroids of the low-lying structure increase in energy, whereas the total low-energy strength decreases when the proton – neutron asymmetry is reduced. One notices that the low-lying states are far more sensitive to the variations of the proton number, than the IV GDR structure. These observations are consistent with the interpretation of the low-energy peaks in terms of the PDR, because the reduction of the asymmetry between the neutron and proton density distributions in the ground state should generally result in higher PDR excitation energies and in the suppression of its strength [130]. The RHB+RQRPA  $B(E1)$  strength in the low-energy region below 10 MeV decreases with mass number along the  $N=82$  isotone chain (lower panel in Fig. 17), but the calculated values are systematically above the data [56, 123]. On the other hand, the quasiparticle phonon model (QPM) predicts a constant summed  $E1$  strength in all the measured  $N=82$  nuclei [159]. The reason is that, in contrast to the fully self-consistent RHB+RQRPA approach, the QPM calculations employ the same single-particle spectrum for all the  $N=82$  isotones [160], and therefore cannot describe the details in nuclear structure which



result from the variation of the proton number.

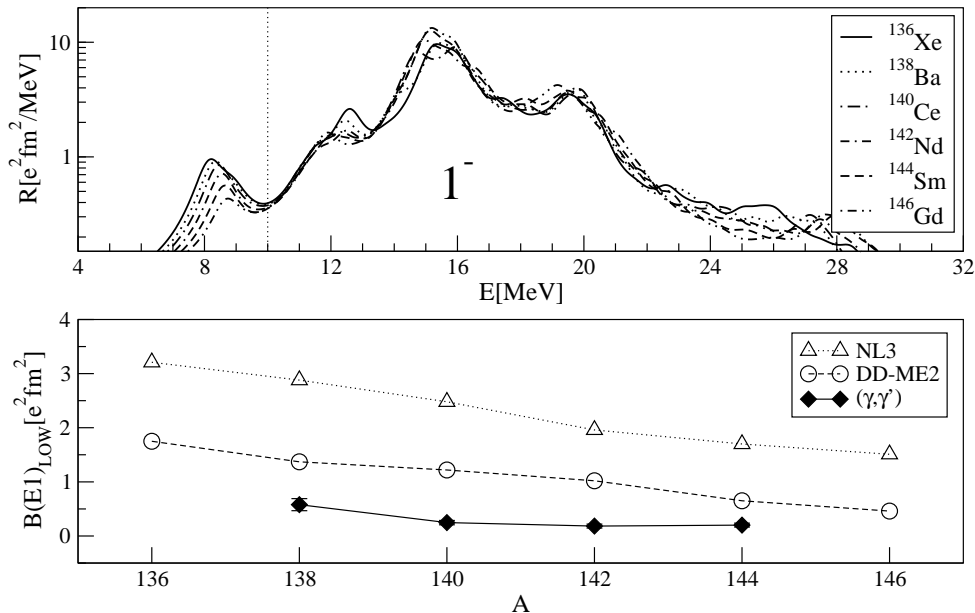


**Figure 17.** The isovector dipole strength distributions in  $N=82$  isotones calculated in the RHB+RQRPA model, with the DD-ME2 effective interaction (upper panel). The integrated  $B(E1)$  transition strength below 10 MeV, for the NL3 and DD-ME2 interactions, is compared with the data from  $(\gamma, \gamma')$  scattering [56, 123] (lower panel).

The theoretical analysis of low-lying excitations and the comparison with data, can be used as a sensitive tool to constrain the isovector channel of effective nuclear interactions. In the lower panel of Fig. 17 we compare the theoretical  $B(E1)$  strength in the low-energy region below 10 MeV with data. The theoretical values have been calculated in the consistent RHB+RQRPA model with the very popular non-linear meson-exchange effective interaction NL3 [24], and with the new meson-exchange interaction DD-ME2 [28], which explicitly includes a medium dependence of the meson-nucleon couplings. Obviously the NL3 interaction, which is known to overestimate the size of the neutron skin not only in exotic neutron-rich nuclei but also in  $^{208}\text{Pb}$ , predicts too much low-lying  $B(E1)$  strength. On the other hand, an interaction like DD-ME2 which has been adjusted to the empirical differences between the radii of neutron and proton density distributions, significantly improves the agreement of the calculated low-energy dipole strength with data. The remaining difference might be caused by the coupling with more complex phonon configurations [135], not taken into account in the RHB+RQRPA models, or in the missing  $E1$  strength in  $(\gamma, \gamma')$  scattering which may be quite considerable when dealing with end-point energies close to the neutron separation threshold [144].

#### 4.4. Isotopic Dependence of Pygmy Dipole Resonances

The evolution of low-lying dipole transition strength along an isotopic chain provides useful information about the underlying dynamics of soft modes in exotic nuclei. In particular, an important question is the location of PDR with respect to the neutron separation threshold [130]. This is important not only for the possible detection of PDR in experiments, but also for modeling the r-process nucleosynthesis [107]. Most of the recent photon scattering experiments provide data on the dipole strength only below the neutron separation energy, i.e. only a portion of the overall low-lying E1 strength is observed [56, 136, 140, 141, 142, 144, 145, 146, 147, 148, 149]. Of course for a more complete understanding of the structure of the low-lying dipole strength and its relation to the PDR mode, data on transition strength above the neutron threshold are necessary [130].

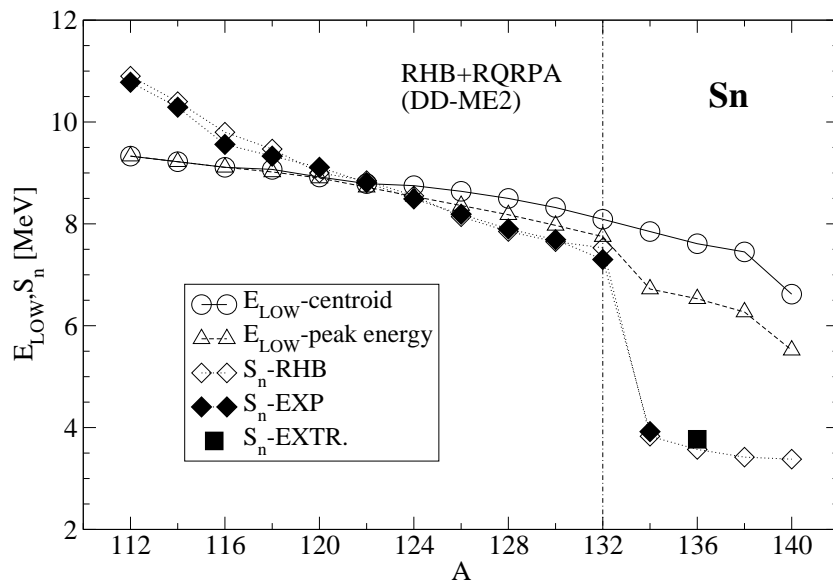


**Figure 18.** The calculated PDR peak and centroid energies, and the one-neutron separation energies for the sequence of Sn isotopes, as functions of the mass number. The DD-ME2 effective interaction has been used in the RHB+RQRPA calculations. The RHB results for the neutron separation energies are compared with the experimental and extrapolated values [161].

This is illustrated in Fig. 18, where we display the RHB+RQRPA results for the peak and centroid energies of the PDR in a series of Sn isotopes. The RQRPA predicts a monotonic decrease of the PDR with mass number, and only a small kink in the peak excitation energies is calculated at the  $N = 82$  shell closure. In the same plot we have also included the calculated one-neutron separation energies, in comparison with the data and the extrapolated value [161]. The self-consistent RHB calculation, with the DD-ME2 mean-field effective interaction in the  $ph$  channel and the D1S Gogny

force in the pairing channel, reproduces in detail the one-neutron separation energies in Sn nuclei. We notice that the separation energies decrease faster than the calculated PDR excitation energies. At the doubly closed-shell nucleus  $^{132}\text{Sn}$  a sharp reduction of the one-neutron separation energy is observed and reproduced by the RHB calculation, whereas the shell closure produces only a much weaker effect on the PDR peak energies. The increased fragmentation of the low-lying strength in heavier Sn isotopes results in larger differences between the PDR peak and centroid energies. The important result here is that for  $A < 122$  the PDR excitation energies are below the corresponding one-neutron separation energies, whereas for  $A \geq 122$  the pygmy resonance is located above the neutron emission threshold. This means, of course, that in the latter case the observation of the PDR in  $(\gamma, \gamma')$  experiments will be strongly hindered [130, 144].

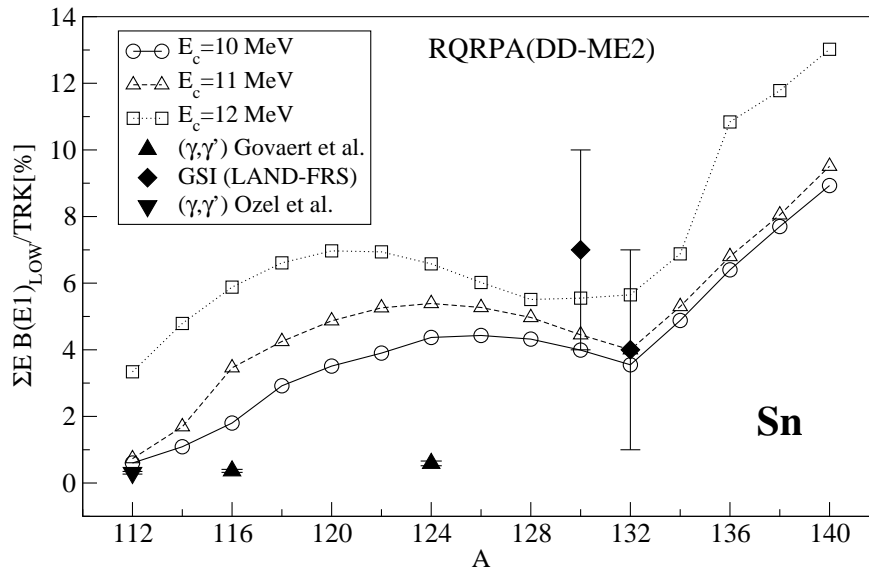


**Figure 19.** The RHB+RQRPA energy-weighted dipole strength, integrated up to the energy cut-off  $E_c=10$ , 11, and 12 MeV, respectively, and plotted in percents of the TRK sum rule. The experimental results are from Refs. [143, 144, 152].

The presently missing data on dipole strength above the neutron threshold could be obtained in the near future by using tagged photons at S-DALINAC [123]. In addition, photon scattering with high intensity beams at energies below and above the neutron separation threshold are planned at the superconducting electron accelerator ELBE [162, 163]. The first studies at ELBE include photon-scattering on  $^{92,98,100}\text{Mo}$  [164]. It is interesting to note that the data show an enhancement of the dipole transition strength around 9 MeV: in  $^{92}\text{Mo}$  the pygmy strength is located below the neutron separation energy, whereas in  $^{100}\text{Mo}$  it shifts above the neutron threshold.

In Fig. 19 we display the isotopic dependence ( $^{112}\text{Sn}$ - $^{140}\text{Sn}$ ) of the energy weighted dipole strength in the low-energy region, integrated up to the cut-off energy  $E_c=10$ ,

11, and 12 MeV, respectively, and plotted in percents of the classical TRK sum rule. Model calculations are performed in the RHB+RQRPA with the DD-ME2 plus Gogny D1S interactions, and the results are compared with the available data from photon scattering [143, 144], and Coulomb dissociation of secondary Sn beams from in-flight fission [152]. The calculated low-lying E1 strength is in excellent agreement with the recent experimental data for  $^{112}\text{Sn}$  [143] and  $^{130,132}\text{Sn}$  [152], whereas it overestimates the  $(\gamma, \gamma')$  data for  $^{116,124}\text{Sn}$  [144]. When considering the evolution of low-lying dipole strength along an isotopic chain, in a first approximation one could expect that the relative strength of the PDR increases monotonically with the number of neutrons, at least within a major shell. In the case of Sn isotopes the RHB+RQRPA calculations predict, however, that the PDR peak is most pronounced around  $^{124}\text{Sn}$  (depending on the cut-off, see Fig. 19) [37]. A combination of shell effects and reduced pairing correlations, leads to a reduction of the strength of the PDR in heavier Sn nuclei below  $N = 82$ . The local minimum in the low-lying E1 strength is calculated for  $^{132}\text{Sn}$ , whereas in the neighboring isotopes the transition strength increases because of enhanced collectivity, i.e. the increase in the number of two-quasiparticle pairs contributing to the RQRPA configuration space. We also notice the pronounced difference in the pygmy strength between nuclei close to the valley of  $\beta$ -stability and exotic nuclei: while below the  $N=82$  shell closure the integrated transition strength is at most  $\approx 4\%$  of the TRK sum rule value (for  $E_c=10$  MeV), beyond  $^{132}\text{Sn}$  the PDR strength exhibits a strong enhancement.

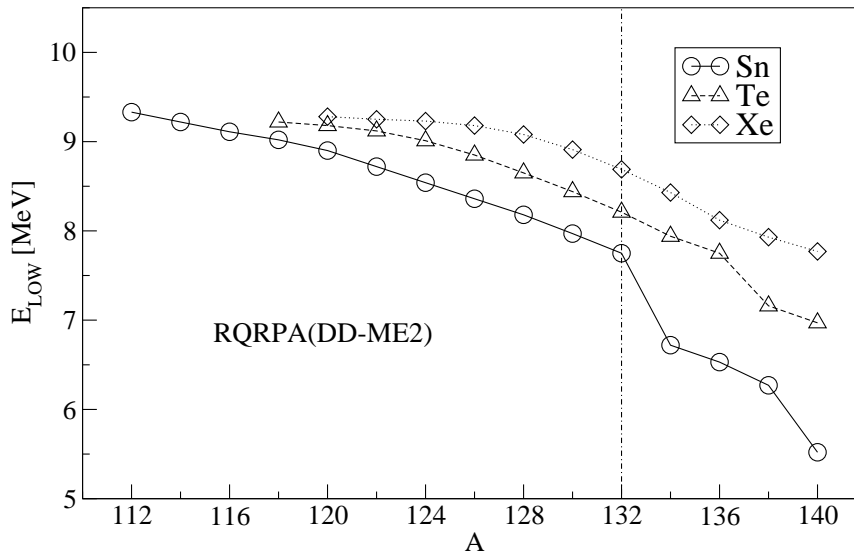


**Figure 20.** The RHB+RQRPA calculated PDR peak energies for Sn, Te, and Xe isotopes.

It is, of course, interesting to explore other isotopic chains of spherical nuclei where

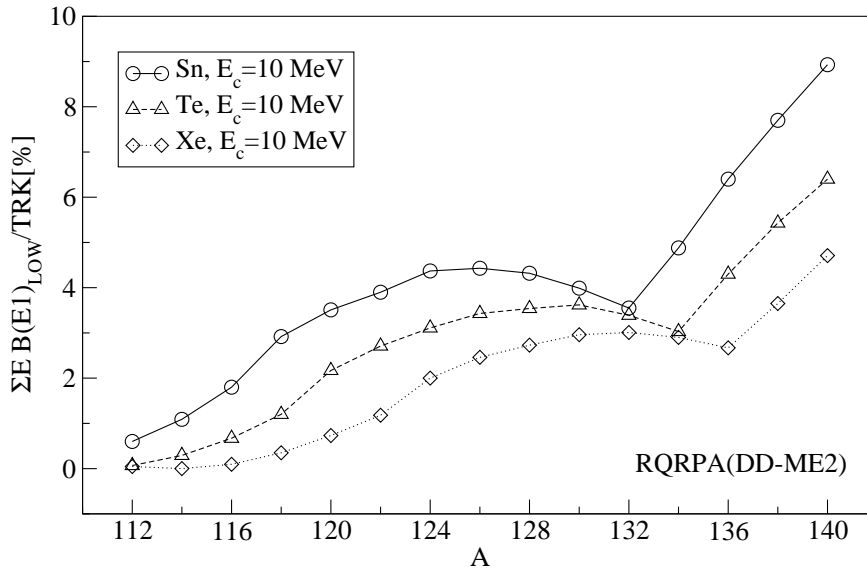


**Figure 21.** Same as Fig. 19, but for the Sn, Te, and Xe isotopes. The cut-off energy for the low-lying E1 strength is set at  $E_c=10$  MeV.

one expects the occurrence of the PDR in the E1 excitation spectrum. In Figs. 20 and 21 we plot the calculated PDR peak energies and the integrated low-lying E1 strength for Sn, Te, and Xe isotopes. The cut-off energy for the low-lying strength is arbitrarily set at  $E_c=10$  MeV. The calculated low-lying dipole strength appears rather sensitive to small variations in the number of nucleons. The PDR excitation energies are lowest in the isotopic chain with the smallest number of protons, i.e. in Sn nuclei. This behavior reflects the nature of the PDR: a larger neutron excess should result in lower PDR excitation energy. In the region beyond  $A=132$ , the slope of the PDR peak energies becomes steeper than for stable nuclei, because the neutrons in outer orbitals are more loosely bound and thus the restoring force in the oscillation of the skin against the core becomes weaker. For Te and Xe isotopes we plot the PDR peak energies starting from  $^{118}\text{Te}$  and  $^{120}\text{Xe}$ , respectively. In the lighter systems the PDR could not be uniquely identified. The energy-weighted dipole transition strength in the region below 10 MeV (Fig. 21) is strongest for the Sn chain, and somewhat weaker for Te and Xe. This is, of course, to be expected because the PDR strength must be proportional to the neutron excess. In all the three chains the local minima in the integrated transition strength are obtained at  $N=82$ , and the PDR strength rapidly increases beyond the neutron shell closure.

Finally, in Fig. 22 the RHB+RQRPA results for the PDR in Ni and Pb isotopes are shown. The RHB neutron separation energies, calculated with the DD-ME2 plus Gogny D1S interactions, are compared with the experimental values [161]. In the sequence of Ni nuclei the crossing between the theoretical curve of one-neutron separation energies and

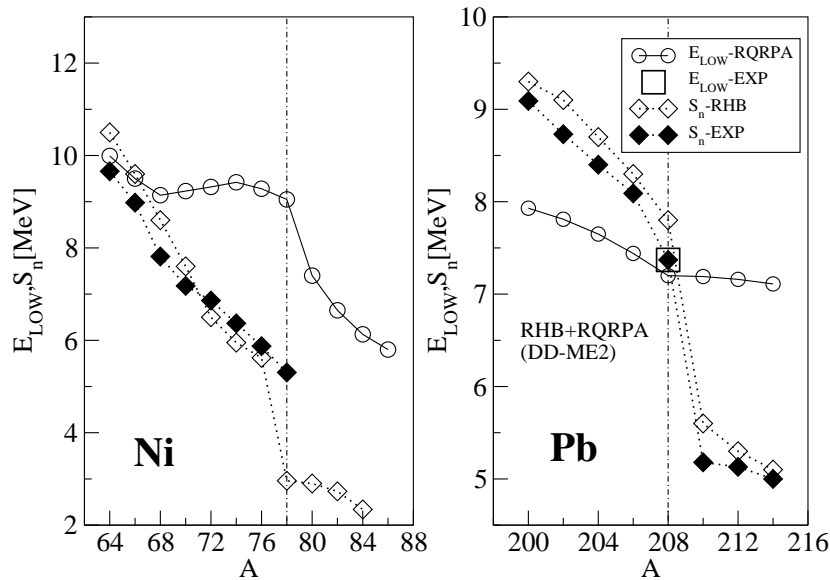


**Figure 22.** Same as in Fig. 18, but for the Ni and Pb isotopic chains. The large square denotes the experimental position of the PDR in  $^{208}\text{Pb}$  [133].

the PDR excitation energies is calculated already at  $A = 66$ . In heavier Ni isotopes the excitation energy of the PDR is predicted high above the neutron emission threshold. One should notice that for the lighter Ni isotopes the agreement between the calculated and experimental neutron separation energies is not as good as for the Sn nuclei and, therefore, the actual point of crossing between the PDR and the one-neutron separation energy could occur for  $A < 66$ . The Ni nuclei are not very rigid and, for a more quantitative description, one would have to go beyond the simple mean-field plus QRPA calculation and include correlation effects. For the Pb isotopes the crossing point is calculated at  $A = 208$ , in excellent agreement with the data on low-lying E1 excitations in  $^{208}\text{Pb}$  [133].

Motivated by the experimental results on the PDR in  $^{130}\text{Sn}$  and  $^{132}\text{Sn}$  [152], the relativistic RPA has recently been applied in the study of the isotopic dependence of the PDR in tin [165], focused on the following questions: (a) is there a correlation between the development of a neutron skin and the emergence of low-energy dipole strength? and (b) can the data be used to discriminate among effective interactions that predict different values for the neutron skin in heavy nuclei? The results of the RPA analysis are not conclusive because, although a strong linear correlation between the neutron skin and the fraction of the energy-weighted sum rule at low energy was observed, an anti-correlation actually developed beyond  $^{120}\text{Sn}$ , and it was attributed to the filling of the neutron  $1h_{11/2}$  orbital. It should be pointed out, however, that the analysis was performed on the RPA level, without considering the effect of pairing correlations. Comparing different effective interactions, it was found that the centroid energy of the

PDR is not sensitive to the density dependence of the symmetry energy. The fraction of the energy-weighted sum rule exhausted by the PDR, on the other hand, increases sharply with increasing neutron skin. Although the experimental error bars are large, the data seem to disfavor effective interactions with stiff symmetry energy, i.e. those which predict excessively large neutron skins.

#### 4.5. The Proton Electric Pygmy Dipole Resonance

Because the proton drip-line is much closer to the line of  $\beta$ -stability than the neutron drip-line, bound nuclei with an excess of protons over neutrons can be only found in the region of light  $Z \leq 20$  and medium mass  $20 < Z \leq 50$  elements. For  $Z > 50$ , nuclei in the region of the proton drip-line are neutron-deficient rather than proton-rich. In contrast to the evolution of the neutron skin in neutron-rich systems, because of the presence of the Coulomb barrier, nuclei close to the proton drip-line generally do not exhibit a pronounced proton skin, except for very light elements. Since in light nuclei the multipole response is generally less collective, all these effects seem to preclude the formation of the pygmy dipole states in nuclei close to the proton drip-line. Nevertheless, a recent analysis based on the RHB+RQRPA approach has shown that proton pygmy dipole states can develop in light and medium mass proton-rich nuclei [166].

In Fig. 23 we plot the ground state density profiles for the Ar isotopes and for the N=20 isotones, respectively, evaluated in the RHB model using the DD-ME2 effective interaction, and the Gogny D1S force in the pairing channel. In the both examples we observe the formation of the proton skin on the surface of nuclei which have a higher ratio of protons over neutrons. The proton skin is, of course, not so pronounced as neutron skin in neutron-rich nuclei, because of the Coulomb barrier which tends to localize the protons in the nuclear interior. Evidence for a possible formation of the proton skin in neutron-deficient or proton-rich nuclei has been reported in recent experimental studies [167], and is supported by model predictions [168, 169].

Only few studies of dipole excitations in proton-rich nuclei have been reported so far. The isovector dipole response of the proton drip-line nucleus  $^{34}\text{Ca}$  has been analyzed with the continuum RPA based on Skyrme interactions, and a multiple peak structure has been predicted between the low-energy isoscalar dipole response and the IV GDR [80]. In the large-scale shell-model calculations for  $^{13}\text{O}$  [170], pronounced E1 strength has been found in the low-energy region below 3 MeV, and related to the coherence in the transition amplitudes between the loosely-bound valence nucleons, and also between the core and the valence nucleons. The relativistic RPA calculation of the dipole response in Ar isotopes [171], has shown a concentration of strength in the proton-rich nuclei  $^{30}\text{Ar}$  and  $^{32}\text{Ar}$ , which has been attributed to excitations from weakly-bound single-particle states into the continuum. A recent study based on the self-consistent RHB+RQRPA framework has shown that a new collective mode – the Proton Pygmy Dipole Resonance (PPDR) could arise in medium-heavy nuclei close to the proton drip-line [166]. In Fig. 24 the RQRPA dipole strength distributions in the N=20 isotones

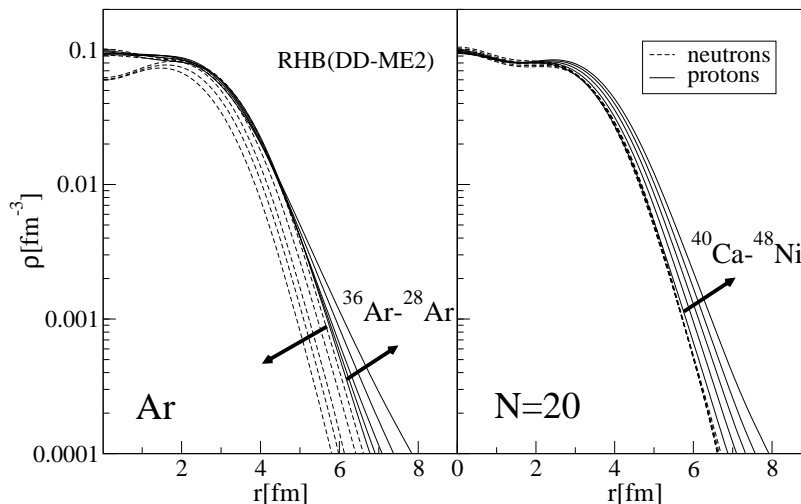


**Figure 23.** Neutron and proton ground-state density profiles for Ar isotopes (left panel), and N=20 isotones (right panel), evaluated in the RHB model with the DD-ME2 effective interaction. The arrows denote the increasing (decreasing) proton (neutron) density distributions along the isotopic, and isotonic chains.

$^{40}\text{Ca}$ ,  $^{42}\text{Ti}$ ,  $^{44}\text{Cr}$ , and  $^{46}\text{Fe}$  are shown, calculated with the fully consistent RHB+RQRPA with the DD-ME2 plus Gogny D1S effective interactions. The strength distributions are dominated by the IV GDR at  $\approx 20$  MeV excitation energy. With the increase of the number of protons, low-lying dipole strength appears in the region below the GDR and, for  $^{44}\text{Cr}$  and  $^{46}\text{Fe}$ , a pronounced low-energy peak is found at  $\approx 10$  MeV excitation energy. In the lower panel of Fig. 24 we plot the proton and neutron transition densities for the peaks at 9.98 MeV in  $^{44}\text{Cr}$  and 9.33 MeV in  $^{46}\text{Fe}$ , and compare them with the transition densities of the GDR state at 18.82 MeV in  $^{46}\text{Fe}$ . Obviously the dynamics of the two low-energy peaks is very different from that of the isovector GDR: the proton and neutron transition densities are in phase in the nuclear interior and there is almost no contribution from the neutrons in the surface region. As in the case of the PDR in neutron-rich nuclei, obviously the low-lying state does not belong to statistical E1 excitations sitting on the tail of the GDR, but could indeed represent a fundamental mode of excitation: the proton electric pygmy dipole resonance (PPDR).

In Fig. 25 we analyse the RQRPA structure of the dipole response in  $^{46}\text{Fe}$ . This nucleus is located at the proton drip-line, and recently evidence for ground-state two-proton radioactivity was reported in the decay of  $^{45}\text{Fe}$  [172, 173]. In the four panels we plot the QRPA amplitudes of proton and neutron  $2qp$  configurations

$$\xi_{2qp} = |X_{2qp}^\nu|^2 - |Y_{2qp}^\nu|^2 \quad (77)$$

for the three low-lying states at 8.91, 9.33, and 10.11 MeV, as well as for the strongest state in the GDR region at 18.82 MeV. For each of the four dipole states, in addition



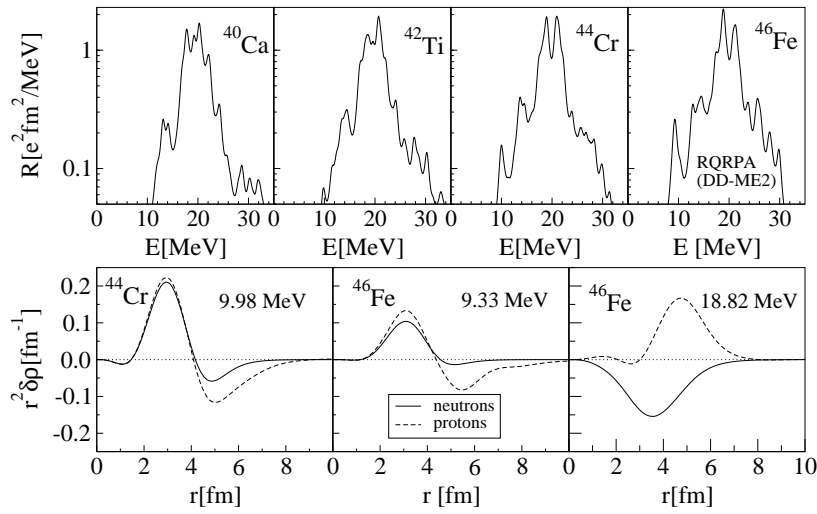


**Figure 24.** The RHB+RQRPA isovector dipole strength distributions in the N=20 isotones (upper panel). The proton and neutron transition densities for the low-lying states in  $^{44}\text{Cr}$  and  $^{46}\text{Fe}$ , and for the IV GDR state in  $^{46}\text{Fe}$  are shown in the lower panel.

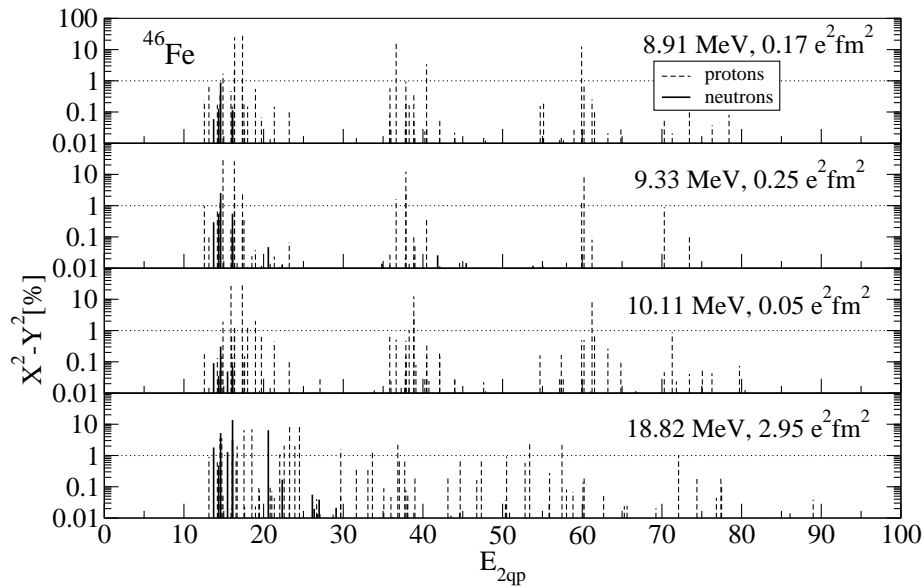


**Figure 25.** The distributions of the RQRPA amplitudes in  $^{46}\text{Fe}$ , plotted as functions of the unperturbed energy of the respective  $2qp$ -configurations, for the main peaks in the low-energy region and for the IV GDR state.

to the excitation energy we have also included the corresponding  $B(E1)$  value. The amplitudes are shown in a logarithmic plot as functions of the unperturbed energy of the respective  $2qp$ -configurations. Only amplitudes which contribute more than 0.01% are shown, and we also differentiate between proton and neutron configurations. We note that, rather than a single proton  $2qp$  excitation, the low-lying states are characterized by a superposition of a number of  $2qp$  configurations. Obviously the pygmy states display a degree of collectivity that can be directly compared with the QRPA structure of the GDR state at 18.82 MeV. In addition, proton  $2qp$  configurations account for  $\approx 99\%$  of the QRPA amplitude of the pygmy states, whereas the ratio of the proton to neutron contribution to the GDR state is  $\approx 2$ . For the GDR states the  $2qp$  configurations predominantly correspond to excitations from the  $sd$ -shell to the  $fp$ -shell. The structure of the pygmy states, on the other hand, is dominated by transitions from the  $1f_{7/2}$  proton state at -0.21 MeV, and from the  $2p_{3/2}$  proton state at 3.63 MeV (this state is only bound because of the Coulomb barrier). The energy weighted sum of the strength below 11 MeV excitation energy corresponds to 2.7% of the TRK sum rule.

Another example where a pronounced proton PDR can occur are the proton-rich isotopes of Ar. In the left panel of Fig. 26 we display the RHB+RQRPA electric dipole strength distribution in  $^{32}\text{Ar}$ . In addition to the rather fragmented GDR structure at  $\approx 20$  MeV, prominent proton PDR peaks are calculated at 8.14, 8.79, 9.22, and 9.46 MeV. These peaks form the pygmy structure and exhaust 5.7 % of the TRK sum rule. The RQRPA amplitudes of the low-lying states present superpositions of many proton  $2qp$  configurations, with the neutron contributions at the level of 1%. The dominant configurations correspond to transitions from the proton states  $1d_{3/2}$  (-1.94 MeV) and  $2s_{1/2}$  (-3.98 MeV). In the right panel of Fig. 26 we display the mass dependence of the centroid energy of the pygmy peaks and the corresponding values of the integrated  $B(E1)$  strength below 10 MeV excitation energy. In contrast to the case of medium-heavy and heavy neutron-rich isotopes, in which both the PDR and GDR are lowered in energy with the increase of the neutron number, in proton-rich isotopes the mass dependence of the PDR excitation energy and  $B(E1)$  strength is opposite to that of the GDR. The proton PDR decreases in energy with the development of the proton excess. This mass dependence is intuitively expected because the proton PDR is dominated by transitions from weakly-bound proton orbitals. As the proton drip-line is approached, either by increasing the number of protons or by decreasing the number of neutrons, due to the weaker binding of higher proton orbitals one expects more inert oscillations, i.e. lower excitation energies. The number of  $2qp$  configurations which include weakly-bound proton orbitals increases towards the drip-line, resulting in an enhancement of the low-lying  $B(E1)$  strength.

For heavier nuclei the proton drip-line is located in the region of neutron-deficient, rather than proton-rich nuclei, and therefore one does not expect to find low-lying dipole strength in medium-heavy and heavy nuclei close to the proton drip-line.

The effect of the coupling to the continuum on the low-lying dipole strength in nuclei close the proton drip-line has also been analyzed in the non-relativistic continuum RPA

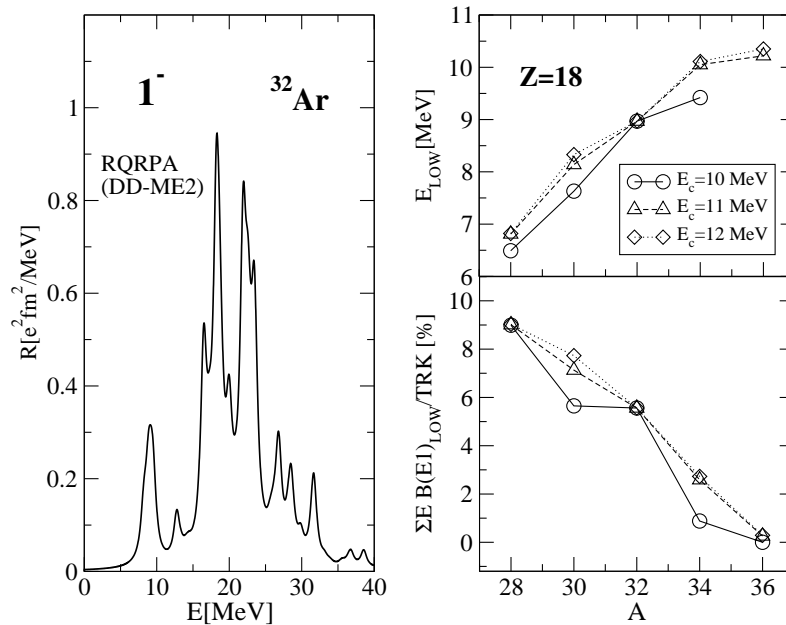


**Figure 26.** The RHB+RQRPA isovector dipole strength distribution in  $^{32}\text{Ar}$  (left panel). The mass dependence of the PPDR centroid energy for Ar isotopes, and the corresponding values of the integrated  $B(E1)$  strength below  $E_c=10, 11,$  and  $12$  MeV are shown in the right panel.

(CRPA) framework, using Skyrme interactions [80, 174]. In the doubly magic nucleus  $^{48}\text{Ni}$  both the CRPA and the RRPA predict the occurrence of the proton PDR, but the CRPA analysis has shown that, as a result of the coupling to the continuum, the PPDR is characterized by a rather large escape width [174].

#### 4.6. Di-neutron Correlations near the Drip-Line

The existence of another exotic mode has been suggested in medium-heavy nuclei close to the neutron drip-line: a soft dipole excitation that corresponds to the vibration of a di-neutron in the nuclear exterior against the remaining  $A-2$  subsystem [175, 176]. While in nuclei with a pronounced neutron excess the pygmy dipole resonance could appear, di-neutron *vs* core vibrations may occur in very exotic nuclei near the neutron drip-line. The latter mode is strongly influenced by neutron pairing correlations, and is characterized by a large transition density for pair motion of neutrons. In the case of light halo-nuclei pairing correlations between the loosely-bound neutrons in the halo lead to a strong enhancement of the soft dipole excitations. Experimental signatures of di-neutron correlation in the soft dipole mode have been found in  $^{11}\text{Li}$  [72, 73]. However, as has recently been shown in Ref. [175], some features of di-neutron correlations may also be present in the ground states of exotic medium-mass nuclei, and therefore influence their excitations.

In the HFB description of the nuclear ground state (cf. Sec. 2.1), the spatial correlations between a pair of neutrons can be probed by the neutron two-body correlation density [175],

$$\rho_{corr}(\mathbf{r}\sigma, \mathbf{r}'\sigma') = |\kappa(\mathbf{r}\sigma, \mathbf{r}'\bar{\sigma}')|^2 - |\rho(\mathbf{r}\sigma, \mathbf{r}'\sigma')|^2, \quad (78)$$

defined by the off-diagonal terms of the pairing tensor (Eq. (3)), and density matrix (Eq. (2)). The notation  $\bar{\sigma}$  has been defined in Eq. (49). In the case of medium-heavy nuclei close to the neutron drip-line, it has been shown that the two-body correlation density clearly reflects the presence of spatial di-neutron correlations in the pair-correlated ground state, and these are especially pronounced on the surface and in the region of the neutron-skin. The di-neutron correlation originates from a coherent superposition of quasiparticle orbits with large orbital angular momenta, which are embedded in the nucleon continuum.

Here we illustrate the role of neutron-pair correlations with the example of the dipole response in  $^{158}\text{Sn}$  [176]. The HFB calculation of the ground state has been performed with the Skyrme effective interaction SLy4, and the density-dependent delta-interaction of Eq. (15) in the pairing channel. The overall strength parameter of the pairing force has been adjusted to reproduce the  $^1\text{S}$  scattering length  $a = -18$  fm in free space. By varying the value of the parameter  $\eta$ , which multiplies the density-dependent term (see Eq. (15)), one controls the effective pairing interaction. A smaller value of  $\eta$ , i.e. a weaker density dependence, results in stronger pairing in the interior of the nucleus. For the particular case of Sn isotopes,  $\eta = 0.71$  has been adjusted so that the average pairing gap becomes comparable to the experimental value  $\Delta = 1.1 - 1.4$  MeV. The choice  $\eta = 0$  corresponds to a density-independent pairing interaction with an extremely large and unrealistic pairing gap  $\Delta \approx 15$  MeV.

The response function has been calculated with the continuum QRPA (cf. Sec. 2.3), which employs the quasiparticle Green's function with exact outgoing boundary condition for neutrons [176]. For the  $ph$  residual QRPA interaction, the Landau-Migdal approximation to the Skyrme functional has been used, whereas the pairing correlations have been consistently described by the same density-dependent delta-interaction (15), both in the HFB and QRPA. An additional renormalization factor must be introduced in the  $ph$  channel in order to remove the spurious center-of-mass contributions.

In Fig. 27 the HFB+QRPA dipole strength function for  $^{158}\text{Sn}$  is shown for different choices of the parameter of the pairing interaction:  $\eta = 0, 0.3, 0.5$  and  $0.71$ . For the realistic value of  $\eta = 0.71$ , in addition to the IVGDR in the high-energy region between 10 and 15 MeV, the strength distribution exhibits a pronounced low-energy structure below 5 MeV. In the case of extremely strong pairing ( $\eta=0$ ), the transition strength basically contains only a single broad resonance centered at 11 MeV.

The structure of the characteristic low-energy peak at 4.4 MeV, obtained in the realistic calculation with  $\eta = 0.71$ , is explored in more details in Fig. 28, where the corresponding transition densities are shown [176]. A large contribution of the neutron particle-pair transition density is found in the region beyond the nuclear surface. It

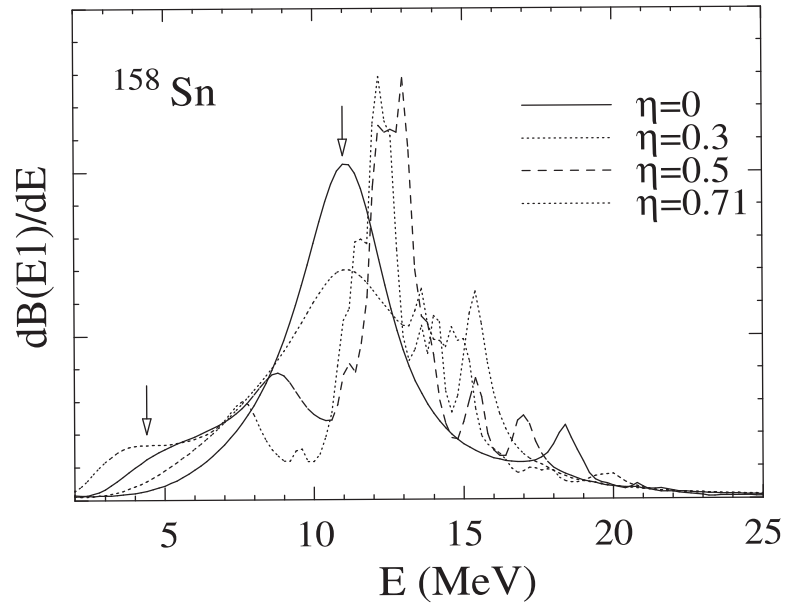


**Figure 27.** The HFB+QRPA isovector dipole strength function in  $^{158}\text{Sn}$ . The strength distributions obtained for several values of the pairing parameter  $\eta = 0, 0.3, 0.5$  and  $0.71$  are shown [176].

originates from dynamical pairing correlations among neutrons moving in the external region, i.e., the QRPA correlation is determined by the pairing interaction. The dynamics of this soft mode can be interpreted as the vibration of di-neutrons against the core. Because of the influence of neutron pairing correlations, this mode has a dominant particle-particle character. The two-quasiparticle configurations, including orbitals in the continuum with orbital angular momenta up to  $l \approx 10$ , contribute coherently to the large particle-pair transition density. Let us also note that in the continuum QRPA calculations of Ref. [176], the quadrupole core *vs* dineutron mode has also been predicted in the low-energy region, but only for a very strong, and therefore unrealistic, pairing interaction.

## 5. Isoscalar Modes

### 5.1. Isoscalar Dipole Compressional and Toroidal Modes

Experimental excitation energies of compressional (monopole and dipole) vibrational modes in atomic nuclei can in principle be used to deduce the value of the nuclear matter compression modulus  $K_{nm}$  [177]. This quantity is related to the curvature of the nuclear matter equation of state at the saturation point, and controls basic properties of atomic nuclei, the structure of neutron stars, the dynamics of heavy-ion collisions and of supernovae explosions. The nuclear matter compressibility cannot be measured directly, but rather deduced from a comparison of experimental excitation energies of isoscalar giant monopole resonances (ISGMR), with the corresponding values predicted by microscopic nuclear effective interactions characterized by different values of  $K_{nm}$ .

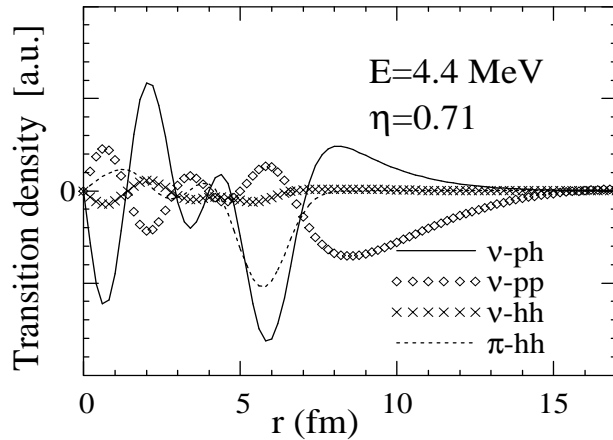


**Figure 28.** The transition densities for the dipole peak at  $E = 4.4$  MeV in  $^{158}\text{Sn}$ , calculated with the value  $\eta = 0.71$  for the parameter of the density-dependent pairing interaction [176]. The curves correspond to the neutron particle-hole transition density (solid), neutron particle-pair transition density (diamonds), neutron hole-pair transition density (crosses), and the proton particle-hole transition density (dashed).

Inelastic  $\alpha$ -scattering experiments have been used in high precision studies of the systematics of ISGMR in nuclei with  $A \geq 90$ . Nuclear structure models provide a consistent description of the main moments of strength distributions and the mass dependence of excitation energies, and thus relate the ISGMR to the nuclear matter compression modulus. There is much less experimental information, and only few microscopic theoretical analyses of the structure of compressional modes in lighter nuclei with  $A < 90$ . While in heavy nuclei the shape of the ISGMR strength distribution is typically symmetric, for  $A < 90$  the ISGMR display asymmetric shapes with a slower slope on the high energy side of the peak, and with a further decrease of the mass number the ISGMR strength distributions become strongly fragmented. The determination of  $K_{nm}$  is based on microscopic calculations of ISGMR excitation energies. Interactions that differ in their prediction of the nuclear matter compressibility, but otherwise reproduce experimental data on ground-state properties reasonably well, are used to calculate ISGMR in the random phase approximation or the time-dependent framework. A fully self-consistent calculation of both ground-state properties and ISGMR excitation energies restricts the range of possible values for  $K_{nm}$ . It has been pointed out, however, that, since  $K_{nm}$  determines bulk properties of nuclei and, on the other hand, the ISGMR excitation energies depend also on the surface compressibility, measurements and microscopic calculations of ISGMR in heavy nuclei should, in principle, provide a more reliable estimate of the nuclear matter compressibility [177, 178].

Recent theoretical studies of nuclear compressional modes have employed the fluid dynamics approach [179], the Hartree-Fock plus random phase approximation (RPA) [180, 181, 182, 183], the RPA based on separable Hamiltonians [184], linear response within a stochastic one-body transport theory [185], the relativistic transport approach [186], and the self-consistent relativistic RPA [187, 188, 189, 190]. Several

analyses have emphasized the importance of a fully self-consistent description of ISGMR, and confirmed that the low value of  $K_{nm} = 210 - 220$  MeV, previously obtained with Skyrme functionals, is an artefact of the inconsistent implementation of effective interactions [183, 191]. The excitation energies of the ISGMR in heavy nuclei are thus best described with Skyrme and Gogny effective interactions with  $K_{nm} \approx 235$  MeV. In Ref. [182] it has been shown that it is also possible to construct Skyrme forces that fit nuclear ground state properties and reproduce ISGMR energies, but with  $K_{nm} \approx 255$  MeV. In Ref. [183] a new set of Skyrme forces was constructed that spans a wider range of values of  $K_{nm}$  and the symmetry energy at saturation density  $a_4$ . RPA calculations with these forces have shown that the ISGMR data can be reproduced either with forces having a softer density-dependent term (the exponent  $\alpha = 1/6$  in Eq. (14)) and  $K_{nm} \sim 230 - 240$  MeV, or with forces having a stiffer density-dependent term ( $\alpha = 1/3$ ) and  $K_{nm} \sim 250 - 260$  MeV. Other forces, in particular those characterized by larger values of  $K_{nm}$ , are associated with unrealistic values of the effective mass, and do not reproduce ground-state properties. On the other hand, it appears that in the relativistic framework the interval of allowed values for  $K_{nm}$  is more restricted. A recent relativistic RPA analysis based on modern effective Lagrangians with explicit density dependence of the meson-nucleon vertex functions, has shown that only effective interactions with  $K_{nm} = 250 - 270$  MeV reproduce the experimental excitation energies of ISGMR in medium-heavy and heavy nuclei, and that  $K_{nm} \approx 250$  MeV represents the lower limit for the nuclear matter compression modulus of relativistic mean-field interactions [190].

The isoscalar giant dipole resonance (ISGDR) is a second order effect, built on  $3\hbar\omega$ , or higher configurations. It corresponds to a compression wave traveling back and forth through the nucleus along a definite direction. Recent data on the compressional ISGDR in  $^{90}\text{Zr}$ ,  $^{116}\text{Sn}$ ,  $^{144}\text{Sm}$ , and  $^{208}\text{Pb}$  [192, 193, 194, 195] can also be used to constrain the range of allowed values of  $K_{nm}$  [196]. The problem, however, is that the isoscalar E1 strength distributions display a characteristic bimodal structure with two broad components: one in the low-energy region close to the isovector giant dipole resonance (IVGDR) ( $\approx 2\hbar\omega$ ), and the other at higher energy close to the electric octupole resonance ( $\approx 3\hbar\omega$ ). Theoretical analyses have shown that only the high-energy component represents compressional vibrations [34, 197], whereas the broad structure in the low-energy region could correspond to vortical nuclear flow associated with the toroidal dipole moment [198, 199, 200]. However, as has also been pointed out in the recent study of the interplay between compressional and vortical nuclear currents [199], a strong mixing between compressional and vorticity vibrations in the isoscalar E1 states can be expected up to the highest excitation energies in the region  $\approx 3\hbar\omega$ . Nevertheless, models which use effective interactions with  $K_{nm}$  adjusted to ISGMR excitation energies in heavy nuclei, also reproduce the overall structure of the high-energy portion of ISGDR data [181, 194, 195, 201, 202].

Accurate data on compressional modes are becoming available also for lighter nuclei, e.g.  $^{56}\text{Fe}$ ,  $^{58}\text{Ni}$ ,  $^{60}\text{Ni}$  [203, 204]. Inelastic  $\alpha$ -scattering data on the isoscalar monopole and dipole strength distributions have been analyzed in the relativistic quasiparticle

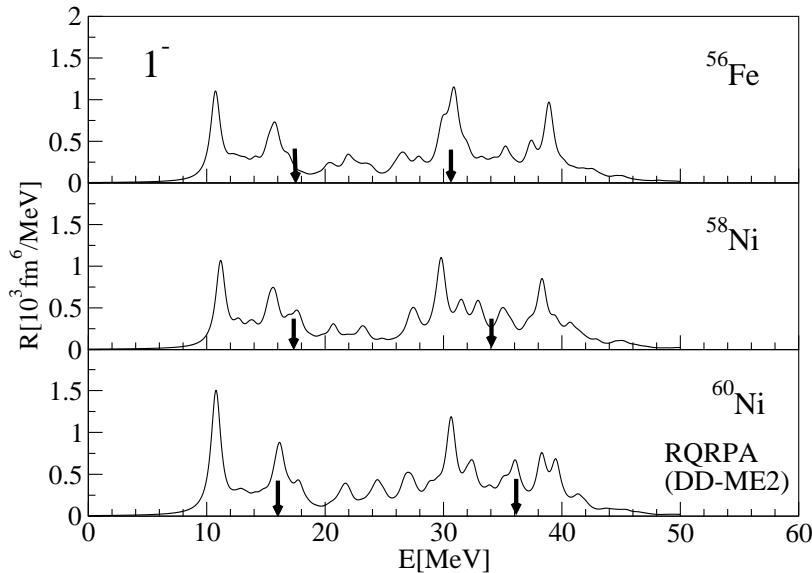


**Figure 29.** The RHB+RQRPA isoscalar dipole transition strength in  $^{56}\text{Fe}$ ,  $^{58}\text{Ni}$ , and  $^{60}\text{Ni}$  calculated with DD-ME2 effective interaction. The arrows denote the positions of the experimental centroid energies of the low- and high-energy components [203].

random-phase approximation (RQRPA) with the DD-ME2 effective nuclear interaction in the particle-hole channel and the finite-range Gogny force in the particle-particle channel [205]. In Fig. 29 we display the strength functions in  $^{56}\text{Fe}$  and  $^{58,60}\text{Ni}$ , for the isoscalar dipole operator:

$$\hat{Q}_{1\mu}^{T=0} = \sum_{i=1}^A \gamma_0 \left( r_i^3 - \frac{5}{3} \langle r^2 \rangle_0 r_i \right) Y_{1\mu}(\Omega_i), \quad (79)$$

where  $\langle r^2 \rangle_0$  denotes the ground-state expectation value, and the inclusion of the second term in the operator ensures that the strength distribution does not contain spurious components that correspond to the center-of-mass motion. In all three nuclei the strength is strongly fragmented and distributed over a wide range of excitation energy between 10 MeV and 40 MeV, in agreement with the experimental results of Ref. [203]. In the experiment between 56% and 72% of the isoscalar E1 strength has been located in these nuclei below 40 MeV excitation energy, and some missing strength probably lies at higher energies. Similarly to the results obtained for heavier nuclei [34, 197, 200], the E1 strength is basically concentrated in two broad structures: one in the region  $10 \text{ MeV} \leq E_x \leq 20 \text{ MeV}$ , and the high-energy component above 25 MeV and extending above 40 MeV excitation energy. Only the high-energy portion of the calculated E1 strength is sensitive to the nuclear matter compression modulus of the effective interaction. The thick arrows denote the locations of the experimental centroid energies



( $m_1/m_0$ ) in the low- and high-energy regions of the isoscalar E1 strength in  $^{56}\text{Fe}$ ,  $^{58}\text{Ni}$ , and  $^{60}\text{Ni}$  [203]. We notice a good qualitative agreement between the calculated and experimental centroids in the high-energy region, especially taking into account that the isoscalar strength above  $E_x = 40$  MeV has not been observed in the experiment. In the low-energy region, however, the theoretical centroid energies are systematically below the experimental values by  $\approx 1\text{--}4$  MeV. This effect is in agreement with previous RRPA calculations in heavier nuclei [200], and supports the picture of pronounced mixing between compressional and vorticity vibrations in the intermediate region of excitation energies.

The role of toroidal multipole form factors and moments in the physics of electromagnetic and weak interactions has been extensively discussed in Refs. [206] and [207]. They appear in multipole expansions for systems containing convection and induction currents. In particular, the multipole expansion of a four-current distribution gives rise to three families of multipole moments: charge moments, magnetic moments and electric transverse moments. The latter are related to the toroidal multipole moments and result from the expansion of the transverse electric part of the current. The toroidal dipole moment, in particular, describes a system of poloidal currents on a torus. Since the charge density is zero for this configuration, and all the turns of the torus have magnetic moments lying in the symmetry plane, both the charge and magnetic dipole moments of this configuration are equal to zero. The simplest model is an ordinary solenoid bent into a torus.

Vortex waves in nuclei were analyzed in a hydrodynamic model [208]. By relaxing the assumption of irrotational motion, in this pioneering study solenoidal toroidal vibrations were predicted, which correspond to the toroidal giant dipole resonance at excitation energy  $E_x \approx (50 - 70)/A^{1/3}$  MeV. It was suggested that the vortex excitation modes should appear in electron backscattering. The isoscalar  $1^-$  toroidal dipole states were studied in the framework of the time-dependent Hartree-Fock theory by analyzing the dynamics of the moments of the Wigner transform of the density matrix [209], and excitations with dipole toroidal structure were also found in semi-classical studies based on nuclear fluid dynamics [198, 199]. The first fully microscopic analysis of toroidal dipole resonances (TGDR) was performed in the framework of the relativistic RPA [129, 200]. Compressional and toroidal dipole modes were also studied with the Quasiparticle Phonon Model, using separable residual interactions with the Nilsson or Woods-Saxon mean-field potentials [184]. Continuum RPA calculations with Skyrme interactions in Ni isotopes have shown that vortex waves could also occur for excitations with higher multi-polarities  $2^+$ ,  $3^-$  and  $4^+$  [210].

In Fig. 30 we display the RRPA dipole strength distributions in  $^{208}\text{Pb}$  for the isoscalar dipole operator (ISGDR) in the upper panel, and for the isoscalar toroidal dipole operator (TGDR)

$$\hat{T}_{1\mu}^{T=0} = -\sqrt{\pi} \sum_{i=1}^A \left[ r_i^2 \left( \vec{Y}_{10\mu}^*(\Omega_i) + \frac{\sqrt{2}}{5} \vec{Y}_{12\mu}^*(\Omega_i) \right) \cdot \vec{\alpha}_i - \langle r^2 \rangle_0 \vec{Y}_{10\mu}^*(\Omega_i) \cdot \vec{\alpha}_i \right], \quad (80)$$

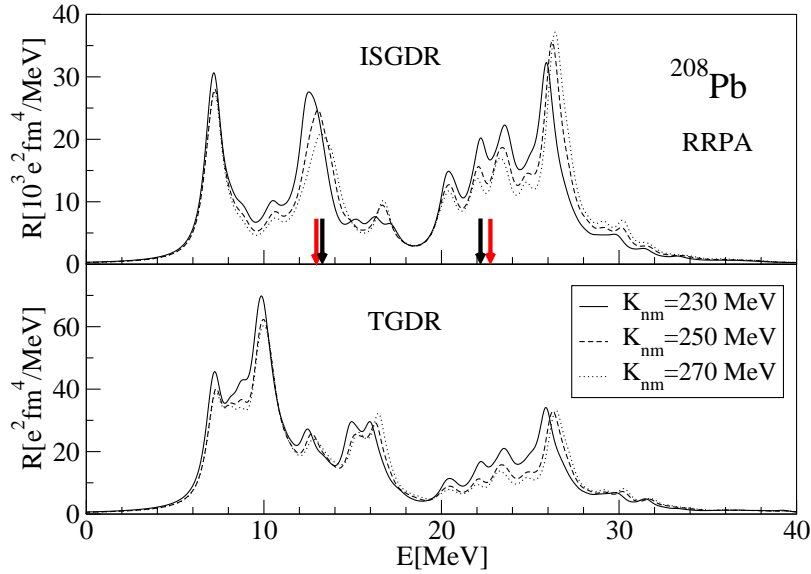


**Figure 30.** Isoscalar dipole (upper panel) and toroidal dipole strength distributions (lower panel) for  $^{208}\text{Pb}$ , calculated with the RRPA based on three density-dependent interactions with  $K_{nm}=230, 250,$  and  $270$  MeV. The  $(\alpha, \alpha')$  experimental data for the centroids of the low-energy and high-energy portions of the isoscalar dipole distribution are denoted by dark [211] and light [194, 195] arrows.

in the lower panel.  $\vec{Y}_{w\mu}$  denotes a vector spherical harmonic, and  $\vec{\alpha}$  are the Dirac  $\alpha$ -matrices. As in the case of the dipole operator Eq. (79), the second term ensures that the TGDR strength distributions do not contain spurious center-of-mass motion components. To illustrate the correlation between the nuclear matter compressibility and the isoscalar dipole response, the strength functions are calculated with three different relativistic effective interactions with  $K_{nm}=230, 250,$  and  $270$  MeV, and the volume asymmetry at saturation  $a_4=32$  MeV [190]. The experimental centroids of the low-energy and high-energy portions of the dipole strength distributions, extracted from small angle  $\alpha$ -scattering spectra, are denoted by arrows [195, 211].

The positions of the calculated peaks in the low-energy region (below 20 MeV) depend only weakly on the incompressibility, whereas the structures in the high-energy region are much more sensitive to the choice of the compression modulus of the interaction. Both dipole strength distributions display two broad structures: one at low energies between 8 and 20 MeV, and one in the high-energy region 20 – 30 MeV. Obviously, a strong coupling between the two isoscalar  $1^-$  modes can be expected. This coupling becomes even more evident if one rewrites the expression in square brackets of the toroidal operator Eq. (80) as [208]

$$\nabla \times (\vec{r} \times \nabla) \left( r^3 - \frac{5}{3} \langle r^2 \rangle_0 r \right) Y_{1\mu}, \quad (81)$$

and compares it with the isoscalar dipole operator of the compression mode (79). The

relative position of the two resonance structures will, therefore, depend on the interaction between the toroidal and compression modes. In Table 2 we compare the RQRPA centroid energies of the low-lying portion of the response to the toroidal operator, with the corresponding experimental values for  $^{116}\text{Sn}$ ,  $^{144}\text{Sm}$ , and  $^{208}\text{Pb}$  [195, 211]. We notice that the theoretical centroids, calculated with the DD-ME2 effective interaction, are systematically located  $\approx 1 - 2$  MeV below the experimental values. The dynamics of the solenoidal toroidal vibrations is illustrated in Fig. 31, where we plot the velocity fields for the three most pronounced peaks of TGDR response function in  $^{208}\text{Pb}$  (calculated with DD-ME2). A vector of unit length is assigned to the largest velocity. All the other velocity vectors are normalized accordingly. Since the collective flow is axially symmetric, we plot the velocity field in cylindrical coordinates. The  $z$ -axis corresponds to the symmetry axis of a torus. The lowest peak at 7.2 MeV is dominated by vortex collective motion. The velocity fields in the  $(z, r_{\perp})$  plane correspond to poloidal currents on a torus with vanishing inner radius. The poloidal currents determine the dynamical toroidal moment. The high-energy peak at 26.1 MeV displays the dynamics of dipole compression mode. The “squeezing” compression mode is identified by the flow lines which concentrate in the two “poles” on the symmetry axis. The velocity field corresponds to a density distribution which is being compressed in the upper half-plane, and expands in the lower half-plane. The centers of compression and expansion are located on the symmetry axis, at approximately half the distance between the center and the surface of the nucleus. Finally, the intermediate peak at 10.0 MeV displays the coupling between the toroidal and compression dipole modes. A very similar behavior of the velocity distributions as function of excitation energy is also observed for  $^{116}\text{Sn}$  and  $^{144}\text{Sm}$ . A direct experimental evidence for the TGDR mode remains a challenge for future studies. In principle the vortex type of motion could be identified in the measurement of transverse electron scattering form factors. An exploratory study with the quasiparticle phonon model (QPM) has shown that the cross sections in electron back-scattering could differentiate between the toroidal and neutron-skin dipole modes [212]. The respective QPM electron scattering form factors at  $180^\circ$  are shown in Fig. 32, for transitions dominated by the toroidal and neutron-skin oscillations. Information about the nature of the low-lying dipole excitations could be obtained in the range of incident energies 40–90 MeV, even though the predicted values for the cross sections are low [212].

	$m_1/m_0(\text{MeV})$	$E_x(\text{MeV})$ [195]	$E_x$ (MeV) [211]
$^{116}\text{Sn}$	13.3	$15.6 \pm 0.5$	$14.38 \pm 0.25$
$^{144}\text{Sm}$	12.7	$14.2 \pm 0.2$	$14.00 \pm 0.30$
$^{208}\text{Pb}$	11.2	$13.0 \pm 0.1$	$13.26 \pm 0.30$

**Table 2.** The RQRPA centroid energies of TGDR calculated with the DD-ME2 effective interaction in the region below 20 MeV excitation energy, compared with the corresponding experimental centroid energies from Refs. [195] and [211].

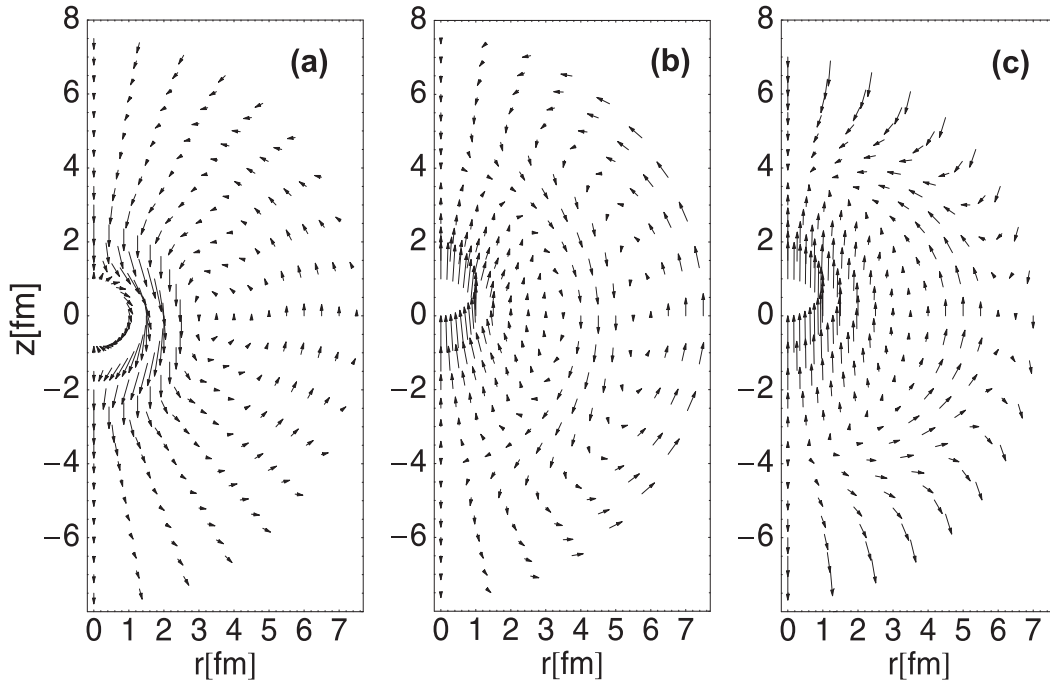


**Figure 31.** Velocity distributions for the three most pronounced peaks in the TGDR response of  $^{208}\text{Pb}$  (calculated with the DD-ME2 effective interaction). The velocity fields correspond to the peaks at (a) 7.2 MeV, (b) 10.0 MeV and (c) 26.1 MeV.

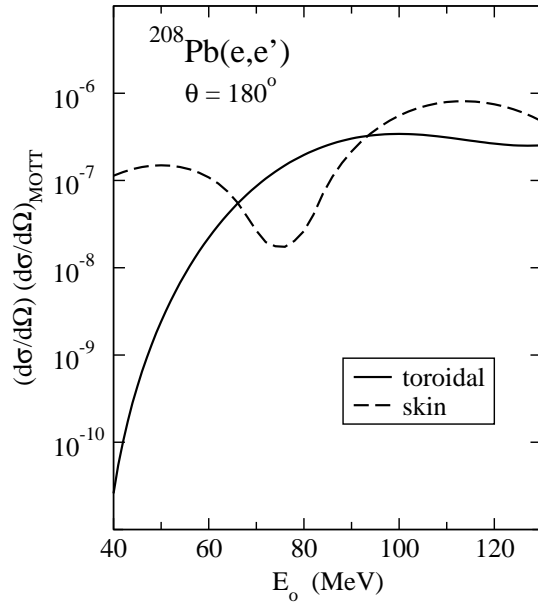


**Figure 32.** Electron scattering form factors of dipole transitions at  $180^\circ$  for  $^{208}\text{Pb}$ , based on calculations with the quasiparticle phonon model [212]. The two curves correspond to predominantly toroidal (solid) and neutron-skin (dashed) density oscillations, respectively.

	$E_{exp}$ (MeV)	$B(E2)_{exp}$ ( $e^2 \cdot \text{fm}^4$ )	$\frac{M_n/M_p}{N/Z}$
$^{18}\text{O}$	2.0	$45 \pm 2$	$0.9 \pm 0.2$
$^{20}\text{O}$	1.7	$28 \pm 2$	$2.2 \pm 0.5$
$^{22}\text{O}$	3.2	$21 \pm 8$	$1.4 \pm 0.5$
$^{24}\text{O}$	$> 3.8$	-	-

**Table 3.** Experimental values of excitation energies, electromagnetic transition probabilities, and ratios of the transition matrix elements, for the first  $2^+$  states in neutron-rich oxygen isotopes.

### 5.2. Low-Lying Quadrupole States in Unstable Nuclei

In most even-even nuclei the first excited state is a  $J^\pi=2^+$ . For magic nuclei the electric transition from the ground state to the first  $2^+$  state reflects directly the structure of the shell gap. The systematics of the  $2_1^+$  energies is very important in studies of shell evolution in nuclei far from stability. In particular, low-lying quadrupole states are closely related to the phenomenon of nuclear superfluidity: the  $2_1^+$  states are built from nucleonic configurations located close to the Fermi surface, which is precisely the energy region in which the pairing interaction is most effective [1, 4].

In oxygen isotopes the evolution of shell structure can be explored from the stable isotope to the neutron drip-line in just a few mass units (cf. also Sec. 4.2). A number of experimental [213, 214, 215, 216, 217, 218, 219] and theoretical [29, 30, 220, 221, 222, 223] studies of neutron-rich oxygen nuclei have been reported. Recent theoretical analyses have predicted the appearance of new magic numbers in  $^{22}\text{O}$  ( $N=14$ ) [223], and  $^{24}\text{O}$  ( $N=16$ ). Shell-model calculations [224] also show a strong gap  $\approx 4.3$  MeV between the  $1d_{5/2}$  and  $2s_{1/2}$  subshells, and thus  $^{22}\text{O}$  appears to be a magic nucleus. Accordingly, both QRPA [216] and shell-model [223, 225] calculations predict a decrease of the  $B(E2; 2_1^+ \rightarrow 0_1^+)$  from  $^{20}\text{O}$  to  $^{22}\text{O}$ . This has been confirmed by recent experimental results [215, 218, 219]. Table 3 summarizes the experimental values of excitation energies and  $B(E2)$  values for the  $2_1^+$  state in neutron-rich isotopes.

The energy of the first  $2^+$  state in  $^{22}\text{O}$  has been measured at 3199(8) keV [217], compared to 1670 keV in  $^{20}\text{O}$ , and its small  $B(E2)$  value of 21(8)  $e^2 \cdot \text{fm}^4$  [215] indicates a strengthening of the  $N=14$  shell gap. Even though the  $2_1^+$  state of  $^{24}\text{O}$  has not been observed directly, it has been shown that its energy must lie above 3.8 MeV, and this points to  $N=16$  as a new shell closure [218].  $^{28}\text{O}$ , which is a doubly magic nucleus in the standard shell model, was found to be neutron unbound [213].

Both the Gogny functionals [125, 226], and Skyrme interactions with density dependent pairing (cf. Eq. (15)) [29, 30, 216, 227], have been employed in recent QRPA studies of the structure of  $2_1^+$  states in exotic nuclei. In Fig. 33 we display the quadrupole response function in  $^{20}\text{O}$ , calculated with the Skyrme interactions SLy4 [16], SGII [228] and SIII [15]. In addition to the strong  $2_1^+$  state at  $\approx 3$  MeV, the pronounced structure above 20 MeV corresponds to the isoscalar giant quadrupole resonance (IS GQR). Obviously the details of the calculated quadrupole strength function depend on

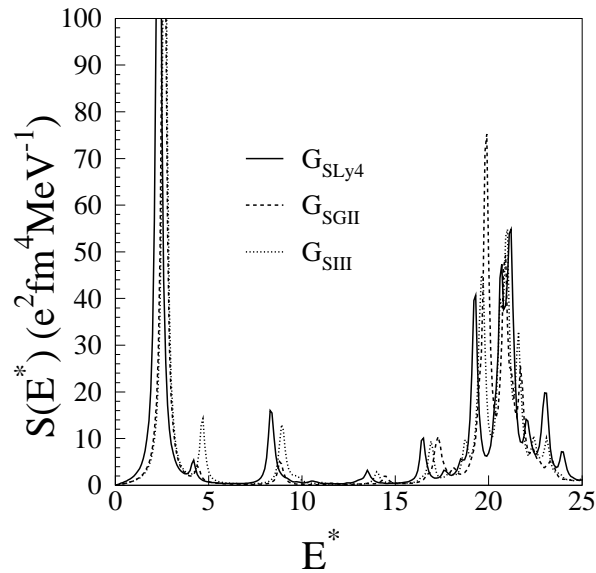


**Figure 33.** The QRPA isoscalar quadrupole strength function for the  $^{20}\text{O}$  nucleus, calculated with the SLy4, SGII and SIII Skyrme forces.

the choice of the interaction. The choice of the pairing interaction, in particular, plays an important role in the calculation of the  $2_1^+$  states. This is illustrated in Fig. 34 which compares the isoscalar quadrupole strength functions of  $^{18}\text{O}$ , calculated with two different pairing interactions Eq. (15). In addition to the density-dependent (surface-type pairing) interaction of Eq. (15), a density-independent interaction (volume-type pairing) i.e.  $\eta=0$  in Eq. (15), has been used in the pairing channel. The strength parameter is adjusted to the empirical pairing gap in  $^{18}\text{O}$ . We note that without any density dependence in the pairing channel, the calculated excitation energy of the  $2_1^+$  state is in better agreement with the experimental value of  $\approx 2$  MeV (see Table 3). This shows that an analysis of low-lying quadrupole states in neutron-rich nuclei can be used to determine the structure and medium dependence of effective pairing interactions [229].

The calculated transition densities of the  $2_1^+$  state in neutron-rich oxygen isotopes are shown in Fig. 35. While the peak in the proton transition density does not change its position with the increase of the number of neutrons, the radial dependence of the neutron transition density clearly reflects the formation of the neutron skin, especially in  $^{22}\text{O}$  and  $^{24}\text{O}$ . The decrease in magnitude of the neutron transition density in  $^{24}\text{O}$  can be related to the predicted  $N=16$  magic neutron number, which appears because of the  $2s_{1/2}$  subshell closure, i.e. the  $2s_{1/2}$  state is more bound in  $^{24}\text{O}$  than in  $^{22}\text{O}$ .

The measured  $B(E2; 2_1^+ \rightarrow 0_1^+)$  values are nicely reproduced by QRPA calculation, except for the problematic  $^{18}\text{O}$  [29]. In this nucleus a large discrepancy between the empirical and theoretical  $B(E2)$  values has been found in several shell-model [225, 230] and QRPA calculations [216, 226]. This could be explained by the presence of deformed states in the experimental low-lying spectrum of  $^{18}\text{O}$ . It has been suggested that the low-lying states in  $^{16,17,18}\text{O}$  contain sizeable admixtures of highly deformed states [231, 232].

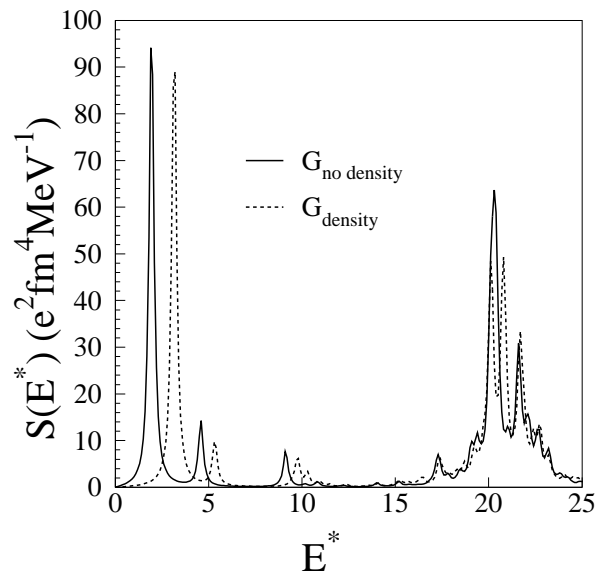


**Figure 34.** Isoscalar quadrupole strength function of  $^{18}\text{O}$  calculated with two types of pairing interaction. See text for description.

By taking into account the mixing between spherical and deformed states, it should be possible to simultaneously reproduce the excitation energies and  $B(E2)$  values of the low-lying states. For heavier oxygen isotopes the deformed states are predicted at higher energies, and thus the mixing is weaker. This explains why the spherical QRPA results for the  $B(E2)$  values in  $^{20,22}\text{O}$  are in much better agreement with experiment. The calculation predicts a decrease in the  $B(E2)$  value in  $^{24}\text{O}$ , and this is due to the effect of the  $2s_{1/2}$  subshell closure.

In nuclei at the neutron drip-line the Fermi level of neutron states is found close to the continuum and, therefore, one expects that continuum effects play an important role also in the calculation of low-lying states. This is illustrated in Fig. 36 where we plot the low-energy portion of the quadrupole response function of  $^{22}\text{O}$ . The two curves correspond to calculations with box boundary conditions, and with the exact treatment of continuum states (cf. Sec. 2). The latter predicts the  $2_1^+$  state at a slightly higher energy, and with a weaker transition strength. In Ref. [30] a continuum QRPA based on the HFB framework in coordinate space has been formulated, and the quadrupole response of the drip-line nucleus  $^{24}\text{O}$  has been described using density-dependent zero-range forces in the particle-hole and particle-particle channels. It has been shown that the low-lying isoscalar quadrupole state is embedded in the neutron continuum, and its excitation energy and strength are very sensitive to the density dependence of pairing correlations.

In order to disentangle the proton and neutron contributions to the  $2_1^+$  excitations, the following reduced matrix elements will be useful:

$$M_p = \langle 2^+ || \sum_{i=1}^Z r_i^2 Y_2(\hat{r}_i) || 0 \rangle,$$

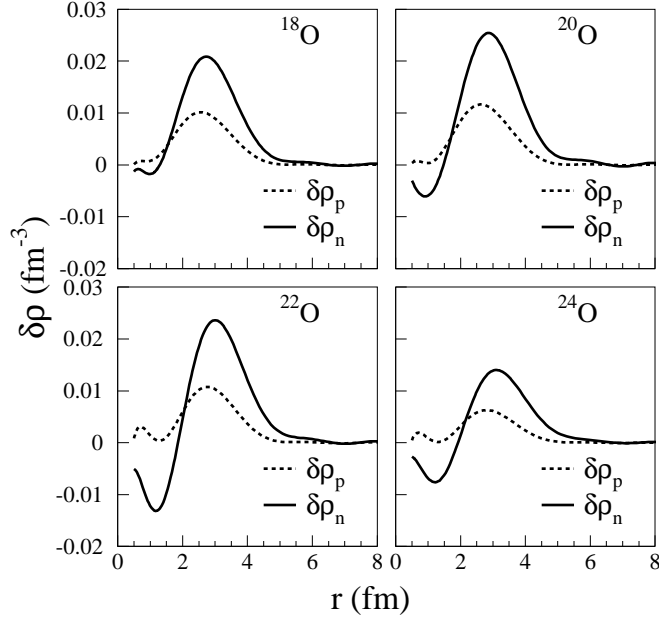


**Figure 35.** Neutron and proton transition densities for the first  $2^+$  state in  $^{18,20,22,24}\text{O}$ .

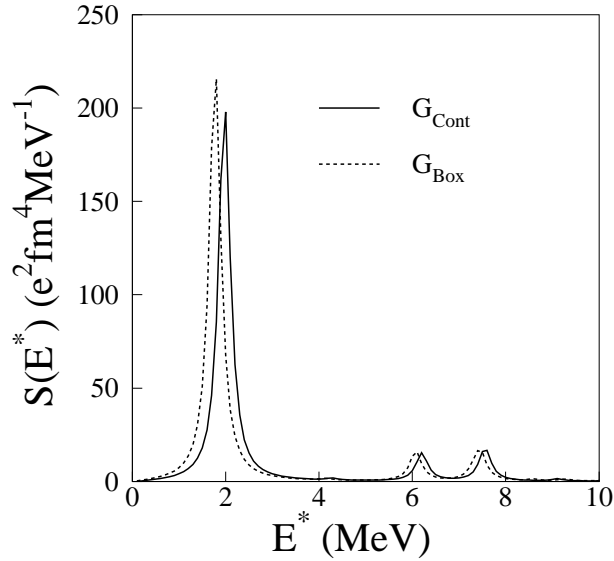


**Figure 36.** Isoscalar quadrupole strength function of  $^{22}\text{O}$ , calculated with the continuum QRPA (solid), and with a box discretization procedure (dashed).

$$M_n = \langle 2^+ || \sum_{i=1}^N r_i^2 Y_2(\hat{r}_i) || 0 \rangle, \quad (82)$$

so that for an electromagnetic probe the  $B(E2)$  is  $\sim M_p^2$ , whereas both  $M_n$  and  $M_p$  contribute in the case of hadron scattering. For instance, experimental evidence for the magicity of the  $N=14$  neutron number in  $^{22}\text{O}$  cannot be conclusive without separating



the proton and neutron contributions to the  $2_1^+$  state. In Ref. [215] the  $B(E2)$  value for  $2_1^+$  was determined by inelastic scattering of  $^{22}\text{O}$  from  $^{197}\text{Au}$  at an energy of 50 MeV/nucleon. The extracted value, however, depends on theoretical predictions for the ratio between  $M_n$  and  $M_p$ , because both Coulomb and nuclear interactions contribute to the reaction.  $M_n$  and  $M_p$  can be separated by means of two experiments which employ different probes. An electromagnetic probe is used to measure the  $B(E2)$  value directly, whereas the second measurement is usually a (p,p') scattering experiment at around 50 MeV/nucleon. This combination allows to determine both  $M_n$  and  $M_p$ , and therefore to probe more directly possible shell closures in exotic nuclei. Angular distributions for elastic and inelastic proton scattering to the  $2_1^+$  state of  $^{22}\text{O}$  have been measured using a secondary radioactive beam [219]. Proton and neutron contributions have been disentangled by a comparison of the (p,p') results with a heavy ion scattering experiment dominated by electromagnetic excitation, and evidence for a strong N=14 shell closure has been found.

In order to compare the QRPA predictions with proton scattering data, microscopic optical potentials can be generated from the HFB and QRPA densities using two different methods: the folding model [233], or the optical model potential (OMP) parameterization using the Jeukenne, Lejeune and Mahaux (JLM) interaction [234]. The folding model analysis uses the CDM3Y6 interaction folded with the HFB densities to generate the isoscalar and isovector parts of the OMP. The spin-orbit potential and the transition potentials are determined by folding the QRPA transition densities with the nucleon-nucleon interaction. The imaginary part of the OMP is generated with the Koning and Delaroche [235] phenomenological parameterization. Cross sections are calculated using DWBA with the ECIS97 [236] code.

The elastic angular distribution is nicely reproduced, even at large angles [219, 227]. Since the  $B(E2)$  can be described by the proton transition density, the neutron transition density is renormalized to reproduce the data. This procedure assumes that the QRPA provides a reliable description of the shape of the transition density for collective states, and provides an empirical value of the  $M_n/M_p$  ratio for the  $2_1^+$  state, deduced from the combination of the electromagnetic and the (p,p') measurements [216]. The resulting  $M_n/M_p$  values are included in Table 3. We note that the value of  $M_n/M_p$  divided by N/Z, is considerably smaller for the first  $2^+$  state of  $^{22}\text{O}$ , compared to  $^{20}\text{O}$ . In  $^{22}\text{O}$  the contributions of protons and neutrons are comparable, because the measured ( $M_n/M_p$ ) ratio is close to N/Z. This is different from  $^{20}\text{O}$ , where the much higher value of  $M_n/M_p$  divided by N/Z shows that neutrons predominantly contribute to the quadrupole excitation. Combined with the high energy of the  $2_1^+$  state in  $^{22}\text{O}$ , these results confirm the N=14 shell closure in neutron-rich oxygen nuclei. The dependence on the potential used to describe the (p,p') angular distributions can be checked by using the complex optical and transition potentials obtained by inserting the calculated ground state and transition densities into the JLM density-dependent optical potential [234]. Renormalizing the neutron transition density to reproduce the inelastic data, the same value of the ratio  $M_n/M_p$  is obtained as with the folding potential. In this way two

reliable optical potentials are used to test the HFB+QRPA matter and transition densities.

A similar study of the  $N=16$  sub-shell closure in  $^{24}\text{O}$  could be performed in a  $^{24}\text{O}(p,p')$  experiment, but this will have to wait for the next generation of radioactive beam facilities. The generality of the method used to microscopically determine the ratio  $M_n/M_p$  from two complementary sets of data, will allow to extend our understanding of neutron-shell closure to regions of heavier nuclei far from stability. An ingenious proton-scattering setup with a liquid hydrogen target and  $\gamma$ -detectors opens the possibility to determine  $M_n/M_p$  in nuclei very far from stability, e.g. in  $^{28}\text{Ne}$  [237].

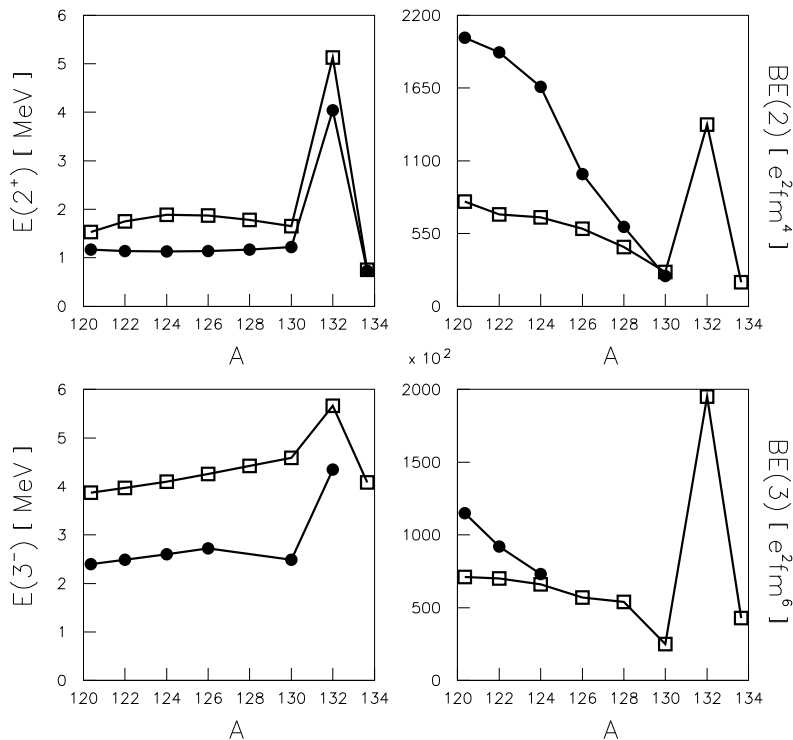


**Figure 37.** The QRPA excitation energies (left panels) and transition strength (right panels) for the  $2_1^+$  and  $3_1^+$  states in the sequence of even-even Sn isotopes (squares) [238], compared with data (circles).

The Skyrme-HFB plus QRPA framework has been applied to the study of low-lying quadrupole states in  $N = 20$  isotones, including the neutron-rich nuclei  $^{32}\text{Mg}$  and  $^{30}\text{Ne}$  [127]. The calculation reproduces both the excitation energies of the first  $2^+$  states and the  $B(E2; 0_1^+ \rightarrow 2_1^+)$  values, and it has been concluded that pairing effects account largely for the anomalous  $B(E2)$  value and the very low excitation energy in  $^{32}\text{Mg}$ .

QRPA calculations for the low-lying  $2^+$  and  $3^-$  states have also been performed for heavier neutron-rich nuclei. For example, the QRPA with Skyrme forces in the  $ph$  channel, and a density-dependent pairing force in the  $pp$  channels, has been employed

in the study of the evolution of the  $2_1^+$  and  $3_1^-$  states along the Sn isotopic chain [238]. The results are shown in Fig. 37, in comparison with experimental data [239], including recent Coulomb excitation measurements of the unstable  $^{126,128,130}\text{Sn}$  isotopes [240]. We notice that the calculation nicely reproduces the excitation energies of the  $2_1^+$  state, but overestimates the experimental energies of the  $3_1^-$  state by more than 50%. On the other hand, the measured  $B(E2)$  values in open shell nuclei are systematically underestimated by large factors with the QRPA model, whereas this discrepancy is less pronounced for the  $B(E3)$  values. The reason for such a large difference between the experimental and calculated  $B(E2)$  values, is that the QRPA does not take into account the anharmonicities of the low-lying quadrupole vibrations, i.e. the  $2_1^+$  is described as a pure 1-phonon state, whereas in this mass region the  $2_1^+$  states contain pronounced admixtures of 2-phonon states which cannot be described in a simple QRPA framework.

In the recent Skyrme-HFB plus QRPA analysis of the  $J^\pi = 0^+$ ,  $1^-$ , and  $2^+$  multipoles for the even Ca, Ni and Sn isotopes from the proton to the neutron drip-lines [120], it has been shown that the strength functions in the  $2^+$  channels are qualitatively different from those in the lower-multipole channels. The low-energy strength grows with the neutron number, but unlike in the  $0^+$  channel, both neutrons and protons contribute to the transitions to these states, even near the drip line, because the isoscalar (IS) peaks are much larger than the isovector (IV) peaks. An interesting result is also that at the neutron drip-line the IS and IV strength functions in Ni and Sn have distinct low-energy peaks, whereas in Ca the peaks coincided. In all nuclei near the neutron drip-line, the states in the low-energy peaks are mostly above the neutron-emission threshold, yet the neutron tails cut off at much smaller radii than do those in the  $0^+$  and  $1^-$  channels. Also the transition densities to the  $2^+$  states are different: they have no real nodes and a proton component that is of the same order as the neutron component. The strong low-energy states near the neutron drip-line have transition densities that resemble those of surface vibrations are often quite collective. The detailed analysis of Ref. [120] has emphasized the complicated relationship among collectivity, strength, and transition density in neutron-rich nuclei.

### 5.3. Giant Quadrupole Resonance and Higher Multipoles

The giant quadrupole resonance (GQR) corresponds to a highly collective oscillation of the neutron and proton density distributions between prolate and oblate ellipsoidal shapes. In the isoscalar mode the proton and neutron densities oscillate in phase, with an empirical excitation energy:  $E_{GQR} \approx 64 \text{ MeV} \cdot A^{-1/3}$  and, in heavy nuclei, this mode typically exhausts 50 to 100 % of the energy weighted sum rule (EWSR) [6]. The isovector GQR is found at much higher excitation energies and, even in heavy nuclei, it is much more fragmented.

In neutron-rich nuclei far from stability one expects that the neutron skin has a pronounced effect on the high-energy quadrupole vibrational mode, however, no data on the GQR in unstable nuclei are available at present. There have also been only few

	$E_{GQR}$ (MeV)	$\Gamma_{FWHM}$ (MeV)
$^{34}\text{Ca}$	17.5	1.6
$^{40}\text{Ca}$	16.2	0.6
$^{48}\text{Ca}$	16.7	0.3
$^{60}\text{Ca}$	14.9	1.3

**Table 4.** Continuum-RPA results for the GQR centroids and widths of Ca isotopes [118]

theoretical studies of giant quadrupole resonances in exotic nuclei. In Refs. [29, 30, 37] the QRPA and RQRPA calculations have been performed for the isoscalar GQR in oxygen isotopes. Since in light systems this mode can be highly fragmented, for a study of the effect of neutron excess on the GQR one should consider heavier nuclei, in which the GQR displays a single peak at energies between 10 and 15 MeV. Such studies have been carried out with the continuum-RPA using Skyrme forces [118], and recently RPA calculations with the Gogny interaction have also been performed [125].

The isospin dependence of the excitation energy and width of the GQR in exotic nuclei is illustrated in Table 4 for the example of  $^{34,40,48,60}\text{Ca}$  [118]. In addition to the systematic lowering of the GQR excitation energies with the increase of the number of neutrons ( $^{48}\text{Ca}$  is an exception, because of the neutron shell closure at  $N = 28$ ), the calculation predicts an enhancement of the low-energy quadrupole strength both in the proton-rich  $^{34}\text{Ca}$ , and neutron-rich  $^{60}\text{Ca}$ . Continuum-RPA calculations predict the escape width of a resonant state, and in Table 4 we notice a pronounced increase of the escape width in the weakly-bound nuclei  $^{34}\text{Ca}$  and  $^{60}\text{Ca}$ . The calculated widths, however, do not contain the spreading contribution, i.e. the width that results from the coupling of the GQR to more complex states like, for instance, two-phonon admixtures. In this sense the widths in Table 4 are not realistic, and only illustrate the effect of the coupling to continuum states. No systematic calculation of the GQR spreading width in exotic nuclei has been reported so far, the only exception is the study of the GQR in  $^{28}\text{O}$  in Ref. [41], which has shown that the spreading width is enhanced with respect to the isotopes close to the stability line.

Giant quadrupole resonances in exotic nuclei have also been calculated with the RPA based on the Gogny interaction [125]. For the doubly-magic  $^{78}\text{Ni}$ ,  $^{132}\text{Sn}$  and  $^{100}\text{Sn}$  the Gogny-RPA results predict GQR excitation energies that are 1 – 1.5 MeV above the empirical relation  $E_{GQR} \approx 64 \text{ MeV} \cdot A^{-1/3}$ . In Ref. [125] RPA-Gogny calculations have also been performed for the isoscalar and isovector octupole strength distributions, and in Fig. 38 we display the isoscalar octupole states in  $^{78}\text{Ni}$ ,  $^{132}\text{Sn}$ ,  $^{100}\text{Sn}$  and  $^{208}\text{Pb}$ . The strength is clearly separated into two regions: the  $3_1^-$  state dominates the low-energy strength, whereas the strong peaks above 20 MeV excitation energy correspond to the High Energy Octupole Resonance (HEOR). The properties of the HEOR in nuclei far from stability ( $^{78}\text{Ni}$ ,  $^{132}\text{Sn}$ ,  $^{100}\text{Sn}$ ) are not significantly different from those in stable nuclei, e.g.  $^{208}\text{Pb}$ , probably because the HEOR corresponds to  $3\hbar\omega$  excitations and

these high-energy configurations may not be very sensitive to changes in the number of neutrons/protons with respect to stable nuclei.

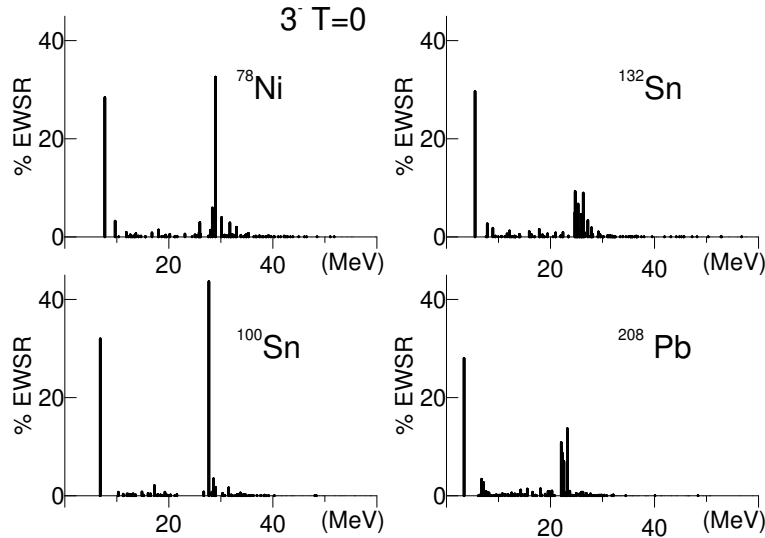


**Figure 38.** Fraction of the EWSR exhausted by the isoscalar octupole states in  $^{78}\text{Ni}$ ,  $^{132}\text{Sn}$ ,  $^{100}\text{Sn}$  and  $^{208}\text{Pb}$  [125].

#### 5.4. Pairing Vibrations in Drip-Line Nuclei

Two-neutron transfer reactions such as  $(t, p)$  or  $(p, t)$  have been used for many years in studies of nuclear pairing correlations [241]. The corresponding pair-transfer modes are usually described in terms of pairing vibrations or pairing rotations [242, 243]. Pairing vibrations are  $L = 0$  modes induced by the addition or removal of a pair of neutrons, and can be associated with the fluctuation of the pairing field  $\hat{\Delta}$  (see Sec. 2.1) around its equilibrium value. Around magic nuclei, such as  $^{208}\text{Pb}$ , the  $J^\pi=0^+$  spectrum generated by the pair-addition  $(c_i^\dagger c_j^\dagger)$  and pair-subtraction  $(c_i c_j)$  operators in Eq. (37), is harmonic and corresponds to the so-called pairing vibration mode, which can be viewed as a vibration in an abstract “gauge” space, instead of the ordinary three-dimensional space in which shape vibrations take place.

In a microscopic approach the collective two neutrons transition can be described in the QRPA framework: the excitation operator of Eq. (37) includes particle-hole, particle-particle and hole-hole excitations. In this case the non-conservation of the particle number, which is implicit in the quasiparticle formalism, can be used as a tool to study particle-violating transitions. The pairing vibrational state reads

$$|A + 2, n\rangle = \left( \sum_{k_F < k < l} X_{kl}^{(n)} c_k^\dagger c_l^\dagger - \sum_{k < l < k_F} Y_{kl}^{(n)} c_l^\dagger c_k^\dagger \right) |A\rangle. \quad (83)$$

High-energy collective pairing modes – Giant Pairing Vibrations (GPV) have been predicted and studied theoretically [241, 243, 244, 245, 246], but have never been observed despite a number of  $(p, t)$  experiments performed in the 70’s and 80’s [241, 243].

The experimental setup for such studies must achieve a proper balance between the low energy of the incident proton beam (below 50 MeV) necessary for the excitation of the  $L = 0$  mode, and the energy which is required to populate the energy region of the GPV. These experiments are therefore rare [247], and the discovery of deep hole-states of non-collective character made the detection of the GPV even harder [248, 249]. Beams of exotic nuclei could provide the solution. Incident beams of a few MeV/nucleon of weakly-bound projectiles (providing high Q-values) could be used to populate the GPV [241] using reactions such as  $({}^6\text{He}, \alpha)$ . However, the intensity of radioactive beams is typically several orders of magnitude lower than that of stable beams, and the background resulting from break-up reactions could be large with weakly-bound projectiles. There is a renewed interest in GPV and improved experimental investigations are currently being planned, both with stable and exotic beams.

Pairing vibrations in exotic nuclei could provide valuable structure information [241, 244, 250], in particular on pairing correlations in systems far from stability and the effects of the coupling to the continuum. Pairing vibrations generally depend on the strength of the pairing interaction between the two transferred neutrons: transfer cross sections are enhanced when the two neutrons form a strongly bound pair. The theoretical analysis of two-nucleon transfer modes in nuclei far from stability is complicated by the effect of continuum coupling. The right tool to study pairing vibrations in exotic nuclei is the continuum-QRPA, because it provides a consistent microscopic treatment of both pairing and continuum effects. The strength function which describes the two-particle transfer from the ground state of a nucleus with  $A$  nucleons to the excited states of a nucleus with  $A+2$  nucleons reads:

$$S(\omega) = -\frac{1}{\pi} \text{Im} \int F^{12*}(\mathbf{r}) \mathbf{G}^{22}(\mathbf{r}, \mathbf{r}'; \omega) F^{12}(\mathbf{r}') d\mathbf{r} d\mathbf{r}' \quad (84)$$

where  $\mathbf{G}^{22}$  denotes the  $(pp, pp)$  component of the Green's function, and  $F^{12}$  is the perturbing external field (see Sec. 2.3).

The strength function for the neutron-pair transfer to  ${}^{22}\text{O}$  is shown in Fig. 39 [250]. The interaction in the  $ph$  channel is Skyrme SLy4, and a zero-range density-dependent pairing interaction is used in the  $pp$  channel. The solid curve denotes the unperturbed strength, which displays peaks characteristic for the addition of two neutrons in specific configurations. The first peak results from the filling of the  $2s_{1/2}$  orbital, and the peak at 10.8 MeV corresponds to the two-neutron  $(1d_{3/2})^2$  quasiparticle configuration. The effect of the residual interaction on the pair transfer mode is seen in the QRPA strength function (dashed curve), and it demonstrates the collective nature of pairing vibrations [243]. Namely, the residual interaction shifts the position of the two-quasiparticle resonant state, located at 10.8 MeV in the unperturbed response, to lower energy and increases its strength. The strong peak at zero-energy corresponds to the pair transfer to the spurious Goldstone mode associated with particle-number fluctuations. The peak at  $\approx 8.6$  MeV represents a neutron-pair transfer predominantly to the  $1d_{3/2}$  states, whereas the broad resonant structure around 16 MeV is built mainly on the neutron resonant state  $1f_{7/2}$ . This broad two-quasiparticle resonance is characteristic

for a giant pairing vibration [244, 245, 246].

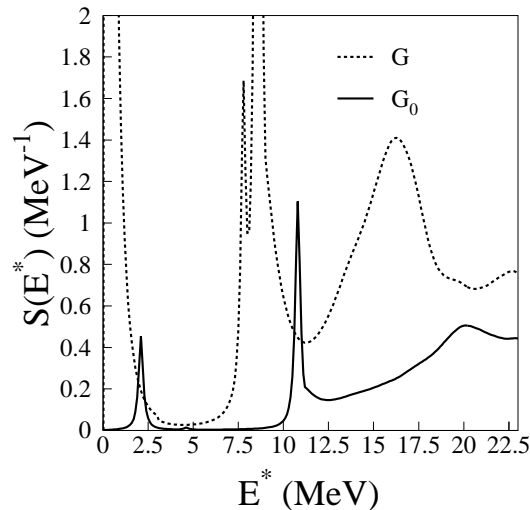


**Figure 39.** The strength function for the two-neutron transfer on  $^{22}\text{O}$ . The solid (dashed) curve corresponds to the unperturbed (QRPA) response.

To compare the results with the measured cross section, one must calculate the nuclear structure form factor, which describes the wave function of the two transferred neutrons, as well as the reaction part which includes the optical potential. For closed-shell nuclei the two-particle transfer modes are described by the particle-particle ( $pp$ ) RPA [251, 252], whereas the QRPA [243, 244] is used for open-shell nuclei. Most of the cross section calculations employ the Distorted Wave Born Approximation (DWBA).

In nuclear response theory the transition from the ground state to the excited state  $|\nu\rangle$  in the same nucleus is described by the transition density

$$\delta\rho^\nu(\mathbf{r}\sigma) = \langle 0|c^\dagger(\mathbf{r}\sigma)c(\mathbf{r}\sigma)|\nu\rangle \quad (85)$$

where  $c^\dagger(\mathbf{r}\sigma)$  is the particle creation operator in coordinate space. The corresponding quantity used in the description of pair transfer processes is the pair transition density defined by

$$\delta\kappa^\nu(\mathbf{r}\sigma) = \langle 0|c(\mathbf{r}\bar{\sigma})c(\mathbf{r}\sigma)|\nu\rangle \quad (86)$$

where the operator  $c^\dagger(\mathbf{r}\bar{\sigma}) = -2\sigma c^\dagger(\mathbf{r} - \sigma)$  creates a particle in the time-reversed state. The pair transition density determines the transition from the ground state of a nucleus with  $A$  nucleons to the state  $|\nu\rangle$  in the nucleus with  $A+2$  nucleons. This quantity is calculated in the QRPA.

The DWBA calculation of the cross section for the two-neutron transfer requires the form factor which describes the correlation between the two neutrons and the initial nucleus [253]. Calculations based on the continuum-QRPA include effects of both pairing correlations and continuum coupling. The calculation of the form factor and cross section will be illustrated for the transfer reaction  $^{22}\text{O}(t,p)$ . The DWBA cross section is calculated for the  $^{22}\text{O}+t$  Bechetti and Greenlees optical potential [254] in the

entrance channel, and the  $^{22}\text{O}+p$  Becchetti and Greenlees [255] in the exit channel. The calculation is performed in the zero-range approximation, in which the two-neutrons and the residual fragment are located at the same point in space, and therefore the range function is determined by a simple constant  $D_0$  [253]. The zero-range approximation provides a satisfactory description of the shape of the angular distribution [243, 253, 256], but its magnitude is generally underestimated. The form factor for the pair transfer is obtained by folding the pair transition density  $\delta\kappa''$  (Eq. (86)) with the interaction acting between the transferred pair and the residual fragment [241]. In the zero-range approximation one uses the  $\delta$ -force for this interaction, and therefore the form factor coincides with the pair transition density (86) [253]. In order to illustrate the effect of the continuum on the form factor, the (t,p) angular distribution for the mode at  $\approx 8.6$  MeV (see Fig. 39) is calculated using both box boundary conditions and with the exact treatment of the continuum. The resulting two-neutron transfer cross sections are shown in Fig. 40, and we notice a pronounced effect of the continuum in the diffraction minima.

The continuum-QRPA could be used in the analysis of the forthcoming data on the GPV, obtained with beams of exotic nuclei at around 5 MeV/nucleon. Preliminary calculations [244] have shown that  $(^6\text{He},\alpha)$  reactions can excite the GPV with a cross section of the order of few millibarns, whereas this mode is not excited in  $(^{14}\text{C},^{12}\text{C})$  reactions.

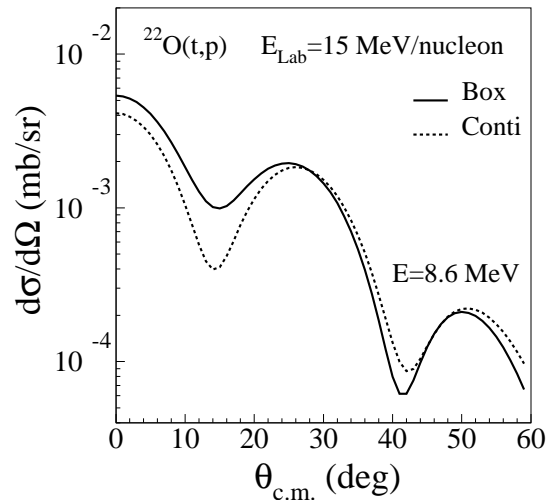


**Figure 40.** Two-neutron transfer cross section on  $^{22}\text{O}$ , for the state at  $\approx 8.6$  MeV. The solid (dashed) curve corresponds to the QRPA result obtained with the box (exact) boundary conditions.



## 6. Charge-exchange Resonances

### 6.1. Proton-Neutron QRPA

Starting from the ground-state of the  $(N,Z)$  nuclear system, charge-exchange excitations induced by isospin lowering  $\tau_-$  and raising  $\tau_+$  operators correspond to transitions to final states in the neighboring  $(N\mp 1, Z\pm 1)$  nuclei, respectively. These transitions can occur either spontaneously in  $\beta$ -decay, or they can be induced in charge-exchange reactions, e.g.  $(p, n)$  or  $({}^3\text{He}, t)$  in the  $\tau_-$  case, when the final state lies outside the  $\beta$ -decay energy window. Charge-exchange resonances in stable nuclei have been the subject of numerous experimental and theoretical studies (see, for instance, Ref. [6]). However, a systematic experimental information on these resonances is still missing, mainly because of the absence of selective probes. For instance, there is very little data on the charge-exchange dipole resonance and, despite considerable experimental effort, the charge-exchange monopole mode has not yet been observed. This resonance is particularly interesting, because its excitation energies could provide useful information on the isospin mixing in nuclear ground-states, the symmetry term of the nuclear equation of state, and the isovector terms in effective nucleon-nucleon interactions. Charge-exchange transitions are important for weak-interaction processes in nuclei, in particular charged current processes in nuclear astrophysics and neutrino physics. These include the  $\beta$ -decay of nuclei that lie on the  $r$ -process path of stellar nucleosynthesis, and neutrino-nucleus scattering.

The only exception are the Isobaric Analog Resonance (IAR) and the Gamow-Teller Resonance (GTR), for which rather detailed experimental information has become available in several mass-regions. They are induced by the following transition operators

$$\hat{F}_{IAR} = \sum_{i=1}^A \tau_-(i), \quad (87)$$

and

$$\hat{F}_{GTR} = \sum_{i=1}^A \sigma(i)\tau_-(i), \quad (88)$$

respectively. Since these are  $L = 0$  modes, they can be selectively excited by using zero-degree charge-exchange reactions, like  $(p, n)$  or  $({}^3\text{He}, t)$ . When the incident projectile energy is increased, the excitation of the GTR is favored over the IAR. A comprehensive review of the properties of the IAR and GTR in stable nuclei can be found in Ref. [257].

Charge-exchange resonances in exotic nuclei are virtually unexplored. The experimental investigation of these modes in nuclei far from stability will become possible with the new generation of radioactive-beam facilities. So far, experimental studies have been restricted to the states which are accessible in  $\beta$ -decay. In neutron-rich nuclei, for example, the neutron Fermi level is located at much higher energy than the proton valence states, and the  $\beta^-$ -decay becomes progressively much faster. In proton-rich nuclei the same happens for the  $\beta^+$ -decay. Closer to the nucleon drip-lines more and

more single-nucleon states enter the  $\beta$ -decay energy window, and the experiment probes most of the charge-exchange strength. The importance of this phenomenon for the understanding of the isospin properties of nuclei has been first pointed out in Ref. [258], where the HF-RPA has been employed in the study of charge-exchange transitions in weakly-bound systems.

The extension of the Skyrme-RPA model to the charge-exchange channel [259], has been used in calculations of the response to different operators [260]. The discrete RPA has also been employed in studies of charge-exchange modes. In addition, the formalism of the coupling of  $p - h$  configurations to more complex states of  $2p - 2h$  character, has been developed in Refs. [54, 261, 262]. In the case of open-shell nuclei, most of the charge-exchange QRPA calculations have used simple separable forces as the  $ph$  and  $pp$  residual interactions. The same functional form has been used in both channels, with two different strength parameters  $g_{ph}$  and  $g_{pp}$ , as in the pioneering work of Ref. [263] where the formalism has been developed for the first time. More recently, the PN-QRPA based on Skyrme forces in the  $ph$  channel, with a simplified residual interaction of a separable form, and with the BCS treatment of the  $pp$  channel, has also been extended to the description of deformed nuclei.  $\beta$ -decay rates in different isotopic chains have been studied [264, 265, 266, 267], in order to determine to what extent the intrinsic deformation influences  $\beta$ -decay properties, and whether the decay spectra differentiate between spherical, prolate and oblate shapes. Medium-heavy nuclei like Kr, Sr have been studied, as well as heavier systems e.g. Hg, Pb and Po [268]. It has been shown that prolate and oblate deformations lead to significantly different Gamow-Teller spectra, but in many cases these signatures of the intrinsic deformation are not too sensitive to the choice of the Skyrme force used in the calculation.

The path of the  $r$ -process nucleosynthesis is governed by delicate balance between neutron-capture reactions and  $\beta$ -decay rates. This has motivated the calculation of the GT  $\beta$ -decay of the so-called “waiting-point” nuclei in Ref. [31], which was also the first attempt to perform a self-consistent PN-QRPA analysis based on the HFB treatment of the nuclear ground state. A Skyrme interaction and a zero-range pairing interaction were used in the mean-field and pairing channels, respectively. The associated QRPA equations were solved in the canonical basis, in which they read as in Eq. (55), with the matrices  $A$  and  $B$  given by:

$$\begin{aligned}
A_{pn,p'n'}^J &= H_{pp'}^{11} \delta_{nn'} + H_{nn'}^{11} \delta_{pp'} \\
&\quad + (u_p v_n u_{p'} v_{n'} + v_p u_n v_{p'} u_{n'}) V_{pn'n_p'}^{phJ} \\
&\quad + (u_p u_n u_{p'} u_{n'} + v_p v_n v_{p'} v_{n'}) V_{pn_p'n'}^{ppJ} \\
B_{pn,p'n'}^J &= (-1)^{j_{p'} - j_{n'} + J} (u_p v_n v_{p'} u_{n'} + v_p u_n u_{p'} v_{n'}) V_{pp'nn'}^{phJ} \\
&\quad - (u_p u_n v_{p'} v_{n'} + v_p v_n u_{p'} u_{n'}) V_{pp_p'n'}^{ppJ} .
\end{aligned} \tag{89}$$

Here  $p$ ,  $p'$ , and  $n$ ,  $n'$  denote proton and neutron canonical states, respectively,  $V^{ph}$  is the proton-neutron  $ph$  residual interaction, and  $V^{pp}$  is the corresponding  $pp$  interaction. Since the canonical basis does not diagonalize the mean-field Hamiltonian  $\hat{h}$ , nor the

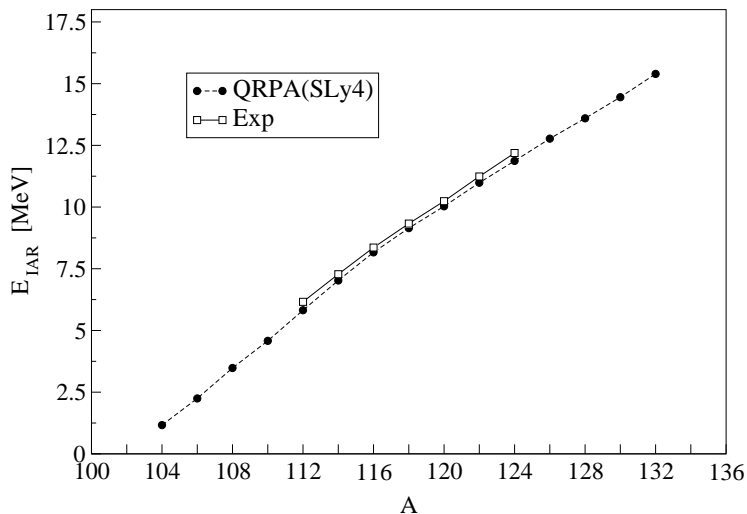


**Figure 41.** IAR excitation energy in the sequence of Sn isotopes. The results from the fully self-consistent Skyrme QRPA calculation are compared with the experimental excitation energies [271].

pairing field  $\hat{\Delta}$ , the non-diagonal matrix elements  $H_{nn'}^{11}$  and  $H_{pp}^{11}$  appear in the matrix  $A$ :

$$H_{\kappa\kappa'}^{11} = (u_{\kappa}u_{\kappa'} - v_{\kappa}v_{\kappa'})h_{\kappa\kappa'} - (u_{\kappa}v_{\kappa'} + v_{\kappa}u_{\kappa'})\Delta_{\kappa\kappa'} . \quad (90)$$

The PN-QRPA calculation of Ref. [31] has shown that the excited  $1^+$  states and  $\beta$ -decay half-lives are very sensitive to the  $T = 0$  component of the residual  $pp$  interaction. Since the  $T = 0$  pairing is not manifest in the ground states of nuclei with  $N$  different from  $Z$ , it has to be introduced in the PN-QRPA independently from the  $T = 1$  channel, and this of course breaks the self-consistency of the calculation. In particular, a finite-range interaction with adjustable parameters has been employed, and the overall strength was tuned to reproduce some selected experimental  $\beta$ -decay half-lives. The same approach has been used in Ref. [269] to analyze properties of GT resonances predicted by several Skyrme parameterizations, in correlation with the corresponding values of the Landau parameters in infinite nuclear matter.

Very recently a fully self-consistent non-relativistic charge-exchange QRPA has been developed and tested in the description of IAR [270]. In this case only the  $T = 1$  component of the residual pairing interaction contributes and, because of isospin invariance, its strength must be identical to that used for the calculation of HF-BCS ground-state. In Fig. 41 we show the excitation energies of IAR of Sn isotopes, calculated with the PN-QRPA based on the Skyrme interaction SLy4 and compared with the experimental values. We notice a very good agreement with data, and this shows that the model can be systematically employed in calculation of charge-exchange processes in stable and exotic open-shell nuclei.

### 6.2. Proton-Neutron Relativistic QRPA

In the relativistic mean-field framework the spin-isospin dependent interaction terms are generated by the  $\rho$ - and  $\pi$ -meson exchange. Because of parity conservation, the one-pion direct contribution vanishes in the mean-field calculation of a nuclear ground state. Its inclusion is important, however, in calculations of excitations that involve spin and isospin degrees of freedom. The particle-hole residual interaction in the PN-RQRPA is derived from the Lagrangian density

$$\mathcal{L}_{\pi+\rho} = -g_\rho \bar{\psi} \gamma^\mu \vec{\rho}_\mu \vec{\tau} \psi - \frac{f_\pi}{m_\pi} \bar{\psi} \gamma_5 \gamma^\mu \partial_\mu \vec{\pi} \vec{\tau} \psi . \quad (91)$$

In Ref. [272] the proton-neutron relativistic quasiparticle RPA (PN-RQRPA) has been formulated in the canonical single-nucleon basis of the time-dependent RHB model, and applied in studies of charge-exchange excitations in open shell nuclei. The spin-isospin dependent residual two-body interaction in the particle-hole channel reads

$$\begin{aligned} V(\mathbf{r}_1, \mathbf{r}_2) = & \vec{\tau}_1 \vec{\tau}_2 (\beta \gamma^\mu)_1 (\beta \gamma_\mu)_2 g_\rho^2 D_\rho(\mathbf{r}_1, \mathbf{r}_2) \\ & - \left( \frac{f_\pi}{m_\pi} \right)^2 \vec{\tau}_1 \vec{\tau}_2 (\boldsymbol{\Sigma}_1 \nabla_1) (\boldsymbol{\Sigma}_2 \nabla_2) D_\pi(\mathbf{r}_1, \mathbf{r}_2) , \end{aligned} \quad (92)$$

where  $D_{\rho(\pi)}$  denotes the meson propagator

$$D_{\rho(\pi)}(\mathbf{r}_1, \mathbf{r}_2) = \frac{1}{4\pi} \frac{e^{-m_{\rho(\pi)}|\mathbf{r}_1 - \mathbf{r}_2|}}{|\mathbf{r}_1 - \mathbf{r}_2|} , \quad (93)$$

and

$$\boldsymbol{\Sigma} = \begin{pmatrix} \sigma & 0 \\ 0 & \sigma \end{pmatrix} . \quad (94)$$

Transitions between the  $0^+$  ground state of a spherical even-even parent nucleus, and the state with angular momentum and parity  $J^\pi$  of the odd-odd daughter nucleus are considered. With respect to the RHB calculation of the ground state of the even-even nucleus, the charge-exchange channel includes the additional one-pion exchange contribution. For the pseudovector pion-nucleon coupling the standard values:  $m_\pi = 138.0$  MeV, and  $f_{\pi NN}^2/4\pi = 0.08$ , are used. The derivative type of the pion-nucleon coupling necessitates the inclusion of the zero-range Landau-Migdal term, which accounts for the contact part of the nucleon-nucleon interaction

$$V_{\delta\pi}(\vec{r}_1, \vec{r}_2) = g' \left( \frac{f_\pi}{m_\pi} \right)^2 \vec{\tau}_1 \vec{\tau}_2 \vec{\Sigma}_1 \cdot \vec{\Sigma}_2 \delta(\vec{r}_1 - \vec{r}_2) , \quad (95)$$

with the parameter  $g' \approx 0.6$  usually adjusted to reproduce data on excitation energies of Gamow-Teller resonances [272, 273, 274]. In the non-relativistic limit the corresponding two-body interaction reduces to the familiar form  $G'_0 \sigma_1 \vec{\tau}_1 \cdot \sigma_2 \vec{\tau}_2$ . We note that a  $ph$  residual interaction based on  $\rho$ - and  $\pi$ -meson exchange has also been used in a number of non-relativistic RPA studies of charge-exchange excitations [275, 276, 277].

In the particle-particle channel of the PN-RQRPA equations both the  $T = 1$  and  $T = 0$  pairing interactions contribute. In Ref. [272] the finite-range Gogny force with

the parameter set D1S [13] has been used in the  $T = 1$  channel, both in the RHB calculation of the ground state of the even-even system and as the PN-RQRPA  $pp$  residual interaction. For the  $T = 0$  proton-neutron pairing force a similar interaction has been employed: a short-range repulsive Gaussian combined with a weaker long-range attractive Gaussian

$$V_{12} = -V_0 \sum_{j=1}^2 g_j e^{-r_{12}^2/\mu_j^2} \hat{\Pi}_{S=1,T=0} \quad , \quad (96)$$

where  $\hat{\Pi}_{S=1,T=0}$  projects onto states with  $S = 1$  and  $T = 0$ . This interaction was also used in the non-relativistic QRPA calculation of  $\beta$ -decay rates for spherical neutron-rich  $r$ -process waiting-point nuclei [31]. The ranges of the two Gaussians  $\mu_1=1.2$  fm and  $\mu_2=0.7$  fm are taken from the Gogny interaction Eq. (13), and the choice of the relative strengths:  $g_1 = 1$  and  $g_2 = -2$  makes the force repulsive at small distances. The overall strength parameter  $V_0$  can be adjusted, for instance, to experimental  $\beta$ -decay half-lives [31, 278].

The two-quasiparticle PN-RQRPA configuration space includes states with both nucleons in the discrete bound levels, states with one nucleon in the bound levels and one nucleon in the continuum, and also states with both nucleons in the continuum. In addition to configurations built from two-quasiparticle states of positive energy, the RQRPA configuration space contains pair-configurations formed from the fully or partially occupied states of positive energy and the empty negative-energy states from the Dirac sea. The inclusion of configurations built from occupied positive-energy states and empty negative-energy states is essential for the consistency of the relativistic (proton-neutron) QRPA (current conservation, decoupling of spurious states, sum rules). The PN-RQRPA model is fully consistent: the same interactions, both in the  $ph$  and  $pp$  channels, are used in the RHB equation that determines the canonical quasiparticle basis, and in the PN-RQRPA equation. In both channels the same strength parameters of the interactions are used in the RHB and RQRPA calculations.

### 6.3. Gamow-Teller Resonances

Collective spin and isospin excitations in atomic nuclei have been the subject of many experimental and theoretical studies (for an extensive review see Ref. [257]). Nucleons with spin up and spin down can oscillate either in phase (spin scalar  $S = 0$  mode) or out of phase (spin vector  $S = 1$  mode). The spin vector, or spin-flip excitations can be of isoscalar ( $S = 1, T = 0$ ) or isovector ( $S = 1, T = 1$ ) nature. These collective modes provide direct information on the spin and spin-isospin dependence of the effective nuclear interaction.

The Gamow-Teller resonance represents a fundamental charge-exchange mode and corresponds to a collective spin-isospin state  $J^\pi = 1^+$  formed when the excess neutrons coherently change the direction of their spin and isospin without changing their orbital motion. This collective mode was predicted already in 1963 [279], but it was only in 1975 that the first experimental indications of the GT resonance were observed in

$(p, n)$  charge-exchange reactions at intermediate energies [280]. More recently, advanced experiments with  $(^3\text{He}, t)$  reactions have achieved very good energy ( $\Delta E \approx 50$  keV) and angular ( $\Delta\Theta \approx 0.3^\circ$ ) resolution [281], allowing not only the detection of the fine structure of GT transitions [282], but also studies of GT strength in exotic proton-rich nuclei [283]. The detailed knowledge of GT strength distributions in regions away from the valley of  $\beta$ -stability is essential for an understanding of nuclear processes relevant for nucleosynthesis. In particular, the low-lying GT strength is directly related to  $\beta$ -decay rates, as well as to the electron-capture process leading to the stellar collapse and supernovae explosion. At present, however, very little is known about charge-exchange excitations in exotic nuclei, and the modeling of nuclear weak-interaction processes in stars must rely on theoretical predictions of the GT strength distributions.

Recent theoretical studies of Gamow-Teller excitations and  $\beta$ -decay rates have been based on: (i) the shell-model approach, (ii) the non-relativistic proton-neutron (Q)RPA, and (iii) the relativistic proton-neutron (Q)RPA. Data on charge-exchange excitations in light and medium-mass nuclei are very successfully reproduced by large-scale shell-model calculations [284]. However, as the number of valence nucleons increases, the dimension of shell-model configuration space becomes far too large for any practical calculation. Present shell-model calculations are thus restricted up to the region of  $pf$ -shell nuclei with  $A = 45 - 65$  [285]. Both the  $\text{GT}^-$  and  $\text{GT}^+$  response, as well as  $\beta$ -decay rates in medium-mass nuclei have been successfully described by shell-model Monte Carlo calculations (SMMC) [286, 287]. Studies of charge-exchange excitations have only recently been reported in the relativistic mean-field plus RPA framework. These include the relativistic RPA analysis of isobaric analog states and Gamow-Teller resonances (GTR) in the doubly closed-shell nuclei  $^{48}\text{Ca}$ ,  $^{90}\text{Zr}$ , and  $^{208}\text{Pb}$  [273, 288], performed in a restricted configuration space that did not include negative-energy states from the Dirac sea. Although these configurations do not affect the excitation energies of the charge-exchange modes, they have a pronounced effect on the Gamow-Teller sum rule [272, 289]. GT resonances in doubly closed shell nuclei have also been studied with the relativistic RPA in the response function formalism [274].

The PN-QRPA can be employed in calculations of charge-exchange excitations in mass regions that are presently beyond the reach of the most advanced shell-model codes, both in stable and exotic nuclei [290]. Most QRPA studies of the GTR have been based on Skyrme effective interactions with BCS-type pairing [54, 258, 269, 291, 292, 293]. It has been shown that the choice of the spin-isospin terms of the Skyrme energy functional affects the calculated strength distribution and excitation energy of the GT resonance, i.e., the properties of the GTR are not entirely determined by the Landau-Migdal residual interaction [269]. In addition, the inclusion of particle-particle correlations in the QRPA residual interaction is important in calculations of the GT transition strength [294, 295, 296],  $\beta$ -decay rates [31, 297, 298] and double  $\beta$ -decay amplitudes [299, 300]. The inclusion of proton-neutron pairing changes significantly the rates of the neutrinoless double  $\beta$ -decay, allowing for larger values of the expectation value of light neutrino masses [301]. Both the two-neutrino and neutrinoless double

$\beta$ -decay matrix elements are suppressed by the particle-particle interaction [295]. The importance of including proton-neutron pairing in calculations of GT excitations has also been illustrated in relativistic QRPA studies [272]. Pairing correlations have recently also been included in the proton-neutron continuum QRPA based on a phenomenological mean-field potential and the isovector part of the Landau-Migdal  $ph$  interaction [302]. In addition to pairing, deformation plays an important role in the description of  $GT^\pm$  transitions in many nuclei [266, 303]. The sensitivity of GT strength distributions and double  $\beta$ -decay matrix elements to the deformed mean-field has recently been analyzed with the QRPA [304], and it has been shown that nuclear deformation could result in a suppression of two-neutrino double  $\beta$ -decay rates.

The GT resonance represents a coherent superposition of high-lying  $J^\pi = 1^+$  proton-particle – neutron-hole configurations. In the relativistic formalism the GT operator reads

$$Q_{\beta^\pm}^{GT} = \sum_{i=1}^A \Sigma \tau_\pm, \quad (97)$$

where  $\Sigma$  is defined in Eq. (94). In Fig. 42 we display the  $GT^-$  strength distributions in the magic nuclei  $^{48}\text{Ca}$ ,  $^{90}\text{Zr}$ , and  $^{208}\text{Pb}$ , calculated in the PN-RRPA with the DD-ME2 effective interaction and, for comparison, data on the excitation energies of the GTR are also included in the figure. In addition to the high-energy GT resonance – a collective superposition of direct spin-flip ( $j = l + \frac{1}{2} \rightarrow j = l - \frac{1}{2}$ ) transitions, the response functions display a concentration of strength in the low-energy tail. The low-lying GT excitations correspond to core-polarization ( $j = l \pm \frac{1}{2} \rightarrow j = l \pm \frac{1}{2}$ ), and back spin-flip ( $j = l - \frac{1}{2} \rightarrow j = l + \frac{1}{2}$ ) neutron-hole – proton-particle transitions. The strength parameter of the zero-range Landau-Migdal force Eq. (95) has been adjusted to reproduce the GTR excitation energy in  $^{208}\text{Pb}$  ( $g' = 0.52$ ), but we notice a very good agreement with data also for  $^{48}\text{Ca}$  and  $^{90}\text{Zr}$ . The adjusted value of  $g'$  in general depends on the choice of the effective interaction. By employing a set of RMF effective interactions with density-dependent meson-nucleon couplings [35], in Ref. [272] it has been shown that there is a linear correlation between the value of the nuclear asymmetry energy at saturation  $a_4$ , and the value of  $g'$  adjusted to reproduce the GTR excitation energies: effective interactions with higher values of  $a_4$  require higher values of  $g'$ .

As an example of Gamow-Teller resonances in open shell nuclei, in Fig. 43 we plot the PN-RQRPA strength distributions for the  $^{112,118,124,130}\text{Sn}$  target nuclei, in comparison with the data for the centroids of the high-energy direct spin-flip strength, obtained in the  $\text{Sn}(^3\text{He},t)\text{Sb}$  charge-exchange reactions [271]. Direct spin-flip transitions dominate the high-energy region above 10 MeV. The low-energy tail of the strength distribution corresponds to core-polarization, and back spin-flip transitions. The solid curves have been calculated without including the  $T = 0$  proton-neutron pairing in the RQRPA residual interaction. The resulting high-energy GT strength in  $^{118}\text{Sn}$  and  $^{124}\text{Sn}$  is divided into two main components, because of the splitting between different  $ph$  configurations. GTR configuration splitting (an appearance of two or more collective

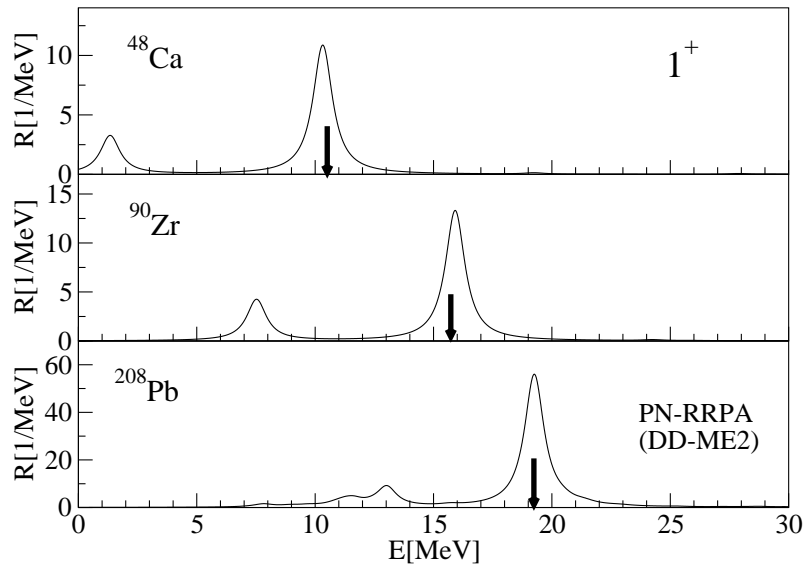


**Figure 42.** Gamow-Teller strength distributions for  $^{48}\text{Ca}$ ,  $^{90}\text{Zr}$ , and  $^{208}\text{Pb}$ . PN-RRPA results are shown in comparison with experimental data (arrows) for the GTR excitation energies in  $^{48}\text{Ca}$  [305],  $^{90}\text{Zr}$  [306, 307], and  $^{208}\text{Pb}$  [102, 308, 309].

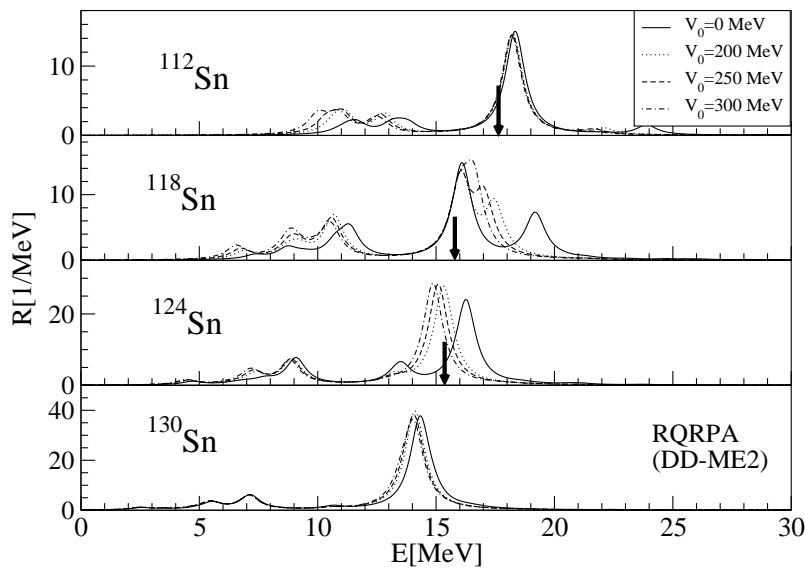


**Figure 43.** The  $\text{GT}^-$  strength distribution in  $^{112,118,124,130}\text{Sn}$ , calculated for different values of the strength parameter  $V_0$  of the  $T = 0$  pairing interaction Eq. (96). The experimental excitation energies of the GTR are denoted by arrows [271].



bumps with comparable intensities in the GTR strength function) was investigated in Ref. [310] in the framework of the shell optical model. For Sn nuclei, in particular, this effect was predicted to occur as the valence neutron start to occupy the level with the highest  $j$  in the shell:  $h_{11/2}$ . The configuration splitting was attributed to the fact that the unperturbed energies of the  $(1g_{7/2}^\pi)(1g_{9/2}^\nu)^{-1}$  and  $(1h_{9/2}^\pi)(1h_{11/2}^\nu)^{-1}$  configurations are almost degenerate. The residual interaction removes this degeneracy and, as a result, the main GT component separates in two distinct peaks. The ground-state pairing correlations have a strong influence on the occupation of the  $1h_{11/2}^\nu$  level, and therefore the energy spacing between the two peaks will depend on  $T = 1$  pairing. For  $^{118}\text{Sn}$  the calculated energy splitting of the GTR was 2.6 MeV [310]. Subsequently, the fragmentation and splitting of the GTR in Sn nuclei was experimentally investigated in Ref. [271]. The theoretically predicted configuration splitting of the main GT component could not be observed, however, because the total widths of the resonances  $\approx 5 - 6$  MeV exceed the predicted splitting. The splitting of the main GT component shown in Fig. 43 (solid line) of  $\approx 3$  MeV is in agreement with the result of Ref. [310].

The other curves shown in Fig. 43 (dotted, dashed and dot-dashed) have been calculated for different values of the strength-parameter of the  $T = 0$  proton-neutron pairing interaction in Eq. (96):  $V_0 = 200, 250,$  and  $300$  MeV. In Ref. [31] the overall strength parameter  $V_0$  of the interaction was adjusted to the measured half-lives of neutron-rich nuclei in regions where the  $r$ -process nucleosynthesis path comes closest to the valley of stability:  $V_0 = 230$  MeV near  $N = 50$ , and  $V_0 = 170$  MeV in the  $N = 82$  region. In our illustrative calculation of Sn nuclei the inclusion of the  $T = 0$  pairing has a strong influence on the low-energy tail of the GT distribution in  $^{112,118,124}\text{Sn}$ , and the configuration splitting between the two high-energy peaks in  $^{118}\text{Sn}$  and  $^{124}\text{Sn}$  disappears. This happens because the  $T = 0$  pairing interaction does not affect configurations based on the  $(1g_{9/2}^\nu)$  orbital (fully occupied), whereas it lowers configurations based on  $(1h_{11/2}^\nu)$  and  $(2d_{5/2}^\nu)$  (partially occupied). This calculation therefore demonstrates that the  $T = 0$  proton-neutron pairing strongly reduces the predicted configuration splitting of the main high-energy GT component. In addition to the main GTR which decreases in energy with increasing mass number, part of the strength associated with direct spin-flip transitions is concentrated at  $\approx 10$  MeV in  $^{112}\text{Sn}$  and  $^{118}\text{Sn}$ . In Ref. [272] it has been shown that the centroid of the GT strength composed of direct spin-flip transitions practically does not depend on the strength of the  $T = 0$  proton-neutron  $pp$  residual interaction.

The structure and evolution of the low-energy tail of the GT distribution determines the  $\beta$ -decay rates of very neutron-rich nuclei, and thus sets the time scale of the  $r$ -process nucleosynthesis. Since the vast majority of nuclides which lie on the path of the  $r$ -process are out of experimental reach, nuclear structure models must be developed that can provide predictions of weak-interaction rates of thousands of nuclei with large neutron to proton asymmetry. Two microscopic approaches can be employed in large-scale calculations of  $\beta$ -decay rates: the interacting shell model and the QRPA. The advantage of using the shell model is the ability to take into account the detailed structure of the

$\beta$ -strength function [311], whereas the QRPA approach is based on global effective interactions and provides a systematic description of  $\beta$ -decay properties of arbitrarily heavy nuclei along the  $r$ -process path. In a recent review of modern QRPA calculations of  $\beta$ -decay rates for astrophysical applications [312], the importance of performing calculations based on self-consistent mean-field models has been emphasized, rather than on empirical mean-field potentials, e.g. the Woods-Saxon potential. In a self-consistent framework both the nuclear ground states, i.e. the masses which determine the possible  $r$ -process path, and the corresponding  $\beta$ -decay properties are calculated from the same energy density functional or effective nuclear interaction. This approach ensures the consistency of the nuclear structure input for astrophysical modeling, and allows reliable extrapolations of the nuclear spin-isospin response to regions of very neutron-rich nuclei.

#### 6.4. Effect of the Dirac Sea on the Gamow-Teller Sum Rule

In nuclei all over the periodic table the GT strength distribution, when measured in the excitation energy region where the most pronounced GT peaks occur, is quenched by more than 20% with respect to the model independent Ikeda sum rule [279]

$$(S_{\beta^-}^{GT} - S_{\beta^+}^{GT}) = 3(N - Z), \quad (98)$$

where  $S_{\beta^\pm}^{GT}$  denotes the total sum of Gamow-Teller strength for the  $\beta^\pm$  transition. In the early  $(p, n)$  studies, for instance, only  $\approx 60\%$  of the sum rule was observed [313]. Two physically different mechanisms had been suggested as a possible explanation of the quenching of the total GTR strength: (i) nuclear configuration mixing – the high-lying  $2p - 2h$  states mix with the  $1p - 1h$  GT states and shift the GT strength to high-energy region far beyond the resonance [314, 315, 316]; (ii) excitation of a nucleon into the high-energy  $\Delta$ -isobar [317, 318], with the  $\Delta$ -isobar – nucleon-hole configurations ( $\Delta - h$ ) coupling to the GT mode and removing part of the strength from the low-lying excitation spectrum [319, 320]. In more recent  $(p, n)$  scattering experiments data on GT strength in the high energy region up to 50 MeV became available [307, 321]. It has been shown that the measured GT strength exhausts 88% and 84% of Ikeda sum rule in  $^{90}\text{Nb}$  and  $^{27}\text{Si}$ , respectively. Most of the GT strength missing in early experimental studies is, therefore, recovered in the energy region where the multiconfiguration spreading mechanism is effective, and only a small fraction of the GT quenching may have its origin in  $\Delta - h$  transitions lying high above the ordinary  $ph$  excitations.

When the Gamow-Teller strength is calculated in the relativistic RPA framework, the total GT strength in the nucleon sector is reduced by  $\approx 12\%$  in nuclear matter, and by  $\approx 6\%$  in finite nuclei, as compared to the Ikeda sum rule [272, 274, 289, 322, 323, 324]. This reduction has been attributed to the effect of Dirac sea negative-energy states, i.e. the missing part of the sum rule is taken by particle-hole excitations formed from ground-state configurations of occupied states in the Fermi sea and empty negative-energy states in the Dirac sea. The effect is illustrated in Fig. 44, where we display the running sum of GTR strength relative to the Ikeda sum rule for  $^{90}\text{Zr}$ ,  $^{132}\text{Sn}$ , and  $^{208}\text{Pb}$ ,

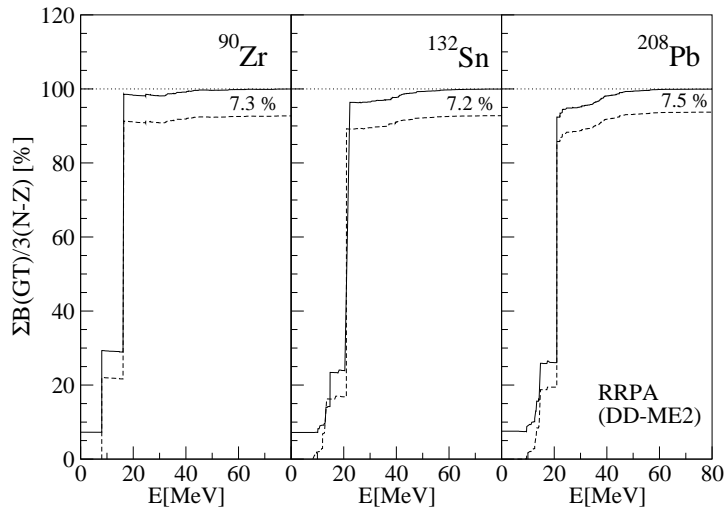


**Figure 44.** The running sum of the GTR strength for  $^{90}\text{Zr}$ ,  $^{132}\text{Sn}$ , and  $^{208}\text{Pb}$ . The dashed lines corresponds to PN-RRPA calculations with only positive-energy  $ph$  configurations. For the calculation denoted by the solid lines the RRPA space includes configurations formed from occupied states in the Fermi sea and empty negative-energy states in the Dirac sea. The total sum of the GT strength is compared to the model independent Ikeda sum rule (dotted lines).

evaluated in the PN-RRPA with the DD-ME2 effective interaction. The horizontal dotted lines denote the value  $3(N - Z)$  of the Ikeda sum rule. The solid and dashed lines correspond to the values of the GTR sum calculated from  $-\infty$  to the excitation energy denoted on the abscissa. The big jump in the calculated GTR sum occurs, of course, when the main GTR peak is included. The PN-RRPA calculation represented by the dashed lines includes only positive energy  $ph$  configurations. Even by extending the sum up to 80 MeV, the total sum is reduced  $\approx 7-8\%$  with respect to the Ikeda sum rule. The Ikeda sum rule is completely exhausted by the calculated GT strength only when the relativistic RPA/QRPA space includes  $ph$  excitations formed from ground-state configurations of the fully or partially occupied states of positive energy, and the empty negative-energy states from the Dirac sea (solid lines in Fig. 44).

In Fig. 45 we plot the discrete GT spectrum for  $^{132}\text{Sn}$ . Two regions of excitation energies are shown. The panel on the right contains the positive energy  $\pi p - \nu h$  strength, with a pronounced Gamow-Teller resonance peak. The panel on the left displays the negative energy spectrum built from  $\pi \alpha - \nu h$  transitions ( $\alpha$  denotes a negative energy state). Even though these transitions are much weaker than the GTR (notice that the vertical scales are different for the two panels), there are many of them and their overall sum represents the strength missing in the positive energy sector.

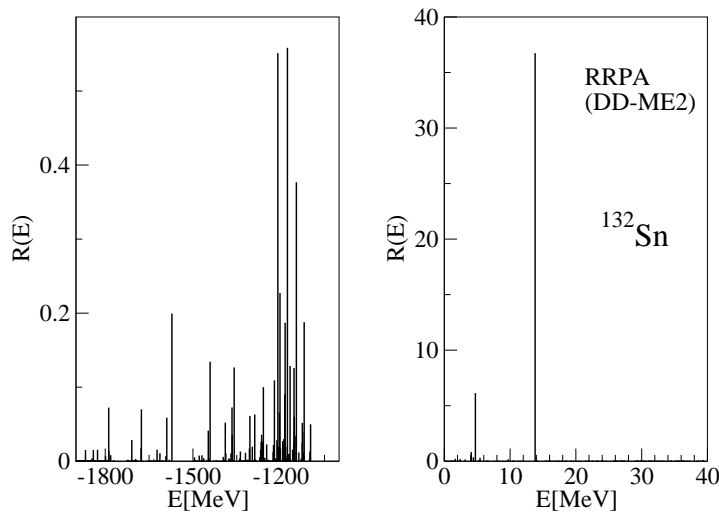


**Figure 45.** The PN-RQRPA strength distribution of discrete  $GT^-$  states for  $^{132}\text{Sn}$ . The panel on the right-hand side contains the positive energy  $\pi p - \nu h$  strength. The panel on the left displays the negative energy spectrum built from transitions to the empty states in the Dirac sea.

### 6.5. Spin-Isospin Resonances and the Neutron Skin of Nuclei

In medium-heavy and heavy neutron-rich nuclei the ground-states are often characterized by an extended neutron density distribution, and in some cases evidence has been reported for the formation of a neutron skin on the surface of the nucleus. The determination of neutron density distributions provides not only basic nuclear structure information, but it also places important additional constraints on effective interactions used in nuclear models. Extremely accurate data on charge densities, and therefore on proton distributions in nuclei, have been obtained from elastic scattering of electrons [325]. Data of comparable precision on neutron density distributions are, however, not yet available. It is much more difficult to measure the distribution of neutrons, though experimental information on the differences between radii of the neutron and proton density distributions has been reported [326, 327, 328]. Various experimental methods have been used, or suggested, for the determination of the neutron density in nuclei [329], but no existing measurement of neutron densities or radii has an accuracy better than a few percent.

One of the modern approaches that provides information about the neutron skin in nuclei is based on studies of giant resonances. In particular, in Ref. [326] excitations of the giant dipole resonance (GDR) were analyzed, and the spin-dipole resonance (SDR) was studied in [327]. The GDR cross section strongly depends on the difference between neutron and proton density distributions [330, 331, 332]. In Ref. [327] it has been demonstrated that there is a predictable correlation between the SDR cross section and

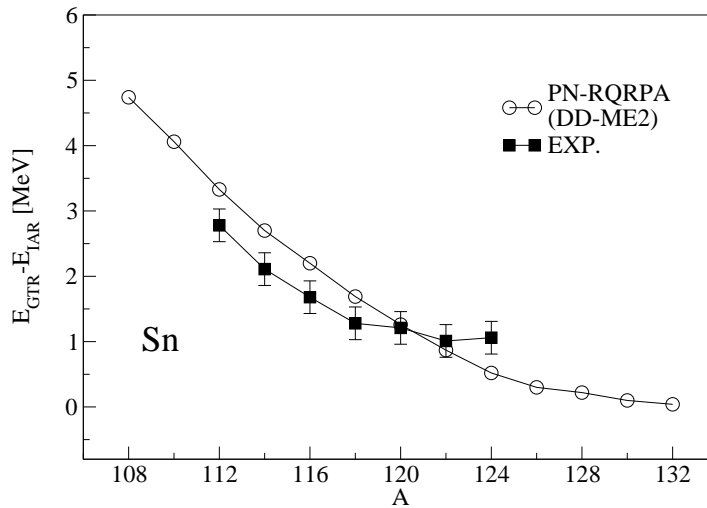


**Figure 46.** RHB plus proton-neutron RQRPA results for the energy spacings between the Gamow-Teller resonances and the respective isobaric analog resonances for the sequence of even-even  $^{112-124}\text{Sn}$  target nuclei. The experimental data are from Ref. [271].

the difference between the rms radii of the neutron and proton density distributions. By normalizing the results to  $^{120}\text{Sn}$ , data on neutron-skin thickness along the stable Sn isotopic chain were obtained, in good agreement with theoretical predictions.

Recently a new method has been suggested for determining the difference between the radii of the neutron and proton density distributions along an isotopic chain, based on measurement of the excitation energies of the Gamow-Teller resonances relative to the isobaric analog states [333]. The Gamow-Teller resonance (GTR)  $J^\pi = 1^+$  represents a collective spin-isospin oscillation with the excess neutrons coherently changing the direction of their spins and isospins without changing their orbital motion. The simplest charge-exchange excitation mode, however, does not require the spin-flip and corresponds to the well known isobaric analog state (IAS)  $J^\pi = 0^+$ . The spin-isospin characteristics of the GTR and the IAS are related through the Wigner supermultiplet scheme. The Wigner SU(4) symmetry implies the degeneracy of the GTR and IAS, and furthermore the resonances would completely exhaust the corresponding sum rules. The Wigner SU(4) symmetry is, however, broken by the spin-orbit term of the effective nuclear potential. The energy difference between the GTR and the IAS decreases with increasing asymmetry  $(N - Z)/A$ . It is implicit, therefore, that the energy difference between the GTR and the IAS reflects the magnitude of the effective spin-orbit potential. A number of relativistic mean-field calculations have shown that the magnitude of the spin-orbit potential is considerably reduced in neutron-rich nuclei [334], and this is reflected in the larger spatial extension of the neutron density, which becomes very diffuse on the surface. The neutron-skin increases correspondingly. The energy spacings

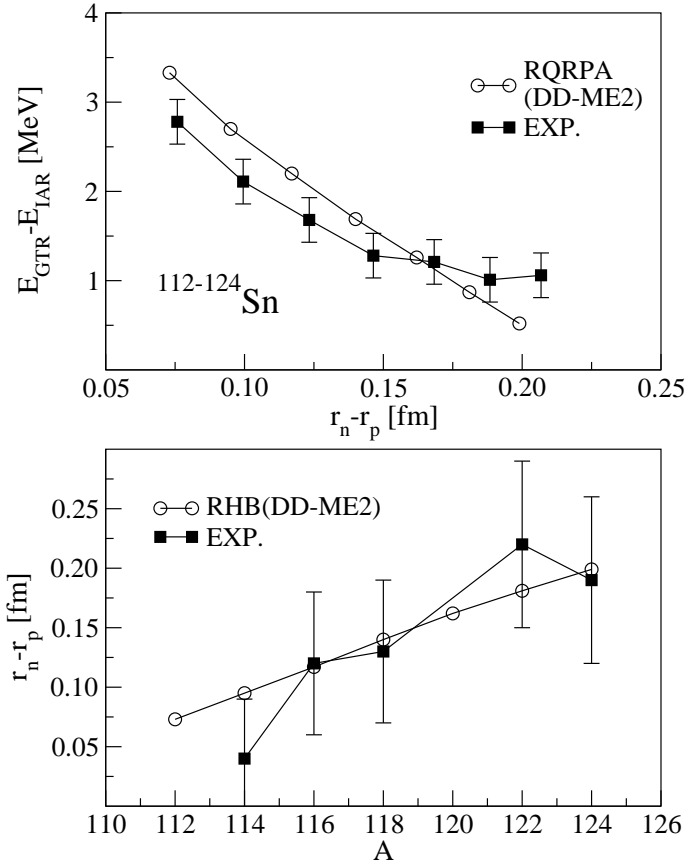


**Figure 47.** The PN-RQRPA and experimental [271] differences between the excitation energies of the GTR and IAR, as a function of the calculated differences between the rms radii of the neutron and proton density distributions of even-even Sn isotopes (upper panel). The calculated differences  $r_n - r_p$  are compared with experimental data [327] (lower panel).

between neutron spin-orbit partner states decrease, and this reduction is quantitatively in accordance with the gradual weakening of the spin-orbit term of the effective potential.

There is a direct connection between the increase of the neutron-skin thickness in neutron-rich nuclei, and the decrease of the energy difference between the GTR and the IAS. In Fig. 46 we display the calculated differences between the centroids of the direct spin-flip GT strength and the respective isobaric analog states for the sequence of even-even Sn target nuclei. For  $A = 112 - 124$  the results of RHB plus PN-RQRPA calculation (DD-ME2 density-dependent effective interaction, Gogny  $T = 1$  pairing,  $T = 0$  pairing interaction Eq. (96) with  $V_0 = 250$  MeV, the Landau-Migdal parameter  $g' = 0.52$  adjusted to reproduce the excitation energy of the GT resonance in  $^{208}\text{Pb}$ ), are compared with the experimental values obtained in a systematic study of the ( $^3\text{He}, t$ )

charge-exchange reaction over the entire range of stable Sn isotopes [271]. The calculated energy spacings are in very good agreement with the data, although for the lighter Sn isotopes it appears that the calculated values differ somewhat from the experimental trend. However, the theoretical energy spacings might depend on the details of the effective interaction and, in fact the data shown in Fig. 46 provide valuable information that can be used to constrain the spin-isospin channel of the effective interaction.

In Fig. 47 the calculated and experimental energy spacings between the GTR and IAS are plotted as a function of the calculated differences between the rms radii of the neutron and proton density distributions of even-even Sn isotopes (upper panel). We note the remarkable uniform dependence of the energy difference between the GTR and IAS on the size of the neutron-skin. This means that, in principle, the value of  $r_n - r_p$  can be directly determined from the theoretical curve for a given value of  $E_{\text{GTR}} - E_{\text{IAS}}$ . In the lower panel the calculated differences between neutron and proton rms radii are compared with available experimental data [327]. The agreement between the theoretical and experimental values suggests that the neutron-skin thickness can be determined from the measurement of the excitation energies of the GTR relative to IAS. This method is, of course, not completely model independent, but it does not require additional assumptions. Since the neutron-skin thickness is determined in an indirect way from the measurement of the GTR and IAS excitation energies in a sequence of isotopes, in practical applications at least one point on the theoretical curve should be checked against independent data on  $r_n - r_p$ .

## 7. Exotic Nuclear Modes in Astrophysical Processes

Collective modes play an important role in astrophysical processes that involve both stable and exotic nuclei far from stability. In particular, spin-isospin excitations such as the Gamow-Teller resonance are essential for weak-interaction processes, e.g.  $\beta$ -decay of exotic nuclei on the path of r-process nucleosynthesis, electron capture on neutron-rich nuclei at temperatures and densities characteristic for stellar core collapse, neutrino-induced reactions on heavy neutron-rich nuclei in the post-collapse supernova environment, including the process of neutrino nucleosynthesis. A recent review of nuclear weak-interaction processes in stars can be found in Ref. [311].

In this section we will review the role of non-charge-exchange nuclear collective modes in astrophysical processes. Particularly interesting is the effect of the low-lying dipole transition strength on the r-process nucleosynthesis, and in the propagation of ultra high-energy cosmic rays. We will also discuss exotic collective modes in the crust of a neutron star.

### 7.1. Low-Energy Dipole Strength and the r-process

Approximately half of the nuclides with  $A > 60$  found in nature are formed in the rapid neutron-capture process (r-process) nucleosynthesis. The nuclear input for r-

process calculations necessitates the knowledge of the properties of thousands of nuclei far from stability, including the characteristics of strong, electromagnetic and weak interaction processes [335]. Most of these nuclei are not accessible in experiments and, therefore, many nuclear astrophysics calculations crucially depend on accurate theoretical predictions for the nuclear masses, bulk properties, nuclear excitations,  $(n, \gamma)$  and  $(\gamma, n)$  rates,  $\alpha$ - and  $\beta$ -decay half-lives, fission probabilities, electron and neutrino capture rates, etc. Early calculations of the nuclear processes relevant for astrophysical applications were based only on phenomenological models [336, 337, 338, 339]. Only more recently large-scale microscopic calculations became standard in the prediction of nuclear masses [340], and dipole strength distributions [106, 107]. The availability of large scale microscopic calculations opens the possibility for global predictions of the nuclear ingredients for the r-process, based on an universal nuclear energy density functional. However, fully microscopic calculations of nuclear observables over the whole isotope chart are not yet feasible, especially for excited states. Only the excitation spectra of all even-even spherical nuclei can be obtained from fully consistent microscopic Skyrme-QRPA calculations [29], whereas for deformed, odd-even, and odd-odd nuclei a series of approximations must be designed specifically for astrophysical applications, and implemented in the microscopic QRPA.

Two principal candidates have been suggested for the astrophysical site of the r-process. In the first scenario the r-process takes place in explosive stellar events, such as the core collapse supernova [335], in an environment characterized by high neutron densities ( $N_n \simeq 10^{20} \text{ cm}^{-3}$ ), so that successive neutron-captures proceed into regions of neutron-rich nuclei far away from the valley of  $\beta$ -stability. If the temperature or the neutron density that characterize the r-process are low enough to break the  $(n, \gamma) - (\gamma, n)$  equilibrium, the waiting-point approximation is not valid any more, and the r-abundance distribution directly depends on the neutron-capture rates on exotic neutron-rich nuclei [336].

Recently an alternative scenario for the r-process has attracted renewed interest. It is related to the decompression of cold neutron star matter, in particular its crust (see [335] for a more detailed description). In this scheme the production of heavy nuclei follows a completely different path from the core-collapse supernovae scenario. The inner crust of a neutron star is composed of nuclear clusters immersed in a neutron gas. When a decompression of this crust occurs, nuclear clusters and the neutron gas are both ejected, and this leads to a decrease of the matter density. The  $\beta$ -equilibrium is broken and nuclei with  $Z$  in the range between 40 and 70 are produced. At very low density drip-line nuclei are formed, immersed in a neutron flux of  $N_n \simeq 10^{35} \text{ cm}^{-3}$ . The competition between the neutron-capture and the  $\beta$ -decay, starting from these drip-line nuclei, leads to the production of heavy nuclear systems. Because this type of nucleosynthesis starts from drip-line nuclei, where the waiting-point approximation cannot be applied, theoretical predictions of various structure phenomena are essential ingredients for r-process modeling.

Several types of nuclear observables are therefore required for the description of



r-process abundances. In addition to the  $\beta$ -decay rates, it is also necessary to describe the  $(n,\gamma)$  rates. This process can be divided into two steps: the neutron capture and the photo-deexcitation [341]. Nuclear masses and neutron-nucleus optical potentials enter into the calculation of the neutron-capture rates. The description of the photo-deexcitation process necessitates predictions of the E1 strength functions, as well the level densities in daughter nuclei. Neutron capture rates are evaluated in the framework of the Hauser-Feshbach statistical model, which is based on the fundamental assumption that the capture process occurs with the intermediary formation of a compound nucleus in thermodynamic equilibrium. In this approach the Maxwellian-averaged  $(n,\gamma)$  rate, at temperatures characteristic for the r-process environment, strongly depends on the electromagnetic interaction, i.e. on the photo-deexcitation probability. The modeling of the r-process abundances requires a reliable extrapolation of the E1-strength functions towards the neutron-drip line. Figure 48 shows a schematic picture of the  $(n,\gamma)$  reaction in the statistical model framework.

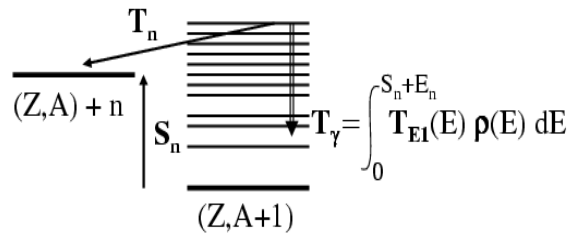


**Figure 48.** Illustration of the statistical radiative  $(n,\gamma)$  neutron-capture.  $T_n$  is the neutron-capture coefficient, and  $T_\gamma$  is the photo-transmission coefficient.  $T_\gamma$  is determined by the E1 strength  $T_{E1}(E)$ , and the level density  $\rho(E)$ .

Low-energy dipole modes are expected to play a more important role in the r-process than the higher lying strength, including the giant dipole resonance (GDR). Namely, the low-lying modes located close to neutron separation energy  $S_n$  are directly sustained by neutron-capture reactions, as shown in Fig. 48. The importance of the soft dipole modes has been emphasized in Ref. [336], where it has been shown that the presence of a low-lying resonant component of the E1 strength leads to an increase of the radiative neutron-capture rate by factors 10 – 100, for nuclei with  $S_n$  between 2 MeV and 4 MeV. The r-abundance distribution is affected because the presence of low-energy dipole resonances accelerates neutron capture and allows the production of heavy nuclei around  $A = 130$ .

Large-scale calculations of E1-strength functions for astrophysical applications are usually performed using phenomenological Lorentzian models [336]. Several refinements can be introduced, such as including the energy dependence and/or the temperature dependence of the width of the Lorentzian [336, 337, 338, 339]. The Lorentzian GDR approach presents, however, several problems. On one hand, in this framework it is not possible to predict the enhancement of the E1 strength at energies close the neutron

separation energy. On the other hand, even if a Lorentzian-type function provides a suitable description of the E1 strength in stable nuclei, the location of its maximum and its width for each nucleus remain to be predicted from some systematics or underlying model. For astrophysical applications these properties have often been obtained from a droplet-type model [342]. This approach is clearly not reliable when dealing with exotic nuclei, and this was already demonstrated in Refs. [106, 112]. In order to achieve a better description of the r-process, one has to improve the nuclear structure modeling. Generally speaking, the more microscopic the underlying theory, the more reliable will be the extrapolations towards the neutron drip-line. Microscopic calculations of the E1-strength functions for the whole nuclear chart have recently been reported [106, 107]. In a first step the dipole response was calculated with the QRPA based on the HF-Skyrme plus BCS description of nuclear ground states [106]. In neutron-rich nuclei pronounced E1 strength was predicted in the low-energy region below the giant dipole resonance.

The dipole strength can also be calculated with the QRPA based on HFB ground states [29, 343]. In this microscopic approach photoabsorption cross sections were determined [107], and one was able to judge the ability of the different forces to reproduce experimental data. In Refs. [340, 344, 345, 346] nuclear deformation was also taken into account. Based on the Skyrme-HFB approach, a number of new effective forces have recently been introduced [340, 345, 346]. Their parameters were *exclusively* adjusted to the 2135 experimental masses [347], with some additional constraints related to the stability of neutron matter and the incompressibility of nuclear matter. The new effective interactions BSk2-BSk7 are summarized in Ref. [335].

Photo-induced reaction cross sections were compiled in Refs. [348, 349], and represent the most reliable source of data with which HFB+QRPA predictions can be compared. These include the GDR parameters (the peak energy, peak cross section, and the full width at half maximum) observed in photonuclear reactions measured by bremsstrahlung, quasimonoenergetic and tagged photons for 84 nuclei. Among these, 48 nuclei are spherical and can be used to test the (HF-BCS or HFB)+QRPA predictions. Figure 49 shows the calculated GDR centroid energies of these 48 spherical nuclei using the HF-BCS+QRPA with the SLy4 parameterization, in comparison with the data.

For the BSk6 and BSk7 interactions, in particular, the comparison shows that these functionals not only reproduce the experimental masses with great accuracy (the rms deviation is only 0.676 MeV for the set of 2135 known masses), but also are suited for the description of E1 collective excitations [107]. The agreement with data is of the same level of accuracy as in the case of phenomenological models, i.e. the rms deviation for the GDR excitation energies is around 500 keV. However, since the microscopic HFB+QRPA approach potentially encompasses a wide range of phenomena, including the soft dipole mode, it is clearly preferable in large-scale calculations.

Turning now to astrophysical applications, microscopic predictions need to be extended on the whole nuclear chart, including also nuclei with an odd number of protons and/or neutrons, and deformed systems. The approximations that are currently used in these calculations include: the filling approximation for odd-A and odd-odd nuclei,

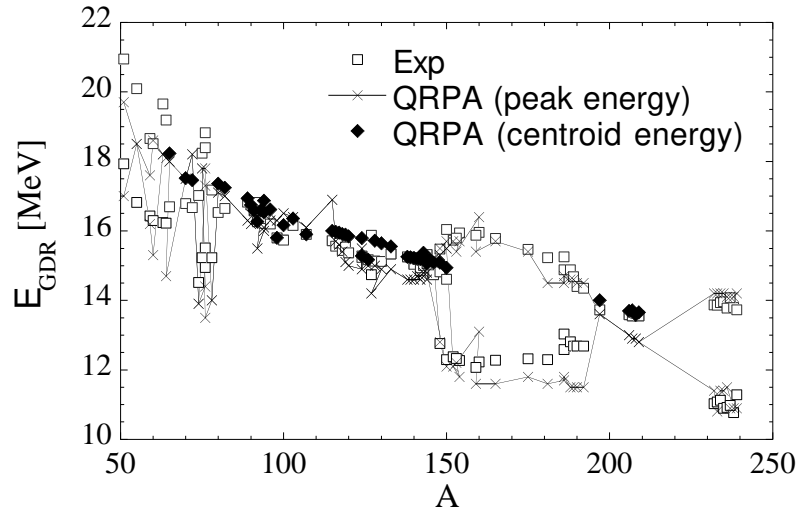


**Figure 49.** Comparison between the experimental GDR energies and the HF-BCS+QRPA calculations with the SLy4 force [106].

a phenomenological damping of the E1 strength, and a phenomenological treatment of deformation. These estimates may be improved in the near future, for instance by developing a deformed QRPA model that could be used in large-scale calculations of thousands of nuclei.

The QRPA provides a reliable description of the GDR centroid energy, but it is necessary to go beyond this approximation to describe the damping of collective motion. The GDR are empirically known to have rather large widths and therefore finite lifetimes, which can be described by several models [43, 92, 350]. In Ref. [106], for instance, the QRPA strength function was folded by an arbitrary Lorentzian adjusted to the empirical GDR width. The damping of the E1 strength can also be described by the approximate procedure developed in Ref. [43]. In the large-scale calculation of Ref. [107] the QRPA strength was folded by a Lorentzian function representing the self-energy operator [43, 351]. It is also necessary to introduce a temperature-dependent correction factor in the expression for the GDR width [338, 352, 353]. In deformed axially symmetric nuclei the GDR splits into two major components as a result of the different resonance conditions characterizing the oscillations of protons against neutrons along the axis of rotational symmetry, and an arbitrary axis perpendicular to it. In the phenomenological approach, the Lorentzian-type formula is generalized to a sum of two Lorentzian functions [354].

Large-scale QRPA calculations based on the BSk7 Skyrme interaction have recently been performed for some 8300 nuclei with  $8 \leq Z \leq 110$ , extending between the proton and neutron drip-lines [107]. In the region of neutron-deficient nuclei, as well as along the valley of  $\beta$ -stability, the calculated E1-strength functions are very similar to the empirical Lorentzian approximation. However, in neutron-rich nuclei the QRPA predictions start to deviate from the simple Lorentzian shape. In particular, low-lying transitions are found at excitation energies well below the GDR, and their strength

increases with neutron excess. This effect has been discussed in detail in Sec. 4.4. In Fig. 50 we plot the E1 strength function in Sn isotopes, calculated in the HFB+QRPA model with the BSk7 effective interaction. For  $A \geq 140$  a significant portion of the strength is concentrated at low energies:  $E \simeq 5 - 7$  MeV. It should be noted that phenomenological models cannot predict these low-energy components. For  $^{150}\text{Sn}$ , for instance, all phenomenological systematics that are used in calculations of neutron-capture cross sections, predict a  $\gamma$ -ray strength peaked around 15 MeV with a full width at half maximum of about 4.5 MeV [355]. This is obviously very different from the microscopic prediction shown in Fig. 50. More generally, HFB+QRPA calculations confirm that the neutron excess affects the spreading of the isovector dipole strength, as well as the centroid of the strength function. The energy shift is larger than predicted by the usual  $A^{-1/6}$  or  $A^{-1/3}$  dependence given by the phenomenological liquid drop approximations [342]. The basic features of the QRPA E1 strength function for nuclei with a large neutron excess are qualitatively independent of the choice of the effective interaction.

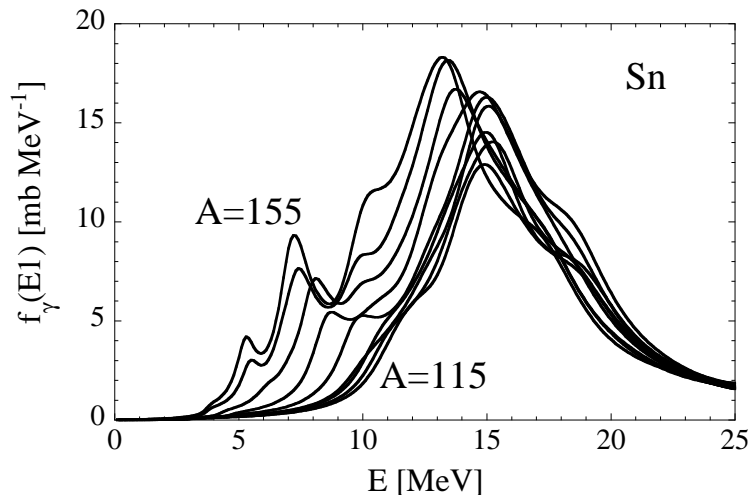


**Figure 50.** E1 strength functions for the Sn isotopic chain, calculated in the HFB+QRPA model with the BSk7 force. Only isotopes between  $A=115$  and  $A=150$ , with a step of  $\Delta A = 5$  are shown [107].

The radiative neutron capture cross sections are calculated with the Hauser-Feshbach statistical model [356], starting from nuclear ground state properties determined consistently in the microscopic HFB model with the same BSk7 Skyrme force [340]. The calculation includes the improved nuclear level density prescription based on the microscopic statistical model, also used to estimate the nuclear temperature [357]. The direct-capture contribution, as well as the possible overestimate of the statistical predictions for resonance-deficient nuclei, could have a significant effect on the radiative neutron capture by exotic nuclei [336]. However, we will focus on the role of the dipole strength, which is almost exclusively probed by the statistical model.

The results of the Hauser-Feshbach calculation can be compared to the

experimental  $(n,\gamma)$  cross-sections. However, it is more convenient to measure the inverse  $(\gamma,n)$  reaction. Such an experiment has recently been performed on  $^{181}\text{Ta}$ :  $^{181}\text{Ta}(\gamma,n)^{180}\text{Ta}$  [358]. In Fig.51 we show the comparison between the data and the Hauser-Feshbach calculations, obtained using either the QRPA E1 strength, or the phenomenological strength distributions. We notice that at low energies ( $E < 10$  MeV) the microscopic calculation of the dipole strength produces results which are in excellent agreement with data, but significantly different from those obtained with the phenomenological approach. The tail of the cross section between 7.5 and 10 MeV is attributed to the presence of the low-energy dipole (pygmy) mode in the QRPA calculation, which does not appear in the phenomenological models.

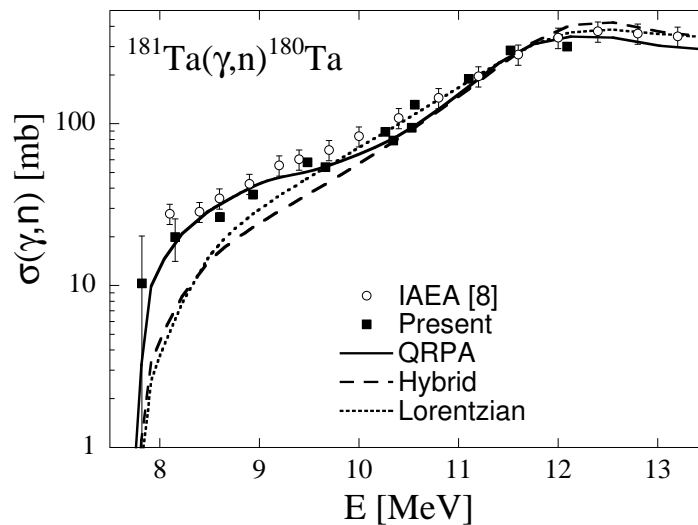


**Figure 51.** Comparison of the experimental photoneutron cross section for  $^{181}\text{Ta}$ , with the Hauser-Feshbach predictions obtained with the QRPA, hybrid, and Lorentzian models [358].

The Maxwellian-averaged neutron-capture rates calculated with the HFB+QRPA E1 strength functions are compared in Fig. 52 with those based on the Hybrid phenomenological formula, for all nuclei with  $8 \leq Z \leq 110$ . The Hybrid E1 strength differs from the QRPA estimate in the location of the centroid energy, as well as in the low-energy tail. Obviously the E1 strength obtained with QRPA enhances the capture rates by a factor up to 10 close to the neutron drip-line. For r-process nuclei characterized by neutron separation energies  $S_n \lesssim 3$  MeV, neutron capture proceeds much faster than predicted by the phenomenological Hybrid formula. This is due to the shift of the GDR to lower energies as compared to the usually adopted liquid-drop  $A^{-1/3}$  rule, as well as to the appearance of dipole modes at low energies. Both effects tend to enhance the E1 strength at energies below the GDR, i.e in the energy window relevant for the neutron capture process. For less exotic nuclei this effect is much smaller, and the differences are mainly due to the predicted location of the GDR and the strength of the low-energy tail. When compared to the HF-BCS+QRPA results [106], the HFB+QRPA model [107] predicts very similar neutron-capture rates, even close to the neutron drip-

line (see the lower panel in Fig. 52). This demonstrates the consistency of the results obtained with various microscopic approaches.

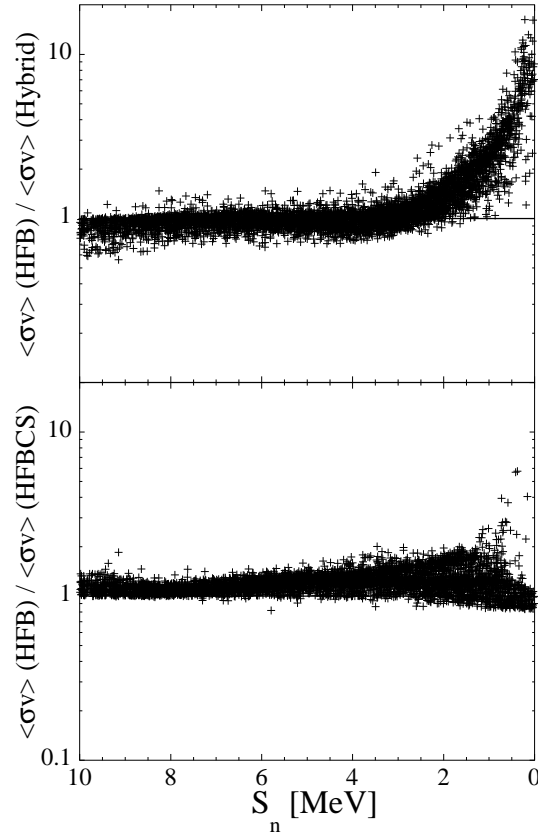


**Figure 52.** Upper panel: ratio of the Maxwellian-averaged  $(n,\gamma)$  rates (at a temperature of  $1.5 \cdot 10^9$  K) obtained with the HFB+QRPA E1 strength to those calculated with the Hybrid formula [336], as a function of the neutron separation energy  $S_n$  for all nuclei with  $8 \leq Z \leq 110$ . Lower panel: the ratios of the HFB+QRPA neutron-capture rates and those calculated with the HF-BCS+QRPA model of Ref. [106].

Many further improvements may be useful, but this will require intensive theoretical and computational advances. For instance, large-scale microscopic QRPA predictions of the E1 strength in deformed nuclei, the inclusion of the particle-vibration coupling effects on the low-energy strength, an improved treatment of odd and odd-odd nuclei, etc. The aim is to achieve a fully microscopic description of the r-process based on an universal nuclear energy density functional.

## 7.2. Nuclei as Ultra-High Energy Cosmic Rays

Cosmic rays are energetic particles that originate in the Universe, with observed energies up to  $\sim 3 \cdot 10^{20}$  eV [359, 360]. Astrophysical sites able to accelerate particles to such ultra high energies are currently under discussion. Among them, violent processes related to

neutron stars are possible candidates, because they generate strong magnetic fields able to confine protons of energy  $10^{20}$  eV. Figure 53 illustrates various natural accelerators in the Universe, and displays their typical magnetic field  $B$  with respect to their curvature radius  $\rho$ . The product  $B\rho$  value gives the energy which can be reached by the accelerated particles, from the well known relation  $B\rho = p/Q$  where  $p$  is the momentum of the particle, and  $Q$  its charge. Sites which could possibly accelerate protons to  $10^{20}$  eV are located in the shaded band.

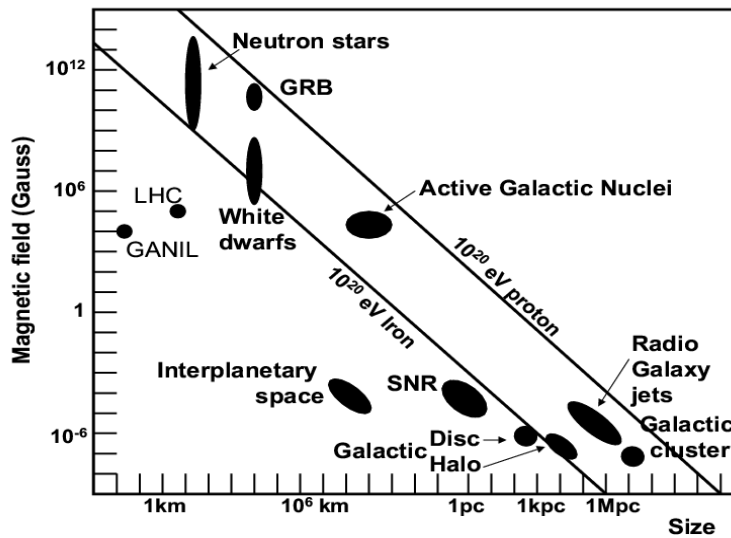


**Figure 53.** Various accelerators in the Universe, located on the plot of their magnetic field versus their size.

The composition of Ultra High Energy Cosmic Rays (UHECR) is not known. According to two principal hypotheses, they are composed either only of protons, or a mixture of protons and nuclei, ranging from hydrogen to iron. It has been known for almost four decades that UHECR interact with the 2.7 K cosmic microwave background radiation (CMB), leading for instance to a spectacular decrease in their flux above energies around  $10^{20}$  eV - the so-called Greisen, Zatsepin and Kuzmin (GZK) suppression [361, 362]. The following UHECR issues need to be addressed: the initial composition, the acceleration mechanism, and the intergalactic propagation. Going through these steps, the UHECR may reach an Earth based detection setup, such as the Auger detector [363]. The first two issues include many unsolved questions about the composition and acceleration processes of UHECR. It is therefore necessary to describe very accurately their propagation in order to provide a test of the composition and acceleration scenarios by comparing the predictions with data measured on Earth.

In the rest frame of a nucleus, at typical UHECR energies of  $10^{19}$ - $10^{21}$  eV, the CMB photons are boosted to the energy range between a few hundred keV, up to a few hundred MeV. The interaction process between the UHECR and the CMB is dominated by the giant dipole resonance (GDR) at photon energies below 30-50 MeV, and to a lesser

extent by the quasideuteron emission at intermediate energies (between 50 MeV and 150 MeV), and the pion photoproduction at energies above 150 MeV [364, 365]. Figure 54 displays the mean free path of  $^{56}\text{Fe}$  nuclei for various photonuclear processes, and shows the predominant role of the GDR. Nuclei photodesintegrate by emitting nucleons through  $(\gamma, n)$ ,  $(\gamma, p)$ ,  $(\gamma, 2n)$ , ... reactions. It is therefore necessary to accurately describe the dipole strength for the nuclei on the photodisintegration path from Fe to protons. It should be noted that many nuclei along this path are unstable, for instance  $^{44}\text{Ti}$ .

In order to describe the changes in the abundance of heavy nuclei as a result of the interaction of the UHECR with the CMB, a nuclear reaction network that includes all interactions of interest must be used. The chosen set of nuclear species are coupled by a system of differential equations corresponding to all the reactions affecting each nucleus, i.e. mainly photodisintegrations and  $\beta$ -decays [366]. All nuclei lighter than the seed nuclei and located between the valley of stability and the proton drip-line must be included in the network. Under the most natural astrophysical assumptions, UHECR are accelerated out of the ambient gas, possibly enriched in Fe close to neutron stars or depleted in metals (i.e. nuclei heavier than H) if significant photodisintegration occurs during the acceleration stage itself. Therefore, if nuclei are indeed present among the UHECR, it is expected that they typically include the most abundant elements found in the interstellar medium, i.e. essentially those lighter than Fe. The interaction of UHECR with the CMB is thus expected to include all possible nuclei resulting from the photodisintegration of the heaviest species and therefore involve all stable and neutron-deficient unstable isotopes with  $A \leq 56$ .

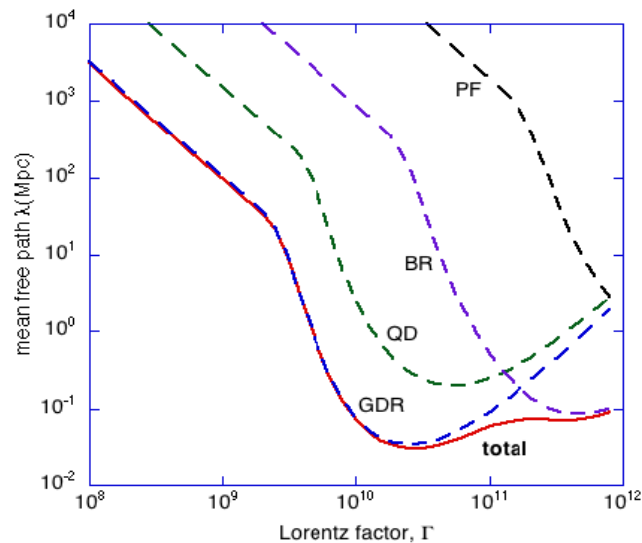


**Figure 54.** Mean free path of  $^{56}\text{Fe}$  nuclei against the various processes in the CMB: Giant Dipole Resonance (GDR), Quasi-Deuteron process (QD), Baryonic Resonance (BR) and Pion Photoproduction (PF) [367].

The UHECR photodisintegration was originally investigated by Puget, Stecker and Bredekamp (PSB) [364, 368]. However, in the PSB model two major approximations



were employed to estimate the intergalactic UHECR propagation. The first is related to the total photoabsorption cross section which is parameterized as a simple Gaussian function [364, 368], abruptly cut below the theoretical reaction threshold. The second is based on the use of a reduced reaction network, including only one nuclide for each value of  $A$ , to estimate the time evolution of the UHECR composition. More precisely, assuming that the  $\beta$ -decay of the unstable nuclei produced by photodisintegration is always faster than the corresponding photoemission rate, a unique nuclear path is followed from the initial  $^{56}\text{Fe}$  source to the final protons [364], neglecting the contribution of unstable nuclei. It is necessary to achieve an accurate description of the photodisintegration rates using photoreactions that are extensively studied in nucleosynthesis, where phenomenological parameterizations of the photoabsorption cross sections have been optimized during the last decades, and where large-scale microscopic predictions have also become available, as described in section 7.1 [106, 107]. New compilations of experimental photoabsorption data also help to determine the degree of accuracy with which the present reaction models predict the corresponding cross sections. Important progress has also been made in the field of nucleosynthesis by solving large reaction networks on the nuclear chart and thus following the time evolution of the composition of the material at given astrophysical sites. Similar tools can therefore be used in the field of UHECR in order to take into account the contribution of unstable nuclei during the photodisintegration path.

The total photon transmission coefficient characterizing the probability to populate by photoabsorption a compound nucleus excited state is obviously one of the key ingredients for the evaluation of the photoreaction rates. In the specific astrophysical conditions considered for UHECR energies of  $10^{19-21}$  eV, this function is dominated by the  $E1$  transition. To estimate the accuracy of the different methods available for the evaluation of an  $E1$ -strength function, four models have been considered: the Lorentzian [369], the generalized Lorentzian [352], the HF-BCS+QRPA [106], and the HFB+QRPA [107]. The former two are phenomenological, and the latter two are microscopic.

The photoreaction cross sections are estimated with the Talys nuclear reaction code [235, 370], which takes into account all types of direct, pre-equilibrium and compound mechanism to estimate the total reaction probability, as well as the competition between the various open channels. The quasideuteron process is neglected because of the limited photon energy range [365]. The predictions are compared with available experimental data [371] for nuclei with  $A \leq 56$ . It should be noted that, even for stable nuclei, the data on such nuclei are scarce. For instance, total photoabsorption cross sections around the GDR peak energy are available for only 10 nuclei [371]. An extensive study has been performed to compare the predictions with the data [366]. Both the microscopic and the Lorentzian approaches correctly describe the data, because the nuclei involved lie close to the valley of stability.

The intergalactic UHECR propagation is calculated considering the interaction with the CMB. For illustrative purposes, we will restrict ourselves in a first step to study the

propagation of a UHECR source made of  $^{56}\text{Fe}$  only. All stable and neutron-deficient unstable nuclei with  $A \leq 56$  are included in the reaction network. Fig. 55 shows the evolution of the average mass number  $\langle A \rangle$  as a function of the distance from the  $^{56}\text{Fe}$  source, calculated with the four GDR prescriptions. For a given source distance,  $\langle A \rangle$  is the average value of the calculated nuclei abundances. The full reaction network is solved at each time-step, taking into account all open photoemission channels, i.e.  $(\gamma, n)$ ,  $(\gamma, p)$ ,  $(\gamma, \alpha)$ ,  $(\gamma, 2n)$ ,  $(\gamma, 2p)$ ,  $(\gamma, 2\alpha)$ ,  $(\gamma, np)$ ,  $(\gamma, n\alpha)$ ,  $(\gamma, p\alpha)$ . In other words, the abundance of each nuclide is derived by taking into account the contribution of all production channels, from the source nucleus downwards the table of nuclides, with the appropriate weight determined according to the corresponding cross sections. The values obtained are thus equilibrium values, representing the composition which would result from the propagation of an infinite number of nuclei up to the time considered.

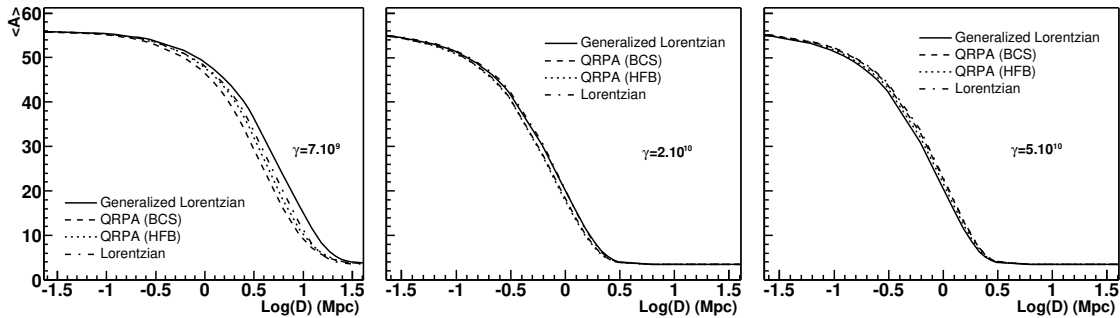


**Figure 55.** Evolution of the average mass number  $\langle A \rangle$  with respect to the distance from the  $^{56}\text{Fe}$  source for three different energies. Left:  $E = 3.6 \times 10^{20}$  eV; center:  $E = 10^{21}$  eV; right:  $E = 2.61 \times 10^{21}$  eV [366].

To illustrate the role of the soft dipole mode, let us consider a  $^{56}\text{Fe}$  nucleus with an energy of  $3.6 \times 10^{20}$  eV. In this regime only the lowest energy part of the  $E1$ -strength overlaps with the photon density  $n(\epsilon)$ . The distance of propagation is mainly sensitive to the low-energy component of the  $E1$ -strength function, and using different prescriptions leads to significant differences in the propagation distance. This emphasizes the necessity accurately describe the low energy tail of the  $E1$  strength, even for nuclei close to the valley of stability. In contrast, results for  $^{56}\text{Fe}$  at higher energy mainly depend on the location of the GDR peak or integrated photoabsorption, and for this reason the propagation distance is less sensitive to the photoreaction details.

The UHECR propagation distance has been estimated using the complete reaction network. The initial PSB calculations were based on the reduced PSB path illustrated in Fig. 56. In this approximation, as explained above, only one stable isotope is considered for an isobaric chain and the corresponding isobars are not affected by competitive channels. However, as shown in Fig. 56, about 85 nuclei are involved in the  $^{56}\text{Fe}$  photodisintegration at  $E = 10^{21}$  eV, and a number open channels, including  $\beta$ -decay, can compete (the Lorentz dilation of time allows  $\beta$ -unstable nuclei with half-lives of the order of an hour to survive over a Mpc scale, and thus have a chance to interact with

a CMB photon). Most of the stable nuclei involved in the photodisintegration process have more neutrons than protons. Neutron photo-emissions are therefore favored and the corresponding unstable nuclei will  $\beta^+$ -decay towards the valley of stability.

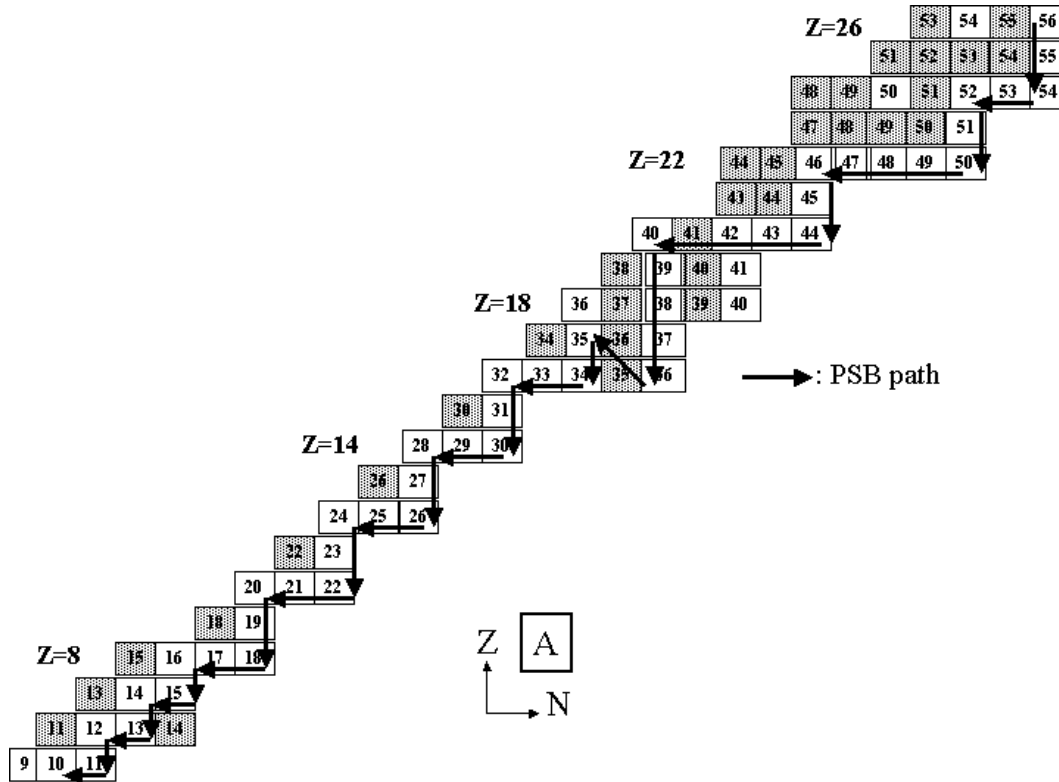


**Figure 56.** Nuclei involved in the photodisintegration process of  $^{56}\text{Fe}$  at  $E = 10^{21}\text{eV}$ . Unstable nuclei are denoted by shaded squares, and the PSB path is indicated by arrows. The mass number  $A$  of each nucleus is written in the corresponding square [366].

Significant discrepancies are therefore expected between the recent calculation in Ref. [366], and the original PSB results based on the reduced path and the Gaussian parameterization of GDR strengths. In particular, as seen in Fig. 56 for  $A \geq 45$ , about 70% of the nuclei are shortcut by the simplified PSB path. For  $E = 3.6 \times 10^{20}\text{eV}$ , a significant difference is found between the PSB predictions and the one using an accurate E1 strength description, such as the QRPA or the generalized Lorentzian. This effect is due to the prediction of the low-energy part of the dipole strength, which in the PSB case does not agree with the data.

A full propagation calculation based on a Monte-Carlo simulation, has been performed in Ref. [367]. A mixed source of protons and nuclei with  $A < 56$  has been considered, as well as quasideuteron, pion photoproduction, and pair-production processes. As shown in Fig. 57, the propagated spectra are in good agreement with the cosmic ray data. The effect of the prediction of the dipole strength compared to the PSB parameterization is non-negligible, and the sensitivity to the description of the

E1 strength will become even more important, because the data provided by the Auger detector will drastically reduce the statistical error bars at high energy.

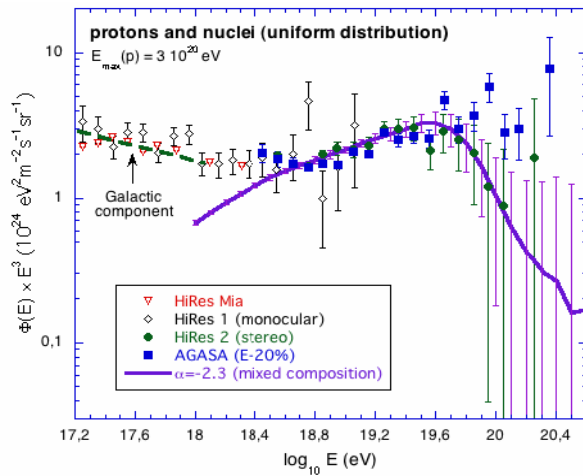


**Figure 57.** Propagated spectra from a source composed of protons and nuclei (solid line), compared with available data [367].

In Ref. [367] it has also been shown that a mixed composition of protons and nuclei provides a reasonable interpretation of the high energy part of the CR spectrum around the so-called ankle area. Better agreement with observed data is obtained with composite source models, than with just a uniform proton source. Moreover, the work of Ref. [372] has shown that by including nuclei in UHECR a much better agreement with complementary experimental observables is obtained. All these studies support the hypothesis that UHECR may be composed of nuclei.

### 7.3. Supergiant Resonances in the Inner Crust of Neutron Stars

Some of the most exotic nuclear excitations could arise in the crust of neutron stars. In microscopic calculations the inner crust matter is usually described in the Wigner-Seitz (WS) approximation [373, 374], i.e. the inner crust is modeled by non-interacting cells that contain a neutron-rich nucleus immersed in a dilute gas of neutrons and relativistic electrons. For baryonic densities in the range from  $1.4 \cdot 10^{-3} \rho_0$  about  $0.5 \rho_0$ , where  $\rho_0 = 0.16 \text{ fm}^{-3}$  is the nuclear matter saturation density, nuclear clusters can be considered spherical [374, 375]. At higher densities, the inner crust matter can develop various non-spherical phases (e.g. rods, slabs, tubes, bubbles) [373]. The structure of the WS cells has been analyzed as a function of their density [374], which is related to the distance of the WS cell from the center of the neutron star. The equilibrium condition for the WS cells has been derived, with the values of  $Z$  and  $N$  that minimize the energy of the system. The resulting values of  $Z$  are typically located between 10 and 50, depending on the density of the WS cell. The corresponding number of neutrons  $N$  is about several hundreds. Therefore the cell with  $Z=50$  and  $N=1750$  is quoted as  $^{1800}\text{Sn}$ . In this cell the density of the neutron gas far from the nuclear cluster is  $\approx 0.018$

$\text{fm}^{-3}$ , and the radius of the cell is 27.6 fm. The WS cell can therefore be represented as a drip-line nucleus immersed in a neutron gas, and considered as a system between a finite nucleus and the uniform neutron matter. Nuclear collective modes are expected to develop in such systems, and several interesting questions arise: What is the structure of collective states in these extremely neutron-rich systems? What is the relationship between the nuclear cluster and the neutron gas? Can the study of very neutron-rich nuclei be helpful in understanding these excitations?

The cooling of low-mass neutron stars is strongly influenced by the superfluid properties of inner crust matter [376]. These properties and their effect on the specific heat have been analyzed in various theoretical frameworks, e.g. semiclassical pairing models [377, 378], Bogoliubov-type calculations based on a Woods-Saxon mean-field [379, 380], and the self-consistent Hartree-Fock-Bogoliubov (HFB) approach [381, 382]. These calculations have shown that pairing correlations can reduce by orders of magnitude the specific heat of baryonic matter in the inner crust. It must be emphasized, however, that the specific heat was evaluated for a system of non-interacting quasiparticles. This quantity can also be strongly affected by collective modes determined by the residual interaction between quasiparticles, especially if these modes appear at low-excitation energy. This effect has been studied in Ref. [383, 384]. It should be noted that the specific heat of the inner crust is also determined by the motion of electrons and, to a lesser extent, by lattice vibrations [373, 376, 380, 385]. These degrees of freedom of the inner crust matter will not be taken into account in the present discussion.

In Ref. [383] RPA calculations were performed for  $^{580}\text{Sn}$ , and a pronounced low-lying quadrupole peak was obtained. In order to take into account pairing effects, it is convenient to calculate the collective response with the HFB+QRPA model formulated in the coordinate representation [29]. This representation is particularly suited to describe systems with a large number of quasiparticle states, such as WS cells. In the first step of the calculation the HFB equations for the ground-state of the given WS cell are solved, considered as an isolated system. The HFB calculations are performed in the coordinate representation and the Dirichlet-Neumann boundary conditions are imposed at the contour of the cell [374]. These are the only discretization conditions which can produce a constant density around the outer boundary of the WS cell. Figure 58 displays the HFB results for the particle densities of the  $^{1800}\text{Sn}$  and  $^{982}\text{Ge}$  WS cells [384]. The density profiles are very diffuse, because of the presence of the neutron skin on the surface of the nuclear cluster ( $\simeq 7$  fm). At larger radii the densities remain constant and correspond to the neutron gas component.

The response of several cells has been calculated within the HFB+QRPA model, e.g.  $^{1500}\text{Zr}$ ,  $^{1800}\text{Sn}$  and  $^{950}\text{Ge}$  [384]. In these cells a very collective low-lying state has been predicted, located in the energy region between 2 and 4 MeV. This SuperGiant Resonance (SGR) typically exhausts around 70 % of the EWSR [384]. The analysis of the SGR structure has shown that the contributions of the nuclear cluster and the neutron gas to the neutron transition density are comparable. However, the magnitude

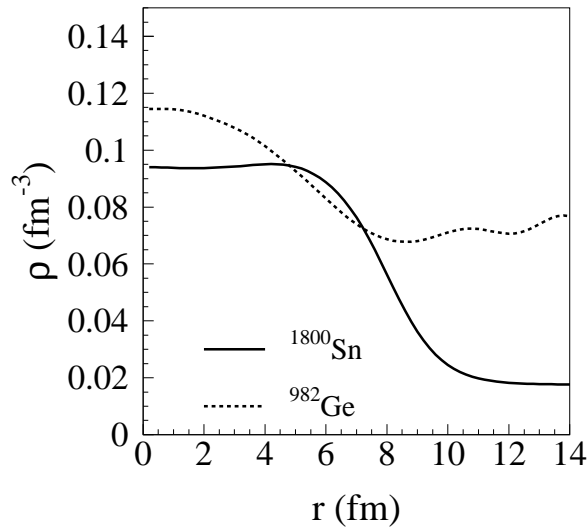


**Figure 58.** Particle densities for the WS cells  $^{1800}\text{Sn}$  and  $^{950}\text{Ge}$ , calculated with the HFB model [384].

of the strength (but not the energy position) is mainly determined by the neutron gas, because it is given by  $\int dr r^{L+2} \delta\rho(r)$  for a given multipole  $L$  (cf. Eq (75)), and this strongly favors effects located at large radii.

The monopole, dipole, and quadrupole neutron response of the cell  $^{1800}\text{Sn}$  are shown in Fig. 59. We display both the unperturbed HFB response built from non-interacting quasiparticle states, and the QRPA response function. When the residual interaction between quasiparticles is turned on, the unperturbed spectrum, which is distributed over a large energy region, is collected in a strong peak located at about 3 MeV. All multiplicities exhibit the SGR, and in the case of the quadrupole response the SGR peak collects more than 99% of the total quadrupole strength. This mode is extremely collective, there are more than one hundred two-quasiparticle configurations contributing to the QRPA amplitude, and its reduced transition probability  $B(E2) \approx 25 \times 10^3$  Weisskopf units. This value is two orders of magnitude larger than the  $B(E2)$ 's found in ordinary nuclei. It should be noted that the extrapolation of the energy position based on the Giant Quadrupole Resonance systematics in finite nuclei, i.e.  $65A^{-1/3}$  MeV [6], predicts the low-energy peak at about 5 MeV. The additional lowering of the peak, which is due to the comparable contributions of the nuclear cluster states and the neutron gas, shows that the WS cells cannot be simply considered as giant nuclei.

In order to study collective excitations at higher baryonic densities of the inner crust matter, the response of the cell  $^{982}\text{Ge}$  has also been calculated in Ref. [384]. In this cell the cluster and the neutron gas are less separated than in the case of  $^{1800}\text{Sn}$  (see Fig. 58). Because of the large degeneracy of states located close to the Fermi level,

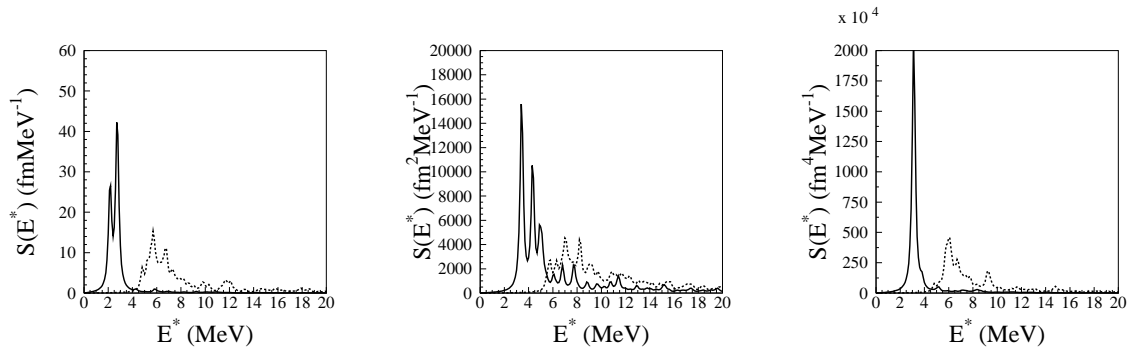


**Figure 59.** Monopole (left), dipole (center) and quadrupole (right) strength distributions for the cell  $^{1800}\text{Sn}$ . The solid and dashed curves represent the QRPA strength and the HFB unperturbed strength, respectively.

many particle-hole configurations add coherently to form the SGR. It is also interesting to investigate whether the contribution of the free neutron gas to the collective mode could be eventually described in a semiclassical picture by using the hydrodynamic model. This requires a coherence length that is much smaller than the size of the system [386], and is only fulfilled for the most external WS cells, such as  $^{1800}\text{Sn}$ . For the WS cells of higher density, such as  $^{1500}\text{Zr}$  and  $^{982}\text{Ge}$ , the hydrodynamic model cannot reproduce the energy position of the SGR [384].

The predicted energies of the SGR are of the same order of magnitude as the average pairing gap of the neutron superfluid and, consequently these modes could have a significant effect on the entropy and the specific heat of baryonic matter in the inner crust. A quantitative estimate of these effects will require finite-temperature HFB+QRPA calculations [387]. There are, however, open questions about the validity of the non-interacting WS approximation in the description of collective modes. Their amplitude is strongly sensitive to the surface, where the neutron gas connects two contiguous cells. Tests have been performed by modifying the Dirichlet-Neumann boundary conditions, but no pronounced deviation of the strength has been found. The role of the coupling between two contiguous WS cells through the neutron gas should be investigated. The cells which have an impact on the specific heat remain also to be determined and, finally, neutron-rich nuclei which will be produced by the next-generation radioactive-beam facilities, could provide data that will constrain models and functionals which describe WS cells.

## 8. Concluding Remarks and Outlook

Experimental studies with radioactive isotope beams have disclosed a wealth of structure phenomena in nuclei far from the line of  $\beta$ -stability. Among the most interesting results are those on the evolution of collective modes of excitation in regions of unstable nuclei, and the possible existence of entirely new types of excitation in weakly-bound systems. The best studied example is the evolvement of the dipole response in neutron-rich nuclei,

and the possible occurrence of the pygmy dipole resonance: the resonant oscillation of the weakly-bound neutron skin against the isospin saturated proton-neutron core. However, even in this case the available data on the low-energy dipole response do not discriminate between various theoretical interpretations. In nuclei near the neutron drip-line new types of excitation could be induced by the strong surface pairing properties as, for instance, the soft dipole pairing mode. On the proton-rich side, even if the protons do not develop a pronounced skin structure, in relatively light nuclei close to the proton drip-line the weakly-bound proton orbitals, including states which are bound only because of the presence of the Coulomb barrier, could contribute to the evolution of the proton pygmy dipole resonance. The existence of exotic isoscalar modes has also been predicted: a low-lying dipole mode which could correspond to the toroidal dipole resonance, giant pairing vibrations, quadrupole excitations and higher multipoles. The increasing interest in exotic collective modes has led to important advances both in the experimental methods and theoretical tools that are used in the study and interpretation of these phenomena.

A modern microscopic time-dependent mean-field theory of collective excitations in nuclei far from stability necessitates a fully self-consistent implementation of effective nuclear interactions: both the equations which determine the ground state of a nucleus, and the residual interaction which governs the small-amplitude vibrations around the equilibrium, must be derived from the same effective interactions in the particle-hole and particle-particle channels. Only fully self-consistent calculations ensure the separation of spurious states from the physical excitations, and provide reliable microscopic predictions of collective modes directly based on ground-state properties. The presently available models which meet these conditions are: the HFB plus QRPA based on Skyrme or Gogny effective interactions, and in the relativistic framework the RHB plus RQRPA based on effective Lagrangians with density-dependent meson-nucleon couplings. Even though some of these state-of-the-art models include the coupling to the particle continuum, i.e. they take into account the escape width of vibrational states that lie above the particle emission threshold, one really must go beyond the mean-field approximation in order to quantitatively describe decay properties of collective excitations. At present only few theoretical approaches take into account in a fully consistent way the coupling of the simple  $1p - 1h$  (or two-quasiparticle) states to more complex  $2p - 2h$  configurations, which basically determines the spreading width of resonances. The way the damping mechanism is modified in nuclei far from stability, e.g. neutron-rich nuclei, is therefore largely unexplored.

Studies of low-energy collective excitations in nuclei with relatively moderate neutron excess provide crucial information on the manifestation of exotic modes in neutron-rich nuclei, and their subsequent evolution towards systems with large isospin asymmetry near the nucleon drip-lines. Evidence for the existence of low-lying dipole strength in neutron-rich nuclei, which might indeed correspond to the pygmy dipole resonance (PDR), has become available from several experiments based on  $(\gamma, \gamma')$  resonant scattering, and data on low-lying E1 strength in exotic nuclei has recently



been obtained in studies with radioactive ion beams. Experimentally, however, very little is known about the nature of the observed low-lying dipole states, the degree of collectivity and the isospin character, and extensive investigations have to be carried out. For instance, studies of low-energy transition strength below the particle emission threshold in  $(\alpha, \alpha'\gamma)$  coincidence experiments, which enable a clear separation of E1 excitations from states of other multiplicities, will allow a more detailed analysis of the structure of these states [388].

A number of theoretical studies have recently been devoted to properties of the PDR, and some models predict an enhancement of collectivity for these states, and pronounced mixing of isoscalar and isovector components. An important issue in neutron-rich nuclei is also the relationship between the PDR excitation energy and the neutron separation threshold. It appears that in nuclei not so far from stability the PDR is located below or very close to the neutron separation energy, whereas in weakly-bound systems with large neutron excess the PDR energy is high above the neutron threshold. Only part of the low-lying E1 strength is observed in current experiments. While the  $(\gamma, \gamma')$  spectra are composed of peaks below the threshold energy, the Coulomb excitation of fission fragments gives the transition strength above the neutron separation energy. Future experiments therefore need to provide complete low-lying dipole spectra, both below and above the neutron threshold energy. A comparison of the complete spectra of measured low-lying strength in nuclei far from stability with the predictions of self-consistent microscopic theories, will present a very sensitive test for the isovector channel of nuclear effective interactions. Namely, it is difficult to adjust the isovector terms of effective interactions only to data in stable nuclei. Stringent constraints on the microscopic approach to nuclear dynamics and effective nuclear interactions will emerge from studies of the structure and stability of exotic nuclei with extreme isospin values.

Except for the PDR, few data have been reported so far on other possible exotic modes of excitation, but dedicated experiments are being planned and designed at radioactive-beam laboratories. For instance, in the near future more information could become available on modes which arise in nuclei near the drip-lines: the proton PDR, and the di-neutron *vs* core oscillations. An important question which has not been addressed so far is the evolution of low-energy modes with temperature in hot nuclei, a topic that could be important for astrophysical applications. The dipole toroidal mode could be probed by the measurement of transverse electron scattering form factors at  $180^\circ$ . An entirely unexplored field is the evolution of modes that involve the spin and/or isospin degrees of freedom in nuclei far from stability. It must also be emphasized that while most theoretical studies of exotic modes of excitation have assumed spherical symmetry, the evolution of deformation in unstable neutron-rich nuclei could give rise to interesting collective phenomena such as, for instance, the low-energy scissors mode of oscillation of the neutron skin [389].

Of particular importance is the role that new exotic modes or, more generally collective excitations in nuclei far from stability, play in astrophysical processes: the description of Gamow-Teller resonances is essential in calculations of  $\beta$ -decay,

electron capture and neutrino-nucleus interaction rates; the low-energy dipole transition strength in neutron-rich nuclei has a pronounced effect on the calculated r-process abundances and on the propagation of ultra-high energy cosmic rays; on the proton-rich side the proton pygmy dipole resonance could contribute to the nucleosynthesis in rapid proton capture processes, as well as in the two-proton capture in astrophysical conditions characteristic for explosive hydrogen burning in novae and x-ray bursts [390]. Theoretical studies of electron capture rates on neutron-rich nuclei, at temperatures and densities characteristic for core collapse, have recently shown that these rates can be so large that electron capture on nuclei dominates over capture on free protons. Further studies of capture rates, particularly in a self-consistent approach extended to finite temperatures, are clearly desirable. The effect of giant resonances in extremely neutron-rich systems on the cooling time of neutron stars should also be investigated. Neutrino-nucleus reactions in the low-energy range 1-100 MeV play an important role in many astrophysical processes, including stellar nucleosynthesis, and the study of low-energy neutrino reactions on medium-heavy and heavy nuclei is of great current interest. Since the description of a neutrino-nucleus reaction becomes increasingly complicated as the target mass number increases, accurate self-consistent mean-field approaches must be developed and applied in calculations of cross sections for all relevant neutrino-induced reactions. More generally, microscopic nuclear structure theory must be integrated into various astrophysical models of nucleosynthesis processes, supernova dynamics, and neutrino-induced reactions, by providing accurate global predictions for bulk nuclear properties and nuclear excitations.

## **ACKNOWLEDGMENTS**

Many students and colleagues have contributed to the work reviewed in this article. In particular, we would like to thank D. Allard, T. Aumann, F. Barranco, K. Bennaceur, K. Boretzky, P. F. Bortignon, R. A. Broglia, H. Emling, P. Finelli, S. Fracasso, F. Ghielmetti, Nguyen Van Giai, G. Giambrone, S. Goriely, M. Grasso, I. Hamamoto, D. T. Khoa, A. Klimkiewicz, G. A. Lalazissis, Zhong-yu Ma, J. Margueron, M. Matsuo, J. Meyer, P. von Neumann-Cosel, T. Nikšić, B. Özel, P. Papakonstantinou, V. Yu. Ponomarev, M. R. Quaglia, F. Ramponi, P. Ring, R. Roth, H. Sagawa, N. Sandulescu, D. Sarchi, H. Utsunomiya, E. Vigezzi, A. Vitturi, and S. Volz. This work has been supported in part by the Croatian Ministry of Science and Education under project 1191005-1010, by the Deutsche Forschungsgemeinschaft (DFG) under contract SFB 634, and by the INFN.

## References

- [1] P. Ring, P. Schuck, *The Nuclear Many-Body Problem*, Springer-Verlag, Heidelberg, 1980.
- [2] J.-P. Blaizot, G. Ripka, *Quantum Theory of Finite Systems*, The MIT Press, Cambridge, 1986.
- [3] J.D. Walecka, *Theoretical Nuclear and Subnuclear Physics*, World Scientific, Singapore, 2004.
- [4] G.F. Bertsch, R.A. Broglia, *Oscillations in Finite Quantum Systems*, Cambridge University Press, 1994.
- [5] P.F. Bortignon, A. Bracco, R.A. Broglia, *Giant Resonances. Nuclear Structure at Finite Temperature*, Harwood Academic, New York, 1998.
- [6] M.N. Harakeh, A.M. Van Der Woude, *Giant Resonances: Fundamental High-Frequency Modes of Nuclear Excitations* Oxford University Press, 2001.
- [7] M. Bender, P.-H. Heenen, P.-G. Reinhard, *Rev. Mod. Phys.* 75, 121 (2003).
- [8] D. Vretenar, A. V. Afanasjev, G. A. Lalazissis, P. Ring, *Phys. Rep.* 409, 101 (2005).
- [9] W. Kohn, L.J. Sham, *Phys. Rev.* 137, A 1697 (1965).
- [10] W. Kohn, *Rev. Mod. Phys.* 71, 1253 (1999).
- [11] R.M. Dreizler, E.K.U. Gross, *Density Functional Theory*, Springer, Berlin, 1990.
- [12] J. Dechargé and D. Gogny, *Phys. Rev. C* 21, 1568 (1980).
- [13] J.F. Berger, M. Girod and D. Gogny, *Comp. Phys. Comm.* 63, 365 (1991).
- [14] D. Vautherin and D. Brink, *Phys. Rev. C* 5, 626 (1972).
- [15] M. Beiner, H. Flocard, N. Van Giai and Ph. Quentin, *Nucl. Phys.* A238, 29 (1975).
- [16] E. Chabanat, P. Bonche, P. Haensel, J. Meyer, R. Schaeffer, *Nucl. Phys.* A 635, 231 (1998).
- [17] J. Dobaczewski, H. Flocard, J. Treiner, *Nucl. Phys.* A 422, 103 (1984).
- [18] J. Dobaczewski, W. Nazarewicz, T.R. Werner, J.F. Berger, C.R. Chinn, J. Dechargé, *Phys. Rev. C* 53, 2809 (1996).
- [19] S.T. Belyaev, A.V. Smirnov, S.V. Tolokonnikov, and S.A. Fayans, *Yad. Fiz.* 45, 1263 (1987).
- [20] M. Grasso, N. Sandulescu, Nguyen Van Giai, R. J. Liotta, *Phys. Rev C* 64, 064321 (2001).
- [21] B.D. Serot, J.D. Walecka, *Adv. Nucl. Phys.* 16, 1 (1986).
- [22] B.D. Serot, J.D. Walecka, *Int. J. Mod. Phys. E* 6, 515 (1997).
- [23] T. Bürvenich, D.G. Madland, J.A. Maruhn, P.-G. Reinhard, *Phys. Rev. C* 65, 044308 (2002).
- [24] G.A. Lalazissis, J. König, P. Ring, *Phys. Rev. C* 55, 540 (1997).
- [25] F. Hofmann, C. M. Keil, and H. Lenske, *Phys. Rev. C* 64, 034314 (2001).
- [26] S. Typel, H.H. Wolter, *Nucl. Phys.* A 656, 331 (1999).
- [27] T. Nikšić, D. Vretenar, P. Finelli, P. Ring, *Phys. Rev. C* 66, 024306 (2002).
- [28] G.A. Lalazissis, T. Nikšić, D. Vretenar, P. Ring, *Phys. Rev. C* 71, 024312 (2005).
- [29] E. Khan, N. Sandulescu, M. Grasso, N. V. Giai, *Phys. Rev. C* 66, 024309 (2002).
- [30] M. Matsuo, *Nucl. Phys.* A 696, 371 (2001).
- [31] J. Engel, M. Bender, J. Dobaczewski, W. Nazarewicz, and R. Surman, *Phys. Rev. C* 60, 014302 (1999).
- [32] J. Terasaki, J. Engel, M. Bender, J. Dobaczewski, W. Nazarewicz, and M. Stoitsov, *Phys. Rev. C* 71, 034310 (2005).
- [33] Z.Y. Ma, N. Van Giai, H. Toki, and M. L’Huillier, *Phys. Rev. C* 55, 2385 (1997).
- [34] D. Vretenar, A. Wandelt, and P. Ring, *Phys. Lett. B* 487, 334 (2000).
- [35] T. Nikšić, D. Vretenar, and P. Ring, *Phys. Rev. C* 66, 064302 (2002).
- [36] P. Ring, Zhong-yu Ma, Nguyen Van Giai, D. Vretenar, A. Wandelt, and Li-gang Cao, *Nucl. Phys.* A 694, 249 (2001).
- [37] N. Paar, P. Ring, T. Nikšić, and D. Vretenar, *Phys. Rev. C* 67, 034312 (2003).
- [38] Li-Gang Cao and Zhong-Yu Ma, *Phys. Rev. C* 71, 034305 (2005).
- [39] G.F. Bertsch, P.F. Bortignon, R.A. Broglia, *Rev. Mod. Phys.* 55, 287 (1983).
- [40] C. Mahaux, P.F. Bortignon, R.A. Broglia, C.H. Dasso, *Phys. Rep.* 120, 1 (1985).
- [41] F. Ghielmetti, G. Colò, E. Vigezzi, P.F. Bortignon, R.A. Broglia, *Phys. Rev. C* 54, R2143 (1996).
- [42] C. Yannouleas, *Phys. Rev. C* 35, 1159 (1987).

- [43] S. Drożdż, S. Nishizaki, J. Speth, J. Wambach, Phys. Rep. 197, 1 (1990).
- [44] A. Bohr, B. Mottelson, Nuclear Structure (vol. II), W.A. Benjamin, New York (1975).
- [45] S. Kamenzhiev, J. Speth, G. Tertychny and V. Tselyaev, Nucl. Phys. A555, 90 (1993).
- [46] S. Kamenzhiev, J. Speth, and G. Tertychny, Phys. Rep. 393, 1 (2004).
- [47] V.G. Soloviev, Theory of Atomic Nuclei: Quasiparticles and Phonons, Inst. of Phys. Publ., Bristol and Philadelphia, 1992.
- [48] C. A. Bertulani and V. Yu. Ponomarev, Phys. Rep. 321, 139 (1999).
- [49] M. Gong and M. Tohyama, Z. Phys. A 335, 153 (1990).
- [50] M. Tohyama and A. S. Umar, Phys. Lett. B 516, 415 (2001); *ibid* 549, 72 (2002).
- [51] P.F. Bortignon, R.A. Broglia, D.R. Bes, R. Liotta, Phys. Rep. 30, 305 (1977).
- [52] F. Barranco *et al.*, Phys. Rev. Lett. 83, 2147 (1999).
- [53] G. Colò, P.F. Bortignon, N. Van Giai, A. Bracco, R.A. Broglia, Phys. Lett. B 276, 279 (1992).
- [54] G. Colò, N. Van Giai, P. F. Bortignon, and R. A. Broglia, Phys. Rev. C 50, 1496 (1994).
- [55] V.Yu. Ponomarev, private communication.
- [56] A. Zilges, S. Volz, M. Babilon, T. Hartmann, P. Mohr, and K. Vogt, Phys. Lett. B 542, 43 (2002).
- [57] T. Kobayashi *et al.*, Phys. Lett. B 232, 51 (1989).
- [58] P. G. Hansen and B. Johnson, Europhys. Lett. 4, 409 (1987).
- [59] G. F. Bertsch and J. Foxwell, Phys. Rev. C 41, 1300 (1990) (see also Phys. Rev. C 42, 1159 (1990)).
- [60] N. Aoi *et al.*, Nucl. Phys. A 616, 181c (1997); H. Simon *et al.*, Phys. Rev. Lett. 83, 496 (1999).
- [61] F. Catara, C. H. Dasso, A. Vitturi, Nucl. Phys. A 602, 181 (1996).
- [62] T. Nakamura *et al.*, Phys. Lett. B 331, 296 (1994).
- [63] I. Hamamoto, H. Sagawa, X. Z. Zhang, Nucl. Phys. A 648, 203 (1999).
- [64] C. A. Bertulani, A. Sustich, Phys. Rev. C 46, 2340 (1992).
- [65] G. F. Bertsch and H. Esbensen, Ann. Phys. (N.Y.) 209, 327 (1991).
- [66] H. Esbensen and G. F. Bertsch, Nucl. Phys. A 542, 310 (1992).
- [67] H. Esbensen, G. F. Bertsch, K. Hencken, Phys. Rev. C 56, 3054 (1997).
- [68] F. Barranco, P. F. Bortignon, R. A. Broglia, G. Colò and E. Vigezzi, Eur. Phys. J. A 11, 385 (2001); G. Gori, F. Barranco, E. Vigezzi, and R. A. Broglia, Phys. Rev. C 69, 041302 (2004).
- [69] T. Aumann *et al.*, Phys. Rev. C 59, 1252 (1999).
- [70] Y. Iwata *et al.*, Phys. Rev. C 62, 064311 (2000).
- [71] K. Ieki *et al.*, Phys. Rev. Lett. 70, 730 (1993); D. Sackett *et al.*, Phys. Rev. C 48, 118 (1993); M. Zinser *et al.*, Nucl. Phys. A 619, 151 (1997).
- [72] S. Shimoura, T. Nakamura, M. Ishihara, N. Inabe, T. Kobayashi, K. Kubo, R. H. Siemssen, I. Tanihata, and Y. Watanabe, Phys. Lett. B 348, 29 (1995).
- [73] T. Nakamura *et al.*, Phys. Rev. Lett. 96, 252502 (2006).
- [74] H. Iwasaki *et al.*, Phys. Lett. B 491, 8 (2000).
- [75] M. Labiche *et al.*, Phys. Rev. Lett. 86, 600 (2001).
- [76] T. Nakamura *et al.*, Phys. Rev. Lett. 83, 1112 (1999).
- [77] T. Motobayashi *et al.*, Phys. Rev. Lett. 73, 2680 (1994); T. Kikuchi *et al.*, Eur. Phys. J. A 3, 213 (1998); N. Iwasa *et al.*, Phys. Rev. Lett. 83, 2910 (1999).
- [78] A. A. Korshennikov *et al.*, Phys. Rev. C 53, R537 (1996).
- [79] T. Suzuki, H. Sagawa, P. F. Bortignon, Nucl. Phys. A 662, 282 (2000).
- [80] I. Hamamoto, H. Sagawa, and X. Z. Zhang, Phys. Rev. C 57, R1064 (1998).
- [81] E. G. Fuller, Phys. Rep. 127, 187 (1985).
- [82] A. Vessiere *et al.*, Nucl. Phys. A 227, 513 (1974).
- [83] B. L. Berman, At. Dat. Nucl. Dat. Tabl. 15, 319 (1975).
- [84] T. Aumann *et al.*, Nucl. Phys. A 649, 297c (1996).
- [85] A. Leistenschneider *et al.*, Phys. Rev. Lett. 86, 5442 (2001).
- [86] E. Tryggstad *et al.*, Nucl. Phys. A 687, 231c (2001).
- [87] E. Tryggstad *et al.*, Phys. Lett. B 541, 52 (2002).

- [88] E. Tryggestad *et al.*, Phys. Rev. C 67, 064309 (2003).
- [89] H. Sagawa and T. Suzuki, Phys. Rev. C 59, 3116 (1999).
- [90] H. Sagawa and T. Suzuki, Nucl. Phys. A 687, 111c (2001).
- [91] M. Matsuo, Prog. Theor. Phys. Suppl. 146, 110 (2002).
- [92] G. Colò and P.F. Bortignon, Nucl. Phys. A 696, 427 (2001).
- [93] Nguyen Dinh Dang, Vuong Kim Au, T. Suzuki, and A. Arima, Phys. Rev. C 63, 044302 (2001).
- [94] J. G. Woodworth *et al.*, Phys. Rev. C 19, 1667 (1979).
- [95] D. Vretenar, N. Paar, P. Ring, and G. A. Lalazissis, Nucl. Phys. A 692, 496 (2001).
- [96] N. Fukunishi, T. Otsuka, and I. Tanihata, Phys. Rev. C 48, 1648 (1993).
- [97] I. Hamamoto and X. Z. Zhang, Phys. Rev. C 52, R2326 (1995).
- [98] S. Mizutori, J. Dobaczewski, G. A. Lalazissis, W. Nazarewicz, and P. G. Reinhard, Phys. Rev. C 61, 044326 (2000).
- [99] K. Amos, S. Karataglidis, and J. Dobaczewski, Phys. Rev. C 70, 024607 (2004).
- [100] A. Trzcinska, J. Jastrzebski, P. Lubinski, F. J. Hartmann, R. Schmidt, T. von Egidy, and B. Klos, Phys. Rev. Lett. 87, 082501 (2001).
- [101] A. Ozawa, T. Suzuki, and I. Tanihata, Nucl. Phys. A 693, 32 (2001).
- [102] A. Krasznahorkay *et al.*, Phys. Rev. C 64, 067302 (2001).
- [103] H. D. Wohlfahrt *et al.*, Phys. Rev. C 23, 533 (1981).
- [104] R. H. McCamis *et al.*, Phys. Rev. C 33, 1624 (1986).
- [105] J. Duflo and A. P. Zuker, Phys. Rev. C 66, 051304(R) (2002).
- [106] S. Goriely and E. Khan, Nucl. Phys. A 706, 217 (2002).
- [107] S. Goriely, E. Khan, and M. Samyn, Nucl. Phys. A 739, 331 (2004).
- [108] Radhe Mohan, M. Danos and L.C. Biedenharn, Phys. Rev. C 3, 1740 (1971).
- [109] Y. Suzuki, K. Ikeda, and H. Sato, Prog. Theor. Phys. 83, 180 (1990).
- [110] P. Van Isacker, M. A. Nagarajan, and D. D. Warner, Phys. Rev. C 45, R13 (1992).
- [111] J. Chambers, E. Zaremba, J.P. Adams, and B. Castel, Phys. Rev. C 50, R2671 (1994).
- [112] F. Catara, E.G. Lanza, M.A. Nagarajan and A. Vitturi, Nucl. Phys. A 624, 449 (1997).
- [113] A. Vitturi, J. Phys. G 24, 1439 (1998).
- [114] P.-G. Reinhard, Nucl. Phys. A 649, 305c (1999).
- [115] I. Hamamoto and H. Sagawa, Phys. Rev. C 53, R1492 (1996).
- [116] I. Hamamoto, H. Sagawa, and X. Z. Zhang, Phys. Rev. C 53, 765 (1996).
- [117] S. Kamerdzhiev, R. J. Liotta, E. Litvinova, and V. Tselyaev, Phys. Rev. C 58, 172 (1998).
- [118] H. Sagawa and H. Esbensen, Nucl. Phys. A 693, 448 (2001).
- [119] I. Hamamoto and H. Sagawa, Phys. Rev. C 66, 044315 (2002).
- [120] J. Terasaki and J. Engel, Phys. Rev. C 74, 044301 (2006).
- [121] T. N. Leite and N. Teruya, Eur. Phys. J. A 21, 369 (2004).
- [122] C. H. Dasso, H. M. Sofia, S. M. Lenzi, M. A. Nagarajan, and A. Vitturi, Nucl. Phys. A 627, 349 (1997).
- [123] A. Zilges, M. Babilon, T. Hartmann, D. Savran, and S. Volz, Prog. Part. Nucl. Phys. 55, 408 (2005).
- [124] S. Peru and J. F. Berger, Int. J. Mod. Phys. E 13, 175 (2004).
- [125] S. Peru, J. F. Berger, and P. F. Bortignon, Eur. Phys. J. A 26, 25 (2005).
- [126] M. Yamagami, E. Khan, and Nguyen Van Giai, Proc. Int. Symp. on Frontiers of Collective Motion 2002, eds. H. Sagawa and H. Iwasaki, World Scientific.
- [127] M. Yamagami and Nguyen Van Giai, Phys. Rev. C 69, 034301 (2004).
- [128] D. Vretenar, N. Paar, P. Ring, and G. A. Lalazissis, Phys. Rev. C 63, 047301 (2001).
- [129] N. Paar, PhD thesis, Technische Universität Muenchen (2003). <http://tumb1.biblio.tu-muenchen.de/publ/diss/ph/2003/paar.ps>
- [130] N. Paar, T. Nikšić, D. Vretenar, and P. Ring, Phys. Lett. B 606, 288 (2005).
- [131] Li-Gang Cao and Zhong-Yu Ma, Mod. Phys. Lett. A 19, 2845 (2004).
- [132] N. D. Dang, T. Suzuki, and A. Arima, Phys. Rev. C 61, 064304 (2000).

- [133] N. Ryezayeva, T. Hartmann, Y. Kalmykov, H. Lenske, P. von Neumann-Cosel, V. Yu. Ponomarev, A. Richter, A. Shevchenko, S. Volz, and J. Wambach, *Phys. Rev. Lett.* 89, 272502 (2002).
- [134] N. Tsoneva, H. Lenske, and Ch. Stoyanov, *Nucl. Phys. A* 731, 273 (2004).
- [135] N. Tsoneva, H. Lenske, and Ch. Stoyanov, *Phys. Lett. B* 586, 213 (2004).
- [136] T. Hartmann *et al.*, *Phys. Rev. Lett.* 93, 192501 (2004).
- [137] G. A. Bartholomew *et al.*, *Adv. Nucl. Phys.* 7, 229 (1972).
- [138] M. Igashira, H. Kitazawa, M. Shimizu, H. Komano, and N. Yamamuro, *Nucl. Phys. A* 457, 301 (1986).
- [139] U. Kneissl, H. H. Pitz, and A. Zilges, *Prog. Part. Nucl. Phys.* 37, 349 (1996).
- [140] T. Hartmann, J. Enders, P. Mohr, K. Vogt, S. Volz, and A. Zilges, *Phys. Rev. Lett.* 85, 274 (2000).
- [141] F. Bauwens *et al.*, *Phys. Rev. C* 62, 024302 (2000).
- [142] L. Käubler *et al.*, *Phys. Rev. C* 70, 064307 (2004).
- [143] B. Özel *et al.*, *Proceedings of COMEX2*, *Nucl. Phys. A*, in press (2006).
- [144] K. Govaert, F. Bauwens, J. Bryssinck, D. De Frenne, E. Jacobs, W. Mondelaers, L. Govor, and V. Yu. Ponomarev, *Phys. Rev. C* 57, 2229 (1998).
- [145] R. D. Herzberg *et al.*, *Phys. Lett. B* 390, 49 (1997).
- [146] R. D. Herzberg *et al.*, *Phys. Rev. C* 60, 051307 (1999).
- [147] T. Chapuran, R. Vodhanel, M. K. Brussel, *Phys. Rev. C* 22, 1420 (1980).
- [148] J. Enders *et al.*, *Phys. Lett. B* 486, 279 (2000).
- [149] J. Enders *et al.*, *Nucl. Phys. A* 724, 243 (2003).
- [150] U. Kneissl, N. Pietralla, and A. Zilges, *J. Phys. G* 32, R217 (2006).
- [151] T. Aumann, *Eur. Phys. J. A* 26, 441 (2005).
- [152] P. Adrich *et al.*, *Phys. Rev. Lett.* 95, 132501 (2005).
- [153] D. Sarchi, P. F. Bortignon, and G. Colò, *Phys. Lett. B* 601, 27 (2004).
- [154] R. D. Starr, P. Axel and L. S. Cardman, *Phys. Rev. C* 25, 780 (1982).
- [155] Z. W. Bell, L. S. Cardman and P. Axel, *Phys. Rev. C* 25, 791 (1982).
- [156] G. Kühner, D. Meuer, S. Müller, A. Richter, E. Spamer, O. Titze and W. Knüpfner, *Phys. Lett. B* 104, 189 (1981).
- [157] J. P. Adams, B. Castel and H. Sagawa, *Phys. Rev. C* 53, 1016 (1996).
- [158] J. Ritman *et al.*, *Phys. Rev. Lett.* 70, 533 (1993).
- [159] J. Enders *et al.*, *Acta Phys. Pol. B* 36, 1077 (2005).
- [160] J. Enders *et al.*, *Nucl. Phys. A* 741, 3 (2004).
- [161] G. Audi and A. H. Wapstra, *Nucl. Phys. A* 595, 409 (1995).
- [162] R. Schwengner, R. Beyer, F. Dönau, E. Grosse, A. Hartmann, A. R. Junghans, S. Mallion, G. Rusev, K. D. Schilling, W. Schultze, and A. Wagner, *Nucl. Instr. Meth. Phys. Res. A* 555, 211 (2005).
- [163] A. Wagner *et al.*, *J. Phys. G* 31, S1969 (2005).
- [164] G. Rusev, E. Grosse, M. Erhard, A. Junghans, K. Kosev, K.-D. Schilling, R. Schwengner, and A. Wagner, *proceedings Nuclear Physics in Astrophysics II*, Debrecen, Hungary, (2005), [nucl-ex/0512027](#)
- [165] J. Piekarewicz, *Phys. Rev. C* 73, 044325 (2006).
- [166] N. Paar, D. Vretenar, and P. Ring, *Phys. Rev. Lett.* 94, 182501 (2005).
- [167] A. Ozawa *et al.*, *Nucl. Phys. A* 709, 60 (2002).
- [168] W. Nazarewicz *et al.*, *Phys. Rev. C* 53, 740 (1996).
- [169] G.A. Lalazissis, D. Vretenar, and P. Ring, *Phys. Rev. C* 63, 034305 (2001).
- [170] H. Sagawa, T. Suzuki, H. Iwasaki, and M. Ishihara, *Phys. Rev. C* 63, 034310 (2001).
- [171] N. Van Giai, Z. Y. Ma, H. Toki, B. Chen, *Nucl. Phys. A* 649, 37 (1999).
- [172] J. Giovannazzo *et al.*, *Phys. Rev. Lett.* 89, 102501 (2002).
- [173] M. Pfutzner *et al.*, *Eur. Phys. J. A* 14, 279 (2002).
- [174] N. Paar, P. Papakonstantinou, V. Yu. Ponomarev, and J. Wambach, *Phys. Lett. B* 624, 195

- (2005).
- [175] M. Matsuo, K. Mizuyama, Y. Serizawa, Phys. Rev. C 71, 064326 (2005).
- [176] M. Matsuo, Y. Serizawa, and K. Mizuyama, Proceedings of COMEX2, Nucl. Phys. A, in press (2006).
- [177] J.P. Blaizot, Phys. Rep. 64, 171 (1980).
- [178] J.P. Blaizot, J.F. Berger, J. Dechargé, and M. Girod, Nucl. Phys. A 591, 435 (1995).
- [179] V. M. Kolomietz and S. Shlomo, Phys. Rev. C 61, 064302 (2000).
- [180] I. Hamamoto, H. Sagawa, and X. Z. Zhang, Phys. Rev. C 56, 3121 (1997).
- [181] S. Shlomo and A. I. Sanzhur, Phys. Rev. C 65, 044310 (2002).
- [182] B. K. Agrawal, S. Shlomo, and V. Kim Au, Phys. Rev. C 68, 031304(R) (2003).
- [183] G. Colò, N. Van Giai, J. Meyer, K. Bennaceur, and P. Bonche, Phys. Rev. C 70, 024307 (2004).
- [184] J. Kvasil, N. Lo Iudice, Ch. Stoyanov, and P. Alexa, J. Phys. G 29, 753 (2003).
- [185] D. Lacroix, S. Ayik, and P. Chomaz, Phys. Rev. C 63, 064305 (2001).
- [186] S. Yildirim, T. Gaitanos, M. Di Toro, and V. Greco, Phys. Rev. C 72, 064317 (2005).
- [187] Z.Y. Ma, N. Van Giai, A. Wandelt, D. Vretenar and P. Ring, Nucl. Phys. A 686, 173 (2001).
- [188] J. Piekarewicz, Phys. Rev. C 64, 024307 (2001).
- [189] J. Piekarewicz, Phys. Rev. C 66, 034305 (2002).
- [190] D. Vretenar, T. Nikšić, and P. Ring, Phys. Rev. C 68, 024310 (2003).
- [191] G. Colò and N. Van Giai, Nucl. Phys. A 731, 15 (2004).
- [192] H. L. Clark, Y.-W. Lui, and D. H. Youngblood, Phys. Rev. C 63, 031301(R) (2001).
- [193] D. H. Youngblood, Y.-W. Lui, B. John, Y. Tokimoto, H. L. Clark, and X. Chen, Phys. Rev. C 69, 054312 (2004).
- [194] M. Uchida et al., Phys. Lett. B 557, 12 (2003).
- [195] M. Uchida et al., Phys. Rev. C 69, 051301(R) (2004).
- [196] U. Garg, Nucl. Phys. A 731, 3 (2004).
- [197] G. Colò, N. Van Giai, P.F. Bortignon, and M.R. Quaglia, Phys. Lett. B 485, 362 (2000).
- [198] S.I. Bastrukov, S. Misicu, and V.I. Sushkov, Nucl. Phys. A 562, 191 (1993).
- [199] S. Misicu, Phys. Rev. C 73, 024301 (2006).
- [200] D. Vretenar, N. Paar, P. Ring, and T. Nikšić, Phys. Rev. C 65, 021301(R) (2002).
- [201] M. Itoh et al., Phys. Rev. C 68, 064602 (2003).
- [202] T. Sil, S. Shlomo, B. K. Agrawal, and P.-G. Reinhard, Phys. Rev. C 73, 034316 (2006).
- [203] Y.-W. Lui, D. H. Youngblood, H. L. Clark, Y. Tokimoto, and B. John, Phys. Rev. C 73, 014314 (2006).
- [204] B. K. Nayak et al., Phys. Lett. B 637, 43 (2006).
- [205] N. Paar, D. Vretenar, T. Nikšić, and P. Ring, Phys. Rev. C 74, 037303 (2006).
- [206] V.M. Dubovik and A.A. Cheshkov, Sov. J. Part. Nucl. 5, 318 (1975).
- [207] V.M. Dubovik and L.A. Tosunyan, Sov. J. Part. Nucl. 14, 504 (1983).
- [208] S.F. Semenko, Sov. J. Nucl. Phys. 34, 356 (1981).
- [209] E.B. Balbutsev and I.N. Mikhailov, J. Phys.G: Nucl. Phys. 14, 545 (1988).
- [210] P. Papakonstantinou, J. Wambach, E. Mavrommatis, and V.Yu. Ponomarev, Phys. Lett. B 604, 157 (2004).
- [211] D. H. Youngblood, Y.-W. Lui, H. L. Clark, B. John, Y. Tokimoto, and X. Chen, Phys. Rev. C 69, 034315 (2004).
- [212] A. Richter, Nucl. Phys. A 731, 59 (2004).
- [213] O. Tarasov *et al.*, Phys. Lett. B 409, 64 (1997).
- [214] J.K. Jewell *et al.*, Phys. Lett. B 454, 181 (1999).
- [215] P.G. Thirolf *et al.*, Phys. Lett. B 485, 16 (2000).
- [216] E. Khan *et al.*, Phys. Lett. B 490, 45 (2000).
- [217] M. Bellegruic *et al.*, Nucl. Phys. A 682, 136c (2001).
- [218] M. Stanoiu *et al.*, Phys. Rev. C 69, 034312 (2004).
- [219] E. Becheva *et al.*, Phys. Rev. Lett 96, 012501 (2006).

- [220] T. Otsuka *et al.*, Phys. Rev. Lett 87, 082502 (2001).
- [221] M. Tohyama, A.S. Umar, Phys. Lett. B 549, 72 (2002).
- [222] P. Ring *et al.*, Nucl. Phys. A 722, 372c (2003).
- [223] B.A. Brown and W.A. Richter, Phys. Rev. C 72, 057301 (2005).
- [224] B.A. Brown, Prog. Part. Nucl. Phys. 47, 517 (2001).
- [225] Y. Utsuno, T. Otsuka, T. Mizusaki, M. Honma, Phys. Rev. C 60, 054315 (1999).
- [226] G. Giambrone *et al.*, Nucl. Phys. A 726, 6 (2003).
- [227] E. Khan *et al.* Nucl. Phys A 694, 103 (2001).
- [228] Nguyen Van Giai and H. Sagawa, Nucl. Phys A 371, 1 (1981).
- [229] N. Sandulescu, P. Schuck and X. Viñas, Phys. Rev. C 71, 054303 (2005).
- [230] B. A. Brown and B. H. Wildenthal, Ann. Rev. Part. Nucl. Sci. 38, 29 (1988).
- [231] G. E. Brown and A. M. Green, Nucl. Phys. 75, 401 (1966).
- [232] P. Federman and I. Talmi, Phys. Lett. 15, 165 (1965).
- [233] D.T. Khoa *et al.*, Nucl. Phys. A 706, 61 (2002).
- [234] J.P. Jeukenne, A. Lejeune and C. Mahaux, Phys. Rev. C 16, 80 (1977).
- [235] A.J. Koning and J.P. Delaroche, Nucl. Phys. A 713, 231 (2003).
- [236] J. Raynal, Phys. Rev. C 23, 2571 (1981).
- [237] Zs. Dombraci *et al.*, Phys. Rev. Lett. 96, 182501 (2006).
- [238] G. Colò, P.F. Bortignon, D. Sarchi, D.T. Khoa, E. Khan and N. Van Giai, Nucl. Phys. A 722, 111c (2003).
- [239] S. Raman *et al.*, At. Data Nucl. Data Tables 78, 1 (2001); T. Kibédi and R.H. Spear, At. Data Nucl. Data Tables 80, 35 (2002); A. Holt *et al.*, Nucl. Phys. A 634, 41 (1998).
- [240] D.C. Radford (private communication); see also D.C. Radford *et al.*, Phys. Rev. Lett. 88, 222501 (2002).
- [241] W. von Oertzen, A. Vitturi, Rep. Prog. Phys. 64, 1247 (2001).
- [242] D.R. Bès and R.A. Broglia, Nucl. Phys. 80, 289 (1966).
- [243] R.A. Broglia, O. Hansen and C. Riedel, Advances in Nuclear Physics, NY Plenum, 6, 287 (1973).
- [244] L. Fortunato, W. von Oertzen, H.M. Sofia and A. Vitturi, Eur. Phys. J. A 14, 37 (2002).
- [245] R.A. Broglia and D.R. Bès, Phys. Lett. B 69, 129 (1977).
- [246] M.W. Herzog, R.J. Liotta and T. Vertse, Phys. Lett. B 165, 35 (1985).
- [247] G.M. Crawley, W. Benenson, D. Weber, B. Zwieglinski, Phys. Rev. Lett. 39, 1451 (1977).
- [248] G.M. Crawley, W. Benenson, G. Bertsch, S. Gales, D. Weber, B. Zwieglinski, Phys. Rev. C 23, 589 (1981).
- [249] P.F. Bortignon, E. Maglione, A. Vitturi, F. Zardi, R.A. Broglia, Phys. Scr. 34, 678 (1986).
- [250] E. Khan, N. Sandulescu, Nguyen Van Giai, M. Grasso, Phys. Rev. C 69, 014314 (2004).
- [251] A. Bouyssy and N. Vinh Mau, Nucl. Phys. A 224, 331 (1974).
- [252] G. Ripka and R. Padjen, Nucl. Phys. A 132, 489 (1969).
- [253] G.R. Satchler, Direct Nuclear Reactions, Clarendon Press, Oxford, 1983.
- [254] F.D. Becchetti and G.W. Greenlees, Polarization Phenomena in Nuclear Reactions, H.H. Barschall and W. Haeberti eds., Madison, Winsconsin, 1971, p. 682.
- [255] F.D. Becchetti and G.W. Greenlees, Phys. Rev. 182, 1190 (1969).
- [256] M. Igarashi, K. Kubo and K. Yagi, Phys. Rep. 199, 1 (1991).
- [257] F. Osterfeld, Rev. Mod. Phys. 64, 491 (1992).
- [258] I. Hamamoto and H. Sagawa, Phys. Rev. C 48, R960 (1993).
- [259] N. Auerbach, N. Van Giai and A. Yeverechyahu, Highly Excited States in Nuclear Reactions, H. Ikegami and M. Muraoka eds., RCNP, Osaka, 1980, p. 623.
- [260] N. Auerbach and A. Klein, Nucl. Phys. A 395, 77 (1983).
- [261] S. Adachi and S. Yoshida, Nucl. Phys. A 462, 61 (1987).
- [262] G. Colò, H. Sagawa, N. Van Giai, P. F. Bortignon, and T. Suzuki, Phys. Rev. C 57, 3049 (1998).
- [263] J. A. Halbleib and R. A. Sorensen, Nucl. Phys. A 98, 542 (1967).
- [264] P. Sarriguren, E. Moya de Guerra, A. Escuderos and A.C. Carrizo, Nucl. Phys. A 635, 55 (1998).



- [265] P. Sarriguren, E. Moya de Guerra and A. Escuderos, Nucl. Phys. A 658, 13 (1999).
- [266] P. Sarriguren, E. Moya de Guerra and A. Escuderos, Nucl. Phys. A 691, 631 (2001).
- [267] P. Sarriguren, E. Moya de Guerra and A. Escuderos, Phys. Rev. C 64, 064306 (2001).
- [268] O. Moreno, P. Sarriguren, R. Álvarez-Rodríguez and E. Moya De Guerra, Phys. Rev. C 73, 054302 (2006).
- [269] M. Bender, J. Dobaczewski, J. Engel, and W. Nazarewicz Phys Rev C 65, 054322 (2002).
- [270] S. Fracasso and G. Colò, Phys. Rev. 72, 064310 (2005).
- [271] K. Pham *et al.*, Phys. Rev. C 51, 526 (1995).
- [272] N. Paar, T. Nikšić, D. Vretenar, and P. Ring, Phys. Rev. C 69, 054303 (2004).
- [273] C. De Conti, A. P. Galeão and F. Krmpotić, Phys. Lett. B 494, 46 (2000).
- [274] Z-Y. Ma, B-Q. Chen, N. Van Giai, and T. Suzuki, Eur. Phys. J. A 20, 429 (2004).
- [275] S. Krewald, F. Osterfeld, J. Speth, and G. E. Brown, Phys. Rev. Lett. 46, 103 (1981).
- [276] G. E. Brown and M. Rho, Nucl. Phys. A 372, 397 (1981).
- [277] S. Krewald, K. Nakayama, and J. Speth, Phys. Rep. 161, 103 (1988).
- [278] T. Nikšić, T. Marketin, D. Vretenar, N. Paar, and P. Ring, Phys. Rev. C 71, 014308 (2005).
- [279] K. Ikeda, S. Fujii and J. I. Fujita, Phys. Lett. 3, 271 (1963).
- [280] R. R. Doering, A. Galonsky, D. M. Patterson, and G. F. Bertsch, Phys. Rev. Lett. 35, 1961 (1975).
- [281] H. Fujita *et al.*, Nucl. Instrum. Methods Phys. Res. Sect. A 484, 17 (2002).
- [282] Y. Kalmykov *et al.*, Phys. Rev. Lett. 96, 012502 (2006).
- [283] Y. Fujita *et al.*, Phys. Rev. Lett. 95, 212501 (2005).
- [284] E. Caurier, G. Martinez-Pinedo, F. Nowacki, A. Poves, and A. P. Zuker, Rev. Mod. Phys. 77, 427 (2005).
- [285] E. Caurier, K. Langanke, G. Martinez-Pinedo and F. Nowacki, Nucl. Phys. A 653, 439 (1999).
- [286] E. Caurier, G. Martinez-Pinedo, A. Poves, and A. P. Zuker, Phys. Rev. C 52, R1736 (1995).
- [287] P. B. Radha, D. J. Dean, S. E. Koonin, K. Langanke and P. Vogel, Phys. Rev. C 56, 3079 (1997).
- [288] C. De Conti, A. P. Galeão and F. Krmpotić, Phys. Lett. B 444, 14 (1998).
- [289] H. Kurasawa, T. Suzuki and N. Van Giai, Phys. Rev. Lett. 91, 062501 (2003).
- [290] I. N. Borzov, Phys. Rev. C 67, 025802 (2003).
- [291] N. Van Giai and H. Sagawa, Phys. Lett. B 106, 379 (1981).
- [292] T. Suzuki and H. Sagawa, Eur. Phys. J. A 9, 49 (2000).
- [293] I. N. Borzov, and S. Goriely, Phys. Rev. C 62, 035501 (2000).
- [294] D. Cha, Phys. Rev. C 27, 2269 (1983).
- [295] J. Engel, P. Vogel and M. R. Zirnbauer, Phys. Rev. C 37, 731 (1988).
- [296] M. K. Cheoun, A. Faessler, F. Simkovic, G. Teneva and A. Bobyk, Nucl. Phys. A 587, 301 (1995).
- [297] I.N. Borzov, S.A. Fayans, and E.L. Trykov, Nucl. Phys. A 584, 335 (1995).
- [298] I.N. Borzov, S.A. Fayans, E. Krömer, and D. Zawischa, Z. Phys. A 355, 117 (1996).
- [299] M. K. Cheoun, A. Bobyk, A. Faessler, F. Simkovic, and G. Teneva, Nucl. Phys. A 561, 74 (1993).
- [300] J. G. Hirsch, P. O. Hess, and O. Civitarese, Phys. Lett. B 390, 36 (1997).
- [301] G. Pantis, F. Šimkovic, J. D. Vergados, and A. Faessler, Phys. Rev. C 53, 695 (1996).
- [302] V. A. Rodin and M. H. Urin, Phys. Atom. Nucl. 66, 2128 (2003).
- [303] I. Stetcu and C. W. Johnson, Phys. Rev. C 69, 024311 (2004).
- [304] R. Álvarez-Rodríguez, P. Sarriguren, E. Moya de Guerra, L. Paceaescu, A. Faessler, and F. Šimkovic, Phys. Rev. C 70, 064309 (2004).
- [305] B. D. Anderson *et. al.* Phys. Rev. C 31, 1161 (1985).
- [306] D. E. Bainum *et. al.* Phys. Rev. Lett. 44, 1751 (1980).
- [307] T. Wakasa *et. al.*, Phys. Rev. C 55, 2909 (1997).
- [308] H. Akimune *et. al.*, Phys. Rev. C 52, 604 (1995).
- [309] D. J. Horen *et. al.*, Phys. Lett. B 95, 27 (1980).
- [310] V. G. Guba, M. A. Nikolaev, and M. G. Urin, Phys. Lett. B 218, 283 (1989).
- [311] K. Langanke and G. Martínez-Pinedo, Rev. Mod. Phys. 75, 819 (2003).

- [312] I.N. Borzov, Nucl. Phys. A 777, 645 (2006).
- [313] C. Gaarde, Nucl. Phys. A 396, 127c (1983).
- [314] K. Shimizu, M. Ichimura, and A. Arima, Nucl. Phys. A 226, 282 (1974).
- [315] G. F. Bertsch and I. Hamamoto, Phys. Rev. C 26, 1323 (1982).
- [316] S. Drożdż, V. Klemt, J. Speth, and J. Wambach, Phys. Lett. B 166, 18 (1986).
- [317] M. Rho, Nucl. Phys. A 231, 493 (1974).
- [318] K. Ohta and M. Wakamatsu, Nucl. Phys. A 234, 445 (1974).
- [319] M. Ericson, A. Figureau, and C. Thevenet, Phys. Lett. B 45, 19 (1973).
- [320] W. Knüpfner, M. Dillig, and A. Richter, Phys. Lett. B 95, 349 (1980).
- [321] T. Wakasa et al., Phys. Lett. B 426, 257 (1998).
- [322] H. Kurasawa, T. Suzuki and N. Van Giai, Phys. Rev. C 68, 064311 (2003).
- [323] H. Kurasawa and T. Suzuki, Phys. Rev. C 69, 014306 (2004).
- [324] H. Kurasawa and T. Suzuki, to appear in Mod. Phys. Lett. A (2006)., nucl-th/0604015
- [325] E.G. Nadiakov, K.P. Marinova, and Yu.P. Gangrsky, At. Data Nucl. Data Tables 56, 133 (1994).
- [326] A. Krasznahorkay et al., Phys. Rev. Lett. 66, 1287 (1991); Nucl. Phys. A 567, 521 (1994).
- [327] A. Krasznahorkay et al., Phys. Rev. Lett. 82, 3216 (1999).
- [328] T. Suzuki *et al.*, Phys. Rev. Lett. 75, 3241 (1995).
- [329] C. J. Batty, E. Friedman, H. J. Gils, and H. Rebel, Adv. Nucl. Phys. 19, 1 (1989).
- [330] S. Shlomo et al., Phys. Rev. C 36, 1317 (1987).
- [331] K. Nakayama and G. F. Bertsch, Phys. Rev. Lett. 59, 1053 (1987).
- [332] J. Peterson, Phys. Rev. Lett. 59, 1055 (1987).
- [333] D. Vretenar, N. Paar, T. Nikšić, and P. Ring, Phys. Rev. Lett. 91, 262502 (2003).
- [334] G.A. Lalazissis, D. Vretenar, W. Pöschl, and P. Ring, Phys. Lett. B 418, 7 (1998).
- [335] S. Goriely, P. Demetriou, H.-Th. Janka, J.M. Pearson and M. Samyn, Nucl. Phys. A 758, 587 (2004).
- [336] S.Goriely, Phys. Lett. B 436, 10 (1998).
- [337] C.M. McCullagh, M.L. Stelts, R.E. Chrien, Phys. Rev. C 23, 1394 (1981).
- [338] S.G.Kadmenskii, V.P. Markushev, V.I. Furman, Sov. J. Nucl. Phys. 37, 165 (1983).
- [339] J. Kopecky, R. E. Chrien, Nucl. Phys. A 468, 285 (1987).
- [340] S. Goriely, M. Samyn, M. Bender and J.M. Pearson, Phys. Rev. C 68, 054325 (2003).
- [341] S.Goriely and P. Descouvemont, *Ecole Int. Joliot-Curie* (2000).
- [342] W.D. Myers, W.J. Swiatecki, et al., Phys. Rev. C 15 2032 (1977).
- [343] M. Grasso, N. Sandulescu, Nguyen Van Giai, R. J. Liotta, Phys. Rev. C 64, 064321 (2001).
- [344] M. Samyn, S. Goriely, P.-H. Heenen, J.M. Pearson, and F. Tondeur, Nucl. Phys. A 700, 142 (2002).
- [345] S. Goriely, M. Samyn, P.-H. Heenen, J.M. Pearson, and F. Tondeur, Phys. Rev. C 66, 024326 (2002).
- [346] M. Samyn, S. Goriely, and J.M. Pearson, Nucl. Phys. A 725, 69 (2003).
- [347] G. Audi and A. H. Wapstra, private communication (2001).
- [348] S.S. Dietrich, B. L. Berman, At. Data Nucl. Data Tables 38, 199 (1989).
- [349] Photonuclear data for applications; cross sections and spectra, IAEA-Tecdoc-1178 (2000).
- [350] P. Schuck and S. Ayik, Nucl. Phys. A 687, 220c (2001).
- [351] R.D. Smith and J. Wambach, Phys. Rev. C 38, 100 (1988).
- [352] J.Kopecky and M. Uhl, Phys. Rev. C 41, 1941 (1990).
- [353] P.F. Bortignon, Nucl. Phys. A 687, 329c (2001).
- [354] F.-K. Thielemann, M. Arnould, in: Proceedings of Conference on Nuclear Data for Science and Technology, (eds. K. Böckhoff, Reidel, Dordrecht, 1983) 762.
- [355] Reference Input Parameter Library, IAEA-Tecdoc, (2004).
- [356] Goriely S., 2001, in Tours Symposium on Nuclear Physics III, AIP Conf. Proc. 561, eds. M. Arnould et al. (New York: AIP), 53; <http://www-astro.ulb.ac.be>.
- [357] P. Demetriou and S. Goriely, Nucl. Phys. A 695, 95 (2001).

- [358] H. Utsunomiya, H. Akimune, S. Goko, M. Ohta, H. Ueda, T. Yamagata, and K. Yamasaki, H. Ohgaki, H. Toyokawa, Y.-W. Lui, T. Hayakawa, T. Shizuma, E. Khan, S. Goriely, Phys. Rev. C 67, 015807 (2003).
- [359] H. Ayashida *et al.*, Phys. Rev. Lett. 73, 3491 (1994).
- [360] D. J. Bird *et al.*, Astrophys. J. 441, 144 (1995).
- [361] K. Greisen, Phys. Rev. Lett. 16, 748 (1966).
- [362] G.T. Zatsepin and V.A. Kuzmin, Zh. Eksp. Teor. Fiz. Rev. 4, 114 (1966).
- [363] P. Mantsch, 29th Int. Cosmic Ray Conf. (2005), Pune, India, astro-ph/0604114.
- [364] J.L. Puget, F.W. Stecker and J.H. Bredekamp, Astr. J. 205, 638 (1976).
- [365] J.P. Rachen, Ph.D. Thesis (1996), Friedrich-Whilhelms University (Bonn)
- [366] E. Khan, S. Goriely, D. Allard, E. Parizot, T. Suomijarvi, A .J. Koning, S. Hilaire, M.C. Duijvestijn, Astroparticle Phys. 23, 191 (2005).
- [367] D. Allard, E. Parizot, A.V. Olinto, E. Khan, S.Goriely, Astr. and Astr. 443, L29 (2005).
- [368] F.W. Stecker and M.H. Salamon, Astr. J. 512, 521 (1999).
- [369] P. Axel, Phys. Rev. 126, 671 (1962).
- [370] A.J. Koning, S. Hilaire and M.C. Duijvestijn, Proceeding of the International Conference on Nuclear Data for Science and Technology (Santa Fe, USA), 2004.
- [371] Photonuclear data for applications; cross sections and spectra, IAEA-Tecdoc-1178 (2000).
- [372] D. Allard, E. Parizot, A.V. Olinto, in preparation, astro-ph/0512345 (2006).
- [373] C.J. Pethick and D.G. Ravenhall, Annu. Rev. Nucl. Part. Sci. 45, 429 (1995).
- [374] J.W. Negele and D. Vautherin, Nucl. Phys. A 207, 298 (1973).
- [375] F. Douchin and P. Haensel, Phys. Lett. B 485, 107 (2000).
- [376] D.G. Yakovlev and C.J. Pethick, Annu. Rev. Astron. Astrophys. 42, 169 (2004).
- [377] R.A. Broglia, F. De Blasio, G. Lazzari, M. Lazzari, and P.M. Pizzochero, Phys. Rev. D 50, 4781 (1994); F. De Blasio, G. Lazzari, P. M. Pizzochero and R. A. Broglia, Phys. Rev. D 53, 4226 (1996).
- [378] O. Elgaroy, L. Engvik, E. Osnes, F. De Blasio, M. Hjorth-Jensen, and G. Lazzari, Phys. Rev. D 54, 1848 (1996).
- [379] F. Barranco, R.A. Broglia, H. Esbensen, and E. Vigezzi, Phys. Rev. C 58, 1257 (1998); F. Barranco *et al.*, Phys. Lett. B 390, 13 (1997).
- [380] P.M. Pizzochero, F. Barranco, E. Vigezzi, and R. A. Broglia, Ap. J. 569, 381 (2002).
- [381] N. Sandulescu, Nguyen Van Giai, and R. J. Liotta, Phys. Rev. C 69, 045802 (2004).
- [382] N. Sandulescu, Phys. Rev. C 70, 025801 (2004).
- [383] G. Gori, F. Ramponi, F. Barranco, R.A. Broglia, G. Colo, D. Sarchi, E. Vigezzi, Nucl. Phys. A 731, 401 (2004).
- [384] E. Khan, N. Sandulescu, Nguyen Van Giai, Phys. Rev. C 71, 042801 (2005).
- [385] P. Magierski, Int. J. Mod. Phys. E 13, 371 (2004).
- [386] P.G. de Gennes, Superconductivity of Metals and Alloys, Addison-Wesley, Reading, MA, (1989).
- [387] E. Khan, Nguyen Van Giai, M. Grasso, Nucl. Phys. A 731, 311 (2004).
- [388] D. Savran, M. Babilon, A. M. van den Berg, M. N. Harakeh, J. Hasper, A. Matic, H. J. Wörtche, and A. Zilges, Phys. Rev. Lett. 97, 172502 (2006).
- [389] D. Warner and P. Van Isacker, Phys. Lett. B 395, 145 (1987).
- [390] L. V. Grigorenko, K. Langanke, N. B. Shulgina, and M. V. Zhukov, Phys. Lett. B 641, 254 (2006).